universität wien

MASTERARBEIT / MASTER'S THESIS

Titel der Masterarbeit / Title of the Master's Thesis

"Characterization of Fibroblast Growth Factor Receptor 4 as contributor to oncogenesis in Glioblastoma Multiforme"

verfasst von / submitted by

Sushilla Tamara van Schoonhoven

angestrebter akademischer Grad / in partial fulfilment of the requirements for the degree of

Master of Science (MSc)

Wien, 2018 / Vienna 2018

Studienkennzahl lt. Studienblatt / degree programme code as it appears on the student record sheet:	A 066 877
Studienrichtung lt. Studienblatt / degree programme as it appears on the student record sheet:	Genetik und Entwicklungsbiologie/ Genetics and Developmental Biology
Betreut von / Supervisor:	Univ. Prof. Dr. Walter Berger

This Master Thesis was conducted at the

Medical University of Vienna

Department of Medicine I

Institute of Cancer Research

Applied and Experimental Oncology

Borschkegasse 8a

1090 Vienna

Supervised by

Univ.Prof.Dr. Walter Berger

Bernhard Englinger, MSc

Mag. Daniela Lötsch, MSc, PhD

"The most exciting phrase to hear in science, the one that heralds new discoveries, is not „Eureka!" but rather, "Hmmm…that's funny."

Isaac Asimov

Acknowledgements

"I began to realize how important it was to be an enthusiast in life. If you're interested in something, no matter what it is, go at it full speed, embrace it with both arms, hug it, love it and above all, become passionate about it. Lukewarm is no good."

Roald Dahl

First of all, I would like to thank *Univ. Prof. Dr. Walter Berger* for the opportunity to work in his laboratory and be part of his team. I am very grateful to have the possibility to learn a tremendous amount about so many different aspects of science and oncology in particular. Thank you for all your help, for sharing your knowledge with all of us and for preparing us to become independent researchers, but most of all, thank you for the open-door policy and down to earth attitude that makes a person feel like home.

Next, I would like to thank *Mag. Daniela Lötsch, MSc, PhD, Bernhard Englinger, MSc,* and *Lisa Gabler, MSc,* for being an enormous help in expanding my scientific knowledge, for showing me new methods and introducing me more into the world of molecular biology. Most importantly, thank you for supervising me and teaching me how to analyze data in a precise and critical manner.

To all the other team members, thank you for always being willing to explain and support everyone, for answering all of my so many questions and for the nice and cozy lunches, dinners, drinks and parties, this makes working in such a great team even greater! A special gratitude for their patience goes to *Christine Pirker, Dominik Kirchhofer, Diana Groza* and *Mirjana Stojanovic*.

I would also like to thank *Prof. Michael Grusch* for spreading his knowledge on cloning and FGFRs, and *Dr. Sabine Spiegl-Kreinecker* and her team for enabling me to work with their established cell models.

Thank you *Korbinian* for your patience. I know it is not always the easiest with me, but even in the most stressful situations, you are the one that supports me and cheers me up. I am happy to have found you and grateful for the life -full of love, health happiness, family and friends- we have here in Austria, The Netherlands, England and Germany.

Last but definitely not least, I want to say thank you to all my *friends* and *family* in The Netherlands but also in Austria for making my life such a happy one. I could not be more blessed with such an amazing group of people around me!!

Table of contents

1. Introduction

The World Health Organization (WHO) provides health-related statistics of disease subcategories (e.g. maternal mortality, childhood mortality, communicable diseases (CD), noncommunicable diseases (NCD) and many more) [2]. NCDs such as diabetes, chronic respiratory diseases, cancer and cardiovascular diseases are the number one cause of worldwide mortality [2, 3]. Globally, 40 million of 56 million diseased people died due to NCDs in 2015. In Europe, NCDs were responsible for 86% of all deaths in 2015 [2]. Since decades, the numbers of new cases affected by NCDs are increasing worldwide. Thus, it is predicted that death, induced by NCDs will rise even more, resulting in approximately 52 million deaths in 2030. Of these NCD related deaths, 25% is expected to be caused by cancer [4].

1.1. Cancer: the numbers

Of the 15.2 million cancer cases, 8.8 million patients died in 2015. This mortality rate accounts for one out of six deaths worldwide [2, 5]. After cardiovascular diseases, which takes the lives of approximately 17 million humans each year, cancer is globally the second leading cause of death [5]. In Europe, 3 million patients suffering from cancer are diagnosed each year and, in addition, this disease is responsible for 20% of all deaths (1.7 million) each year [2].

Taking together all cancer cases, 90-95% occur due to environmental and lifestyle factors, whereas only 5-10% is related to an inherited genetic defect (figure 1) [6]. Low intake of vitamins via nutrition, poor physical activity, obesity (20.9% in Austria), use of tobacco and abuse of alcohol (46% and 10.3%, respectively in Austria) are common risk factors in the development of NCDs in general and of cancer in specific (figure 1.C) [7].

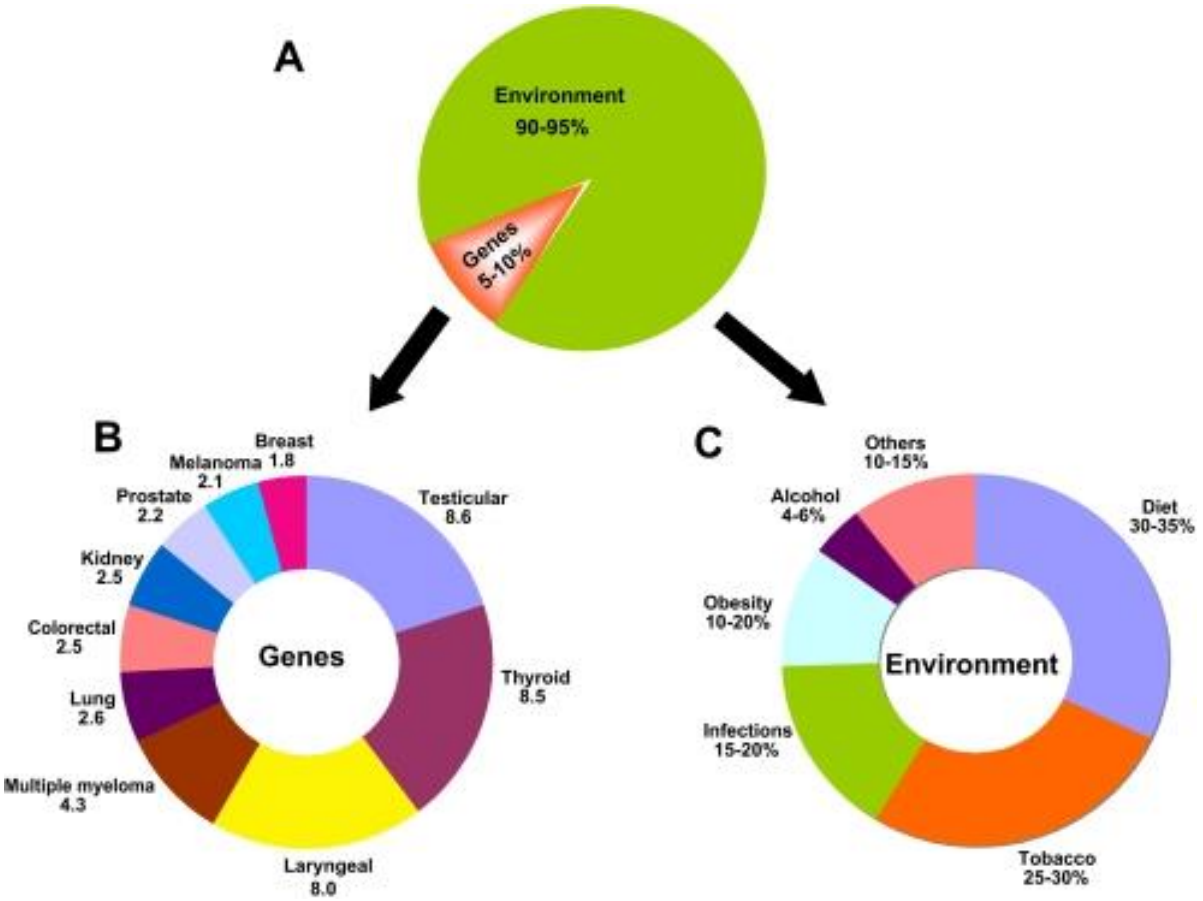

Figure 1. Cancer development and the role of genetic and environmental risk factors. A) Overall risk of cancer development divided into environmental/lifestyle risks and inherited genetic defects, B) Indication what cancer types are caused by familial genetic defects and to which extent. Numbers indicate the ratio of familial risks, C) Subdivision of the single environmental risks and their contribution to cancer development, shown in percentage [6].

Albeit the enhanced cancer risk, these factors are still part of daily human routine [8]. In addition, viral infections and chronic diseases such as hepatitis B virus (HBV) infections or (chronic) inflammatory bowel diseases (IBD) are predisposing factors for cancer development [9, 10]. HBV is known to cause hepatocellular carcinoma (HCC) in a large subset of patients, whereas IBDs play a role in the development of colorectal carcinomas [9, 10].

1.2. Cancer: the disease

As mentioned above, cancer is a serious health problem accounting for every sixth death worldwide. Therefore, expanding knowledge about this disease is very important in the evolution of understanding tumor development [4, 7, 11].

1.2.1. Cancer research history

The disease “cancer” is well described since the beginning of written history. In 1775, Percivall Pott described the development of squamous cell carcinoma in the lungs of chimney sweepers [12]. Further, Rudolph Virchow found a connection between cancer and inflammation (1863), the first mastectomy to treat breast cancer was performed in 1882 by William Halsted, Hilário de Gouvêa published preliminary findings on the inheritance of cancer and additionally, X-rays were discovered by Wilhelm Roentgen in 1895 (figure 2) [12]. Yet, more advanced cancer research started in the early 1900s leading to novel anticancer treatment using radiation-, hormonal-, and chemotherapy. Further, new findings were described regarding the development of cancer, such as immune surveillance, the correlation between smoking and lung cancer and the detection of cervical cancer using Pap smear (discovered by George Papanicolaou in 1928) [12].

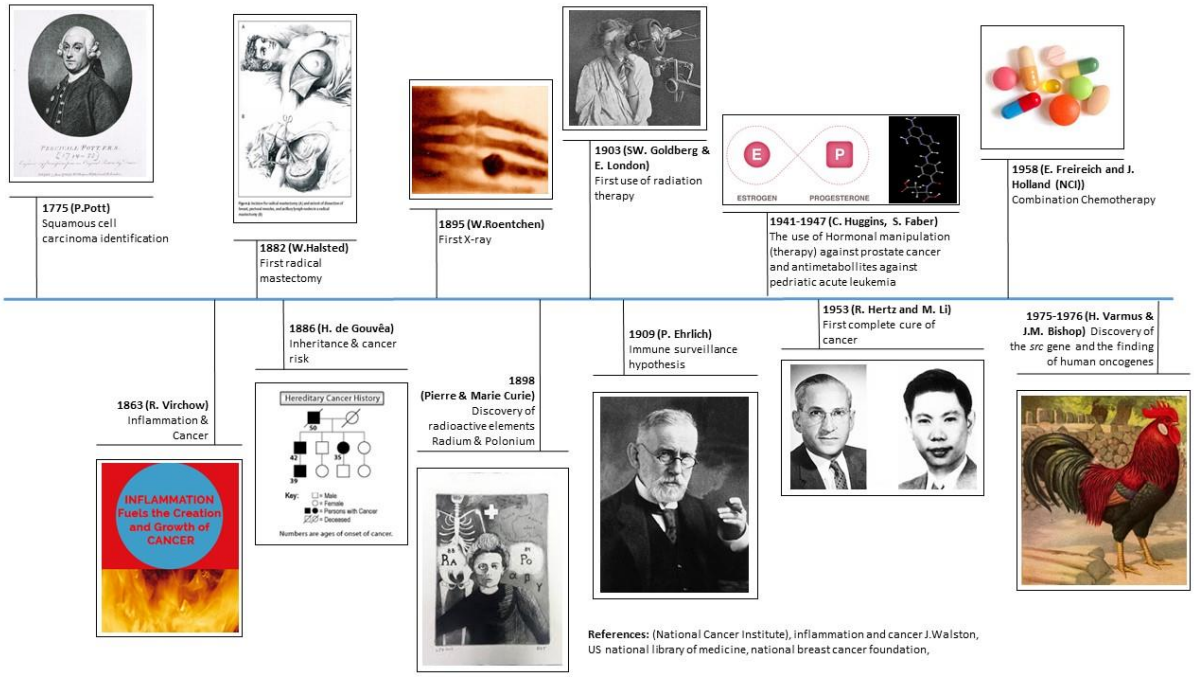

Figure 2. Cancer-related research history from the late 1700s until the late 1900s. This timeline includes life-changing findings, such as the correlation between inflammation and cancer, inheritance and the risk of cancer, first X-ray use, radiation-, hormone- and chemotherapy and the discovery of oncogenes. Data in the timeline and pictures are adapted from the National Cancer Institute (NCI) [12].

Molecular cancer biology found its breakthrough in 1971, when a lot of money became available during President Nixon's leadership [13]. In 1975-1976, the Varmus-Bishop discovery of the first proto-oncogene (a gene that due to mutations can become an oncogene) named *src* (sarcoma), encoding a non-receptor tyrosine kinase, changed the view on the development of cancer [13, 14]. This study revealed that cancer is a genetic disease, inducible by retroviral transfection of a mutated gene into healthy cells, thus transforming these cells into malignant cells [13]. To follow up these findings, more and more researchers performed viral DNA transfections to induce malignant cell transformation via oncogenes [13]. Furthermore, the effect of mutagenic carcinogen exposure was analyzed in 1979 by Shih *et al*., who found transformed DNA in the normal healthy cell genome [13, 15]. The evolution in molecular tumor biology went on when DNA sequencing found its place in cancer research. In 1980 and afterwards, DNA sequencing data indicated that even small changes in the DNA, such as single point mutations, could transform a proto-oncogene into an oncogene. Since the application of DNA sequencing, many proto-oncogenes were identified (e.g. *RAS, ERBB2, ERK, MYC*) [12, 16].

Taken together, cancer research deepens our understanding of the disease and supports improvement of procedures for diagnosis and detection, therapeutic strategies (with focus on the molecular level), surgical approaches with focus on the different tumor types and eventually improve patient outcome [17, 18]. Thus, the evolution in cancer research and the continuous development of molecular functions are a major help in the battle against cancer.

1.2.2. Development of cancer

Cancer is a somatic disease of the genome and globally the second leading cause of death in the cluster of NCDs [17, 19]. Histological science was a big step in the process of understanding the origin of cancer cells [16].

Tumor formation occurs when cells start to proliferate in an uncontrolled manner. However, malignant cell transformation is a multistep process [20, 21]. Three main steps concerning the development of a malignant phenotype are described: i) tumor initiation, ii) promotion and iii) progression (figure 3) [22]. Furthermore, the

phenotype and histology of precancerous and cancerous lesions can indicate the stage of disease progression [22].

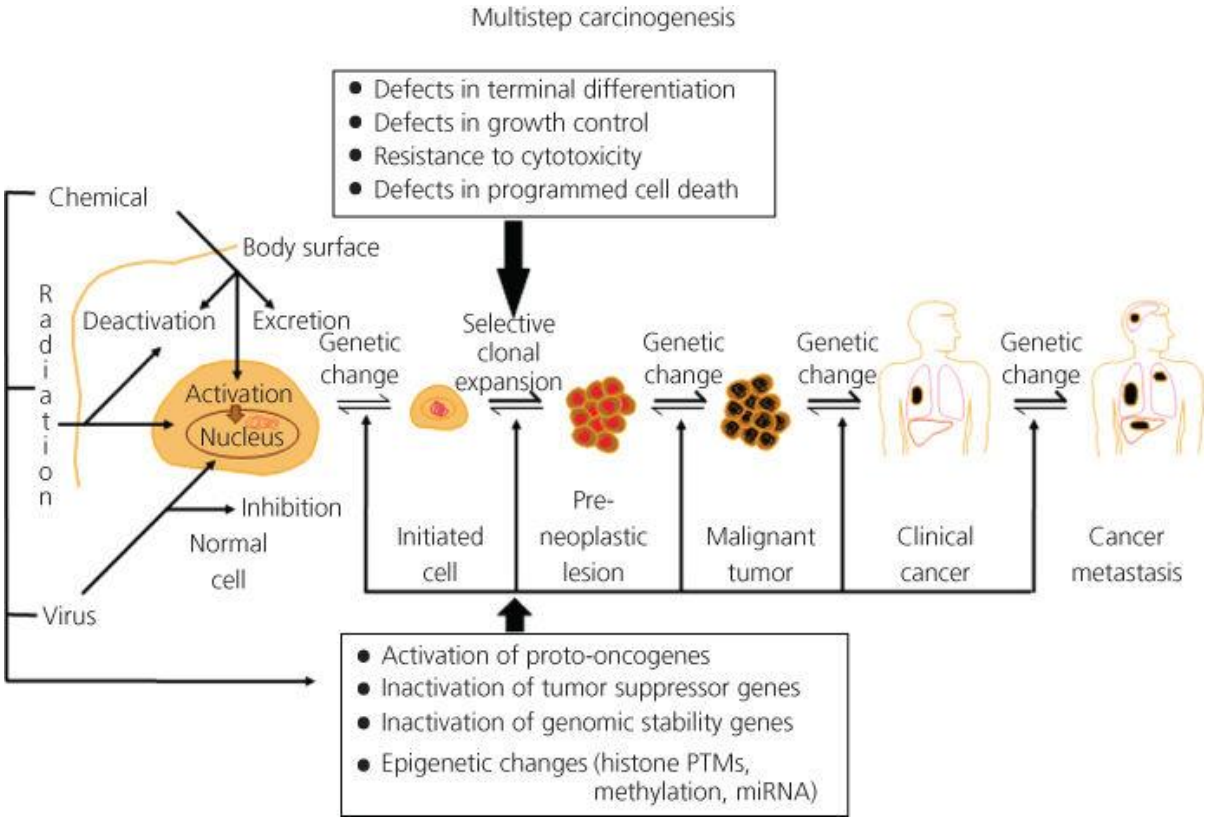

Figure 3. Multistep carcinogenesis. The development of tumors is a multistep process depending on multiple environmental factors and is subdivided into three main stages, i) initiation, ii) promotion and iii) progression [23].

Cancer categorization is based on the anatomical characteristics, histological features, proteomics data, gene expression, invasiveness of the cells into the surrounding tissue as well as on metastatic potential [18].

It became clear that cancer can be separated into two clusters, i) the non-invasive, encapsulated benign tumors and ii) the invasive and metastatic malignant tumors [16]. Furthermore, benign tumors are named after the tissue of origin with an addition of “-oma” at the end of the word (e.g. adenoma, teratoma), whereas malignant tumors (cancers) are divided in epithelial- (carcinomas) and non-epithelial subtypes [16]. Non-epithelial cancers are i.e. i) sarcomas (deriving from bone and soft tissue), ii) lymphomas (originating from the B- and T-lymphocytes), iii) germ cell tumors (grown from sperm or egg cells), iv) leukaemias (deriving from different cell types of the

hematogenous lineage) and v) blastomas (formed out of embryonic and incompletely differentiated cells) [11, 16, 24].

Alterations in the genome and epigenome, including mutations, regularly lead to the development of malignant cells [25]. Error-prone DNA replication, unfaithful DNA repair and enzyme-induced DNA modifications are key factors in mutagenesis [26]. Additionally, exogenous mutagen exposure plays a substantial role in some cancer types (e.g. ultraviolet light (UV) in skin cancer and tobacco smoke in lung cancers) [26].

1.2.3. Hallmarks of cancer

In the year 2000, Douglas Hanahan and Robert A. Weinberg wrote an article in which they characterize cancer according to major common hallmarks, followed by an updated version published in 2011. These hallmarks describe the biological processes during malignant tumor development and are an attempt to break down the complexity of the disease to a set of universal molecular principles that define cancer [27-29]. The hallmarks described in 2000 comprise i) evading growth suppressors, ii) enabling replicative immortality, iii) resisting cell death, iv) sustaining proliferative signaling, v) inducing angiogenesis and vi) activating invasion and metastasis [27, 29]. In 2011, two enabling characteristic features, namely genome instability as well as tumor-promoting inflammation were described. Further, two emerging hallmarks (deregulating cellular energetics and avoiding immune destruction) were added to the six existing hallmarks of cancer (figure 4) [27].

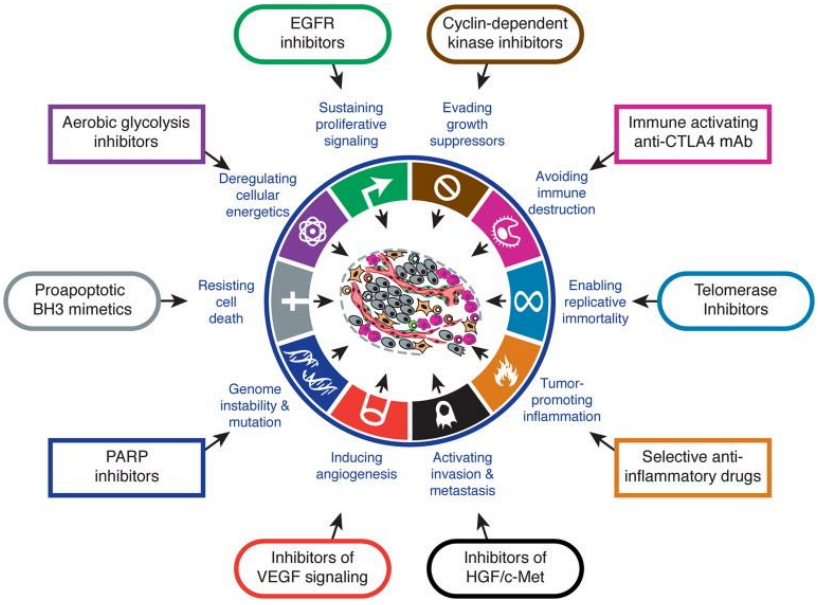

Figure 4. The hallmarks of cancer and their respective therapeutic targets [27]. Depicted are the six hallmarks of cancer, defined 2000. Additionally, the four novel hallmarks i) avoiding immune destruction, ii) tumor-promoting inflammation, iii) genome instability & mutation and iv) deregulating cellular energetics are included. Strategies to therapeutically target these traits are mentioned to the respective hallmark [27].

Importantly, a tumor is a complex tissue consisting of heterogenous cell populations forming a mass of fast proliferating mutated cells [19, 27, 30]. Each population of cancer cells can regulate specific biological processes in the tumor tissue [27]. By this, malignant cells communicate with the tumor stroma to activate healthy cells during the development of malignancies [27, 30]. Therefore, not only the single cellular components but also the total neoplastic tissue and the tumor-microenvironment (including surrounding tissue) are of importance when trying to understand tumorigenesis [27, 30].

Evading growth suppressors & sustaining proliferative signaling

Cell growth and proliferation in healthy organisms is controlled by a large set of proteins involved in cell cycle regulation. Main cell cycle phases are the G1-phase (resting phase), S-phase (DNA synthesis), G2-phase (between S- and M-phase, preparation for mitosis), M-phase (mitosis) and the G0-phase (quiescence/senescence) [31]. Healthy tissues regulate proliferation via an “on & off” of growth and proliferation-stimulating factors. Additionally, during cell cycle progression, each cycle is strictly controlled to maintain cell number homeostasis [29, 30, 32]. The so-called tumor suppressor genes are responsible for guided cell cycle progression and its negative regulation in case mutations or DNA damages occur [27, 29, 30]. Two prominent tumor suppressive proteins are the retinoblastoma-associated (RB) protein and p53. Both tightly control cell proliferation such as cell cycle stalling, senescence or apoptotic signaling activation upon DNA damage [27, 29, 30]. Mutations in these tumor suppressor genes lead to continuous DNA synthesis and cell division even when damaged DNA is included [27, 31]. For example, wild-type p53 functions as transcription factor that is stabilized after activation by its negative regulator MDM2, causing ubiquitination of p53 [33]; whereas on the contrary, mutated p53 (e.g. missense, nonsense, frameshift mutations) loses the tumor suppressor function, causing several pro-tumorigenic changes [27, 34].

Altered proliferation pathways in cancer cells increase the turnover rate and may keep growth signals “on” continuously [27, 30]. Most frequently, mutations affect oncogenic drivers and proliferative signaling such as receptor tyrosine kinase (RTK) associated pathways (e.g. epidermal growth factor receptor (EGFR) mutations). RTKs contain intracellular tyrosine kinase domains responsible for phosphorylation of

downstream proteins [27, 30]. Furthermore, mutated tumor suppressors fail to control the cell cycle or block proliferative signals, thus, no suppression of proliferation occurs [27, 30].

Taken together, mutations within tumor suppressor genes can help tumor cells to evade growth suppressors and enables the cells to proliferate without any interference of inhibitors and inhibiting signals, therefore, driving cancer progression [35].

Resisting cell death & enabling replicative immortality

As mentioned above, apoptosis is a strictly regulated mechanism of cell death and serves as cellular protection against general different alterations, including mutations. Apoptotic signaling is induced by both intrinsic and extrinsic signaling factors activating the machinery [27, 29]. Both pro-apoptotic as well as anti-apoptotic proteins play major roles in the intracellular apoptotic regulation [16, 17]. Members of the Bcl-2 family are either pro- or anti-apoptotic proteins, e.g. Bcl-2 and Bcl-xl are anti-apoptotic regulatory proteins, while Bax and Bak work in a pro-apoptotic manner [27, 29].

Additionally, cellular replication is regulated tightly and is limited in healthy cells, however, during malignant transformation, cells are in need of unlimited replication abilities [31]. Therefore, cancer cells try to gain their immortal state by evading senescent and apoptotic signals resulting in rapid cell proliferation and outgrowth into large cell clusters forming a heterogenous population [31].

Inducing angiogenesis & activating invasion and metastasis

Rapidly dividing cells, homing in the tumor tissue, are in urgent need of high oxygen and nutrients supply and fast disposition of metabolic waste [27]. Angiogenesis, the process of new blood vessel formation, takes place when tumors grow beyond a certain size (in general 1-2mm^3) [32]. Microscopic pre-malignancies already require angiogenesis and therefore malignant cells abuse the vascularization and angiogenic signaling systems to obtain more nutrients and oxygen allowing the tumor tissue to grow efficiently [32, 36]. Frequently observed tumor-secreted growth

signals like thrombospondin-1 (TSP-1) and vascular endothelial growth factor-A (VEGF-A) are responsible for blood vessel growth [27, 29]. In addition, vascular permeability and endothelial sprouting is induced by the expression of VEGF-A receptor tyrosine kinases 1-3 (VEGFR 1-3) [27, 29].

Via these newly formed blood vessels or already existing lymphatic- and blood circulation system, cancer cells can migrate through the body and spread the disease [37]. Invasion is often the first step towards metastasis and stands for the event that cancer cells penetrate the surrounding tissue without using any circulating system; whereas, during metastasis, malignant cells can travel via the blood and lymphatic system to other organs and invade the tissue at the distant site (figure 5) [27, 37]. Hence, this process is known as the “invasion-metastasis cascade” and depicts the main steps leading the migratory process of cancer cells [27, 29]. The main steps are, i) primary cancer cells are released into the surrounding tissue (invasion), ii) cancer cells enter the bloodstream via intravasation and survive to iii) travel through the circulation and lymphatic system and reach distant target tissues, iv) where the cells enter via extravasation and adapt to the new microenvironment to start proliferation and form (micro-) metastasis [27, 29]. Epithelial like cells are mostly unable to enter the process of invasion and metastasis, therefore, they undergo epithelial to mesenchymal transition (EMT) to enhance their migratory potential.

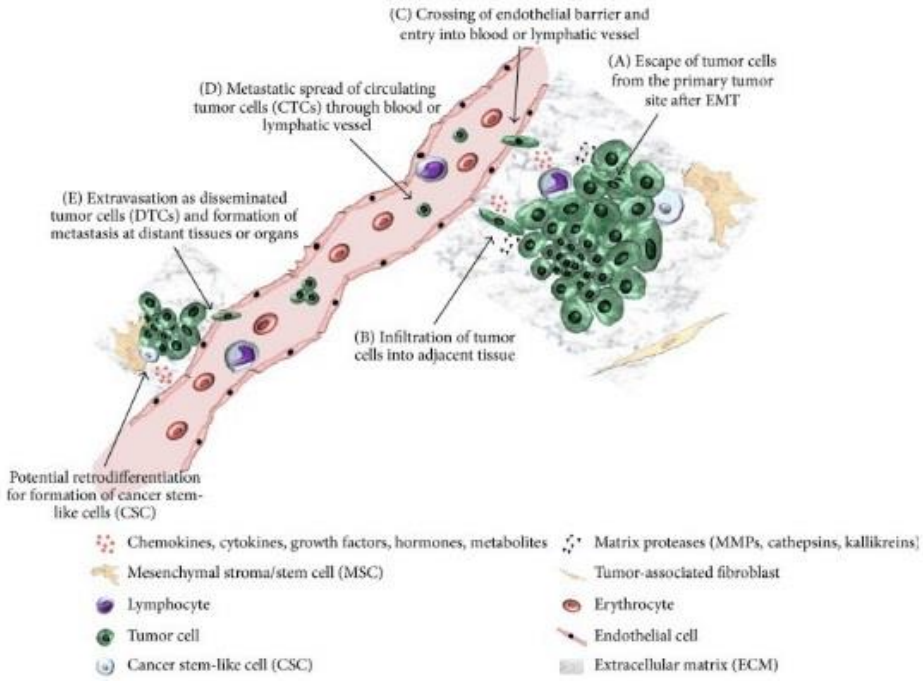

Figure 5. Metastatic route via EMT [38]. The five main steps of the invasion-metastasis cascade are shown including the cell types involved in this process. Tumor cells undergo EMT, they invade surrounding tissue or intravasate to travel via the blood- or lymphatic system, exit the circulating system and form a tumor at the distant site (metastasis).

EMT is a well-known process during embryonal development which improves the migratory characteristics of cells [37]. Cancer cells make use of this process, adapting the embryonal abilities to survive and metastasize. During this conversion, epithelial (-like) cells gain migratory potential and change their phenotype to more mesenchymal characteristics (e.g. polarity of the cells, cytoskeletal disorganization) by deregulating cell-cell adhesion proteins such as cadherins and catenins [37, 39]. Once EMT takes place, migration, invasion and metastasis are promoted [39]. Furthermore, cells can convert from mesenchymal to epithelial-like cells (MET) again by upregulating epithelial markers like E-cadherin [37, 39].

The four additional hallmarks

Taken together, cancer cells are able to evade growth suppressors and keep on proliferating, they become immortal, induce angiogenesis to obtain more oxygen and can invade and metastasize [27, 29]. Additionally, malignant cells can avoid the immune system, deregulate cellular energetics to gain more energy and make use of inflammatory signals and genome instability, promoting tumorigenesis [27, 29].

The healthy body is constantly observed by the immune system (e.g. B- and T-lymphocytes, NK-cells and macrophages) to detect pathogens and abnormal cells [27, 29]. Cancer cells can “hide” from these immune cells and evade the detection and

elimination via the immune system [27, 29]. Moreover, cancer cells can even use the inflammatory signals secreted by the infiltrated immune cells as tumor promoting factors [27, 29]. Molecules (i.e. VEGF, tumor necrosis factor- α (TNF-α)) released by activated immune cells stimulate regrowth of damaged tissue. In turn, these molecules can positively influence and facilitate tumorigenesis [27, 29].

Rapidly and uncontrolled proliferating cells are dependent on an enhanced metabolism [27, 29]. Thus, cancer cells exhibit the ability to alter the normal glucose metabolism to aerobic glycolysis (Warburg effect) to quicken energy production [40, 41]. During normal respiration, cells use glycolysis to metabolize glucose to pyruvate followed by oxidative phosphorylation in the mitochondria, where pyruvate is oxidized to CO_2 and H_2O [40]. Oxidative phosphorylation generates 36 adenosine triphosphate (ATP) molecules per glucose [40, 41]. Cancer cells deregulate glycolysis and switch to aerobic glycolysis (e.g. under hypoxic conditions), during which pyruvate is metabolized, followed by direct conversion to lactic acid, instead of entering the mitochondria and undergoing oxidative phosphorylation (figure 6) [40, 41]. Aerobic glycolysis is less efficient and produces low amounts of ATP. The low levels of ATP can be compensated in the cancer cells by upregulating glucose transporters (e.g. GLUT1) [40]. This upregulation and the increase in glucose uptake is frequently correlated to activation of oncogenes [27, 40].

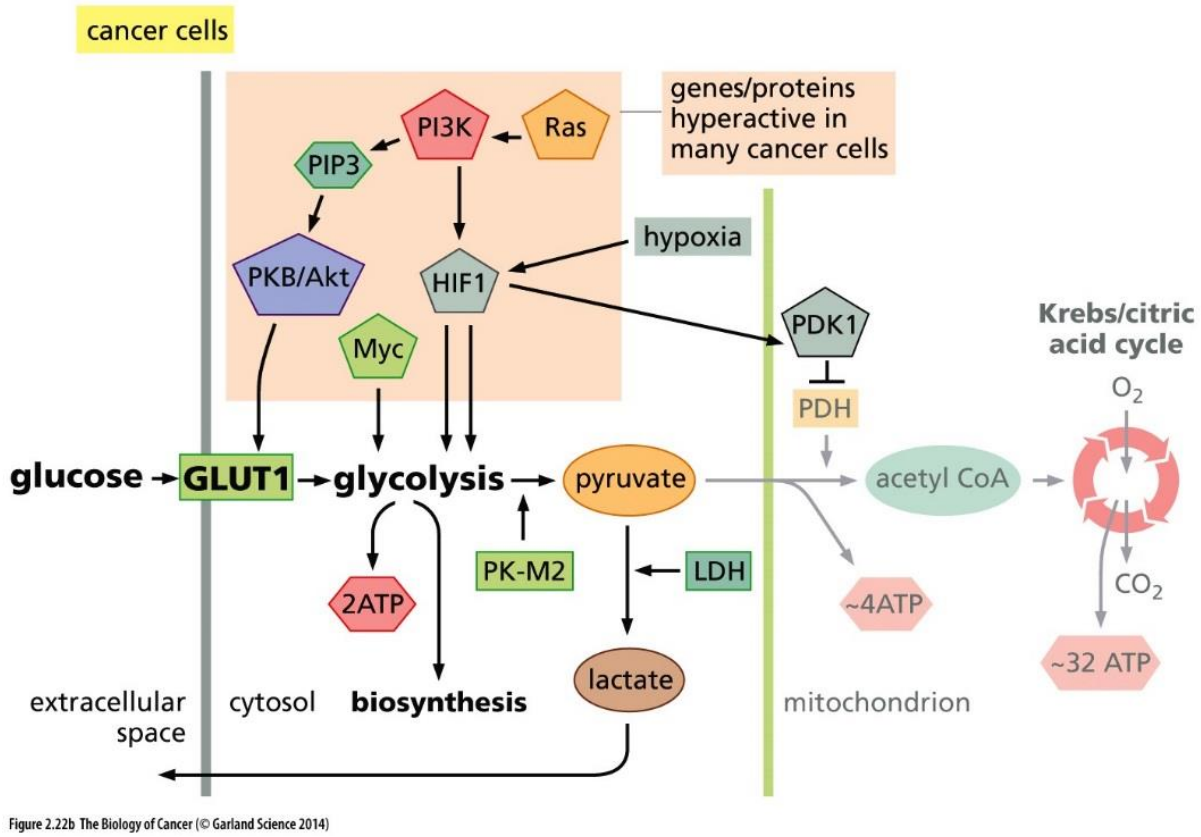

Figure 6. Altered glucose metabolism in cancer cells. Cancer cells frequently make use of the aerobic glycolysis (Warburg effect) leading to quick glucose metabolism but low ATP production [41].

1.2.4. Tumor microenvironment

The accumulation of malignant cells alone is not sufficient enough to establish a well-functioning tumor [42]. Therefore, accurate distribution and interaction of malignant cancer cells (CC), cancer associated fibroblasts (CAF), immune inflammatory cells (ICs), cancer stem cells (CSC), pericytes (PC) and endothelial cells is necessary to form the tumor and microenvironment (TME, figure 7) [41, 42]. The majority of non-malignant cell types is associated with growth and proliferation during normal development and therefore, these cells mostly exhibit tumor-promoting characteristics, which help the tumor to expand [41-43].

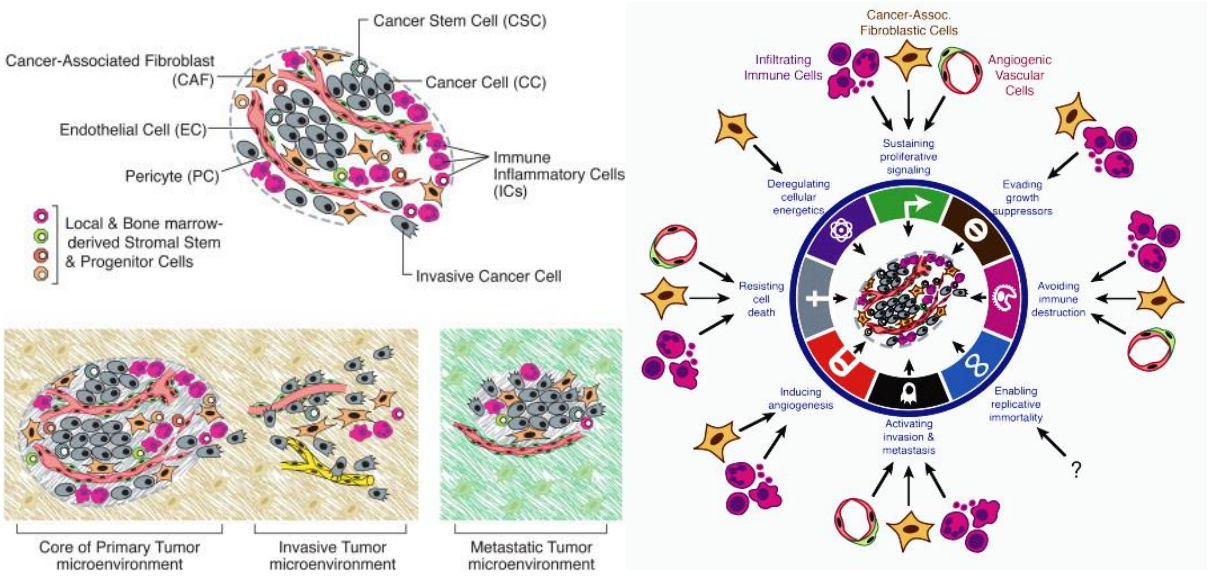

Figure 7. The tumor microenvironment. A set of cell populations forming the tumor microenvironment are depicted in the left panel [26] and, in addition, each cell type is further sub-divided according to their involvement in a particular hallmark (right panel [43]).

1.3. Anticancer therapy

The history of anticancer compounds started in 1939 with Charles Huggins' idea of using chemical hormones for prostate cancer treatment and continued with Sidney Faber in 1942, who used antimetabolites to treat leukemia (figure 2) [44]. The main aim of anticancer therapy is the complete removal of malignant cells from the body. Thus, several topic and systemic strategies such as surgery, radiation and chemotherapy are applied [45, 46]. The most promising, and in many cases curative strategy to treat cancer is a combination of surgery, radiation and systemic drugs [47]. Therapy scheme selection strongly depends on the tumor type, the progression, the location in the body and the physical condition of the patient [47, 48].

1.3.1. Surgery

In most patients, surgery remains the standard treatment method applied in the battle against cancer [49]. Nevertheless, removal of all malignant cells, even after complete resection, is often complicated and recurrence may occur [49]. Accordingly, a combination of several therapeutic approaches mostly increases a patient's prognosis [48].

1.3.2. Chemotherapy

Chemotherapy is often administered as treatment to cure cancer (neoadjuvant or adjuvant chemotherapy) or to prolong life (palliative chemotherapy) [50]. This type of therapy is usually non-specific and inhibits proliferating cells by causing irreversible DNA damage leading to inhibition of proliferation or cell death [44]. Standard chemotherapy affects malignant but also rapidly dividing healthy cells, leading to major side effects [45, 46]. Therefore, managing physical (but also psychological) side effects is of high importance to improve the patient's quality of life during anticancer therapy [51, 52]. Fatigue, pain and emotional stress are the most common side effects of chemotherapy [53]. Anemia, bleeding, hair loss, immune suppression, skin rash and heart damage are additional side effects often related to chemotherapy due to its non-specific characteristics [53].

Subclasses of chemotherapeutic agents are antimetabolites, toxic antibiotics, alkylating agents, topoisomerase inhibitors and microtubule interfering molecules [41,

44, 54]. Cisplatin, accidentally discovered as an anticancer agent by Rosenberg, 40 years ago, is one of the best-known chemotherapeutic agents worldwide [55]. At first, cisplatin was found to show promising biological properties in bacteria, followed by anticancer activity in mouse models and finally approval of cisplatin for human anticancer treatment (figure 8) [55].

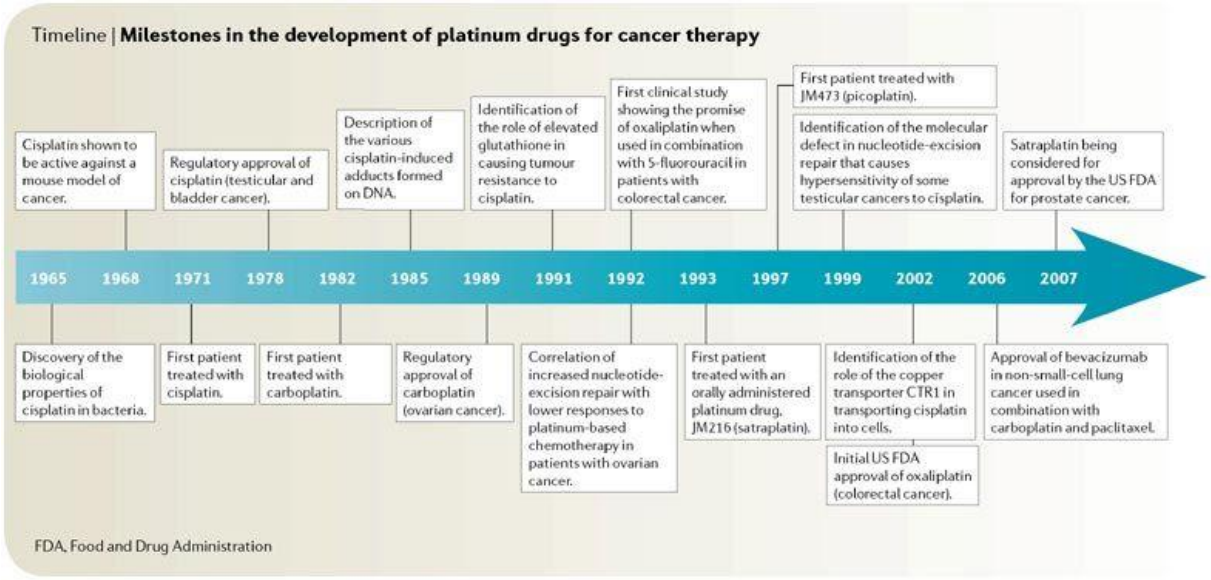

Figure 8. Milestones in the development of platinum drugs for cancer therapy. The history of cisplatin discovery and approval and the development of other platinum compounds to treat malignancies [55].

1.3.3. Hormone therapy

Hormone therapy is applied in gender specific cancer types driven by hormonal changes. Prostate cancer was the first cancer type treated with synthetic hormones in 1939, so called androgen-deprivation therapy (ADT) [44, 56]. Another example of hormonal therapy is the use of anti-estrogenic therapy to treat breast cancer (estrogen receptor-positive tumors) and the use of aromatase inhibitors [56].

These synthetic hormones, used for hormone therapy, interfere with the standard hormonal household in the body and therefore bear great risk of developing metabolic syndromes (e.g. dyslipidemia, insulin resistance) [56, 57].

1.3.4. Immunotherapy

The major histocompatibility complex (MHC) on tumor cells presents tumor antigens towards the T-cell receptor (TCR), present on T-lymphocytes, and thereby

triggers an antitumor immune response [58]. This process is regulated by the so-called “immune checkpoint” molecules located on T-cells [58]. Cytotoxic-t-lymphocyte-associated protein 4 (CTLA-4) and programmed cell death receptor 1 (PD-1) are extensively investigated immune checkpoint receptors involved in the immune response against cancer cells [58]. The activity of these checkpoint receptors is regulated via a balanced system consisting of co-stimulatory and inhibitory signals [59].

The most promising way to eliminate cancer cells from the body via the immune system, is by blocking specific immune checkpoints [59]. In 2011, the first immune checkpoint inhibitor, targeting CTLA-4, was approved by the FDA [48]. Checkpoint inhibition is based on the blockage of co-inhibitory signals, restoring T-cell functions [28]. Antibodies directed to PD-1 like nivolumab and pembrolizumab and to its respective ligand (PD-L1), such as atezolizumab, were widely used in clinical trials and showed promising results [28]. Accordingly, several therapeutic antibodies, e.g. i) pembrolizumab (2014), ii) nivolumab (2015), iii) avelumab (2017), iv) inotuzumab (2017) have been approved by the FDA as anticancer therapeutics [60-63]. However, ineffective treatment with PD-1-targeting antibodies have also been described during clinical trials, indicating the complexity of anticancer therapy and the ability of tumor cell clearance by the immune system [27, 28]. Hence, the use of immunotherapy in combination with conventional therapy and targeted therapy is worth the consideration [64].

1.3.5. Targeted therapy

The major aim of targeted therapeutic strategies is the specificity of the compounds and the reduction of side effects. An example of targeted therapeutic agents are renowned tyrosine kinase inhibitors (TKIs) [47]. TKIs are small molecules, exhibiting the ability to bind to the intracellular kinase domain of RTKs. Intracellular kinase domains are frequently mutated, transforming the receptor from a proto-oncogene into an oncogene [41, 65].

By binding the intracellular kinase domain, the inhibitor directly interferes with the ATP binding ability and prevents phosphorylation, thus causing the receptor to stay inactive [65]. Blockage of the RTKs results in the disruption of downstream signaling cascades and, subsequently, inhibition of cancer cell proliferation [65, 66].

1.3.6. Radiotherapy

The use of radiation to treat cancer was first applied in 1903 by *Goldberg* and *London* after the discovery of the X-ray by Röntgen in 1895 [41]. Röntgen observed the impact of X-ray on healthy tissue, namely, burns and necrotic tissue damage [41].

Adjuvant radiotherapy has made its way into standard cancer treatment schemes. Post-operational focal application of radiotherapy is supposed to reduce relapse risk, frequently in combination with adjuvant chemotherapy [41].

1.3.7. Therapy resistance

Intrinsic or acquired drug resistance are the main limitations in cancer treatment [67]. Prior to the application of anticancer therapy, 50% of all patients already exhibit intrinsic resistance, whereas a great amount of the other half will develop resistance towards the applied drugs (acquired resistance) [67].

Generally, the mode of action of all antineoplastic drugs is damaging essential driver molecules resulting in reactive oxygen species (ROS), DNA damage, cell cycle arrest, senescence, apoptosis or necrosis [68]. By modifying target genes, alteration of signaling pathways or activation of efflux pumps, drug resistance can be acquired [68]. Consequently, single agent resistance can occur and, in addition, cross-resistance against multiple drugs that are mechanistically unrelated is probable [68-70]. This multidrug-resistance (MDR) phenotype is mainly acquired upon overexpression of MDR-related proteins (MRP) belonging to the ATP-binding cassette (ABC) transporter family [68-70].

1.4. Brain development and malignancies

The central nervous system (CNS), and in particular the brain, is said to be the center of every functioning human being [71]. Therefore, the embryonal development of the CNS is tightly organized and defects mostly lead to early termination of pregnancy.

1.4.1. Development of the human central nervous system

Formation and evolution of the human brain depends on tight signaling structures during embryonal development [71]. Epigenetic factors play major roles in regulating development-related genes resulting in differentiation of stem cells into cells contributing to a functional brain [71, 72]. Maternal- and fetal factors are the two players influencing the epigenetic-related functions during embryonal development [72]. Alterations in fetal epigenetic regulations can be induced by maternal factors such as exposure to e.g. smoking, stress, incomplete nutrition, alcohol abuse and other environmental influences [72, 73]. Embryonal epigenetic changes are frequently caused by fetal factors such as insufficient nutrient transport via the placenta and fetal hypoxia, leading to early birth and low body weight [72, 73].

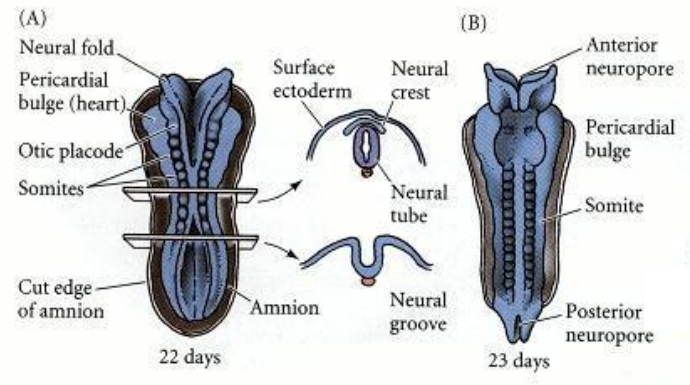

Figure 9. Formation of the neural tube (neurulation) during embryogenesis [74]. (A) Dorsal and transverse sections of a 22-day human embryo initiating neurulation. Both anterior and posterior neuropore are open to the amniotic fluid. (B) Dorsal view of a human embryo during neurulation a day later. The anterior neuropore region is closing while the posterior neuropore remains open.

Embryonic brain development

The CNS, and thus the brain, develops during the embryonal gastrulation stage (third week of pregnancy) from the ectodermal layer [75]. The neural plate thickens at the edges and forms so-called neural folds, folding the sheet of ectodermal cells into a tube, eventually forming the neural tube (figure 9) [75]. At the tip of these neural folds,

neural crest cells (NCs) appear and migrate in lateral direction from the neural tube to the periphery [75]. These NCs give rise to many cell types, some of them are the sensory ganglia cells and glia cells [75]. After complete closure of the cranial neuropore, the brain is split up in three sections, the brain vesicles, the forebrain (prosencephalon), midbrain (mesencephalon) and hindbrain (rhombencephalon) [75]. The prosencephalon is sectioned in two parts (i.e. the telencephalon and the diencephalon) during further development (figure 10A) [75]. While the mesencephalon stays nearly unchanged, the rhombencephalon splits up in myelencephalon and the metencephalon, which will give rise to the pons and cerebellum at a later stage (figure 10B) [75].

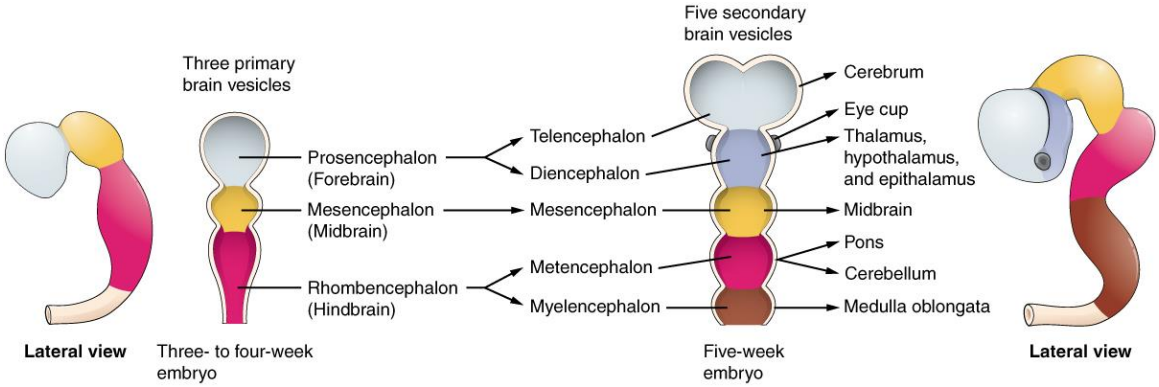

Figure 10. Embryonic development of the brain [76]. A) Early brain development, indicating the three primary brain vesicles, formed in three- to four- week old embryos, B) Five-week old embryonic stage includes formation of the secondary brain vesicles including from top to bottom the i) telencephalon, ii) diencephalon, iii) mesencephalon, iv) metencephalon and v) myelencephalon. Included are structures of the brain formed out of the five secondary brain vesicles.

Neuroblasts (primitive neural cells) arise by neuro-epithelial cell division after neural tube closure [75]. Neuroblasts exhibit the ability to migrate and differentiate, and when they do so, they develop into neurons and lose the ability to divide (figure 11.B, left differentiation panel) [75]. Furthermore, neuroepithelial cells can give rise to primitive gliablasts. Depending on the layer these blasts arise from, they differentiate into fibrillar- or protoplasmic astrocytes (in the mantle layer) or turn into oligodendroglia (in the marginal layer, figure 11.B, middle panel) [75]. Neuroepithelial cells, skipping the differentiation into neuro- or gliablasts, develop into ependymal cells (figure 11.B, right panel) [75]. In a later stage during brain development when the nervous system is additionally supported by blood vessels (induced angiogenesis), microglia, deriving from mesenchymal cells, migrate into the brain and serve as neuronal macrophages (figure 11.A) [75].

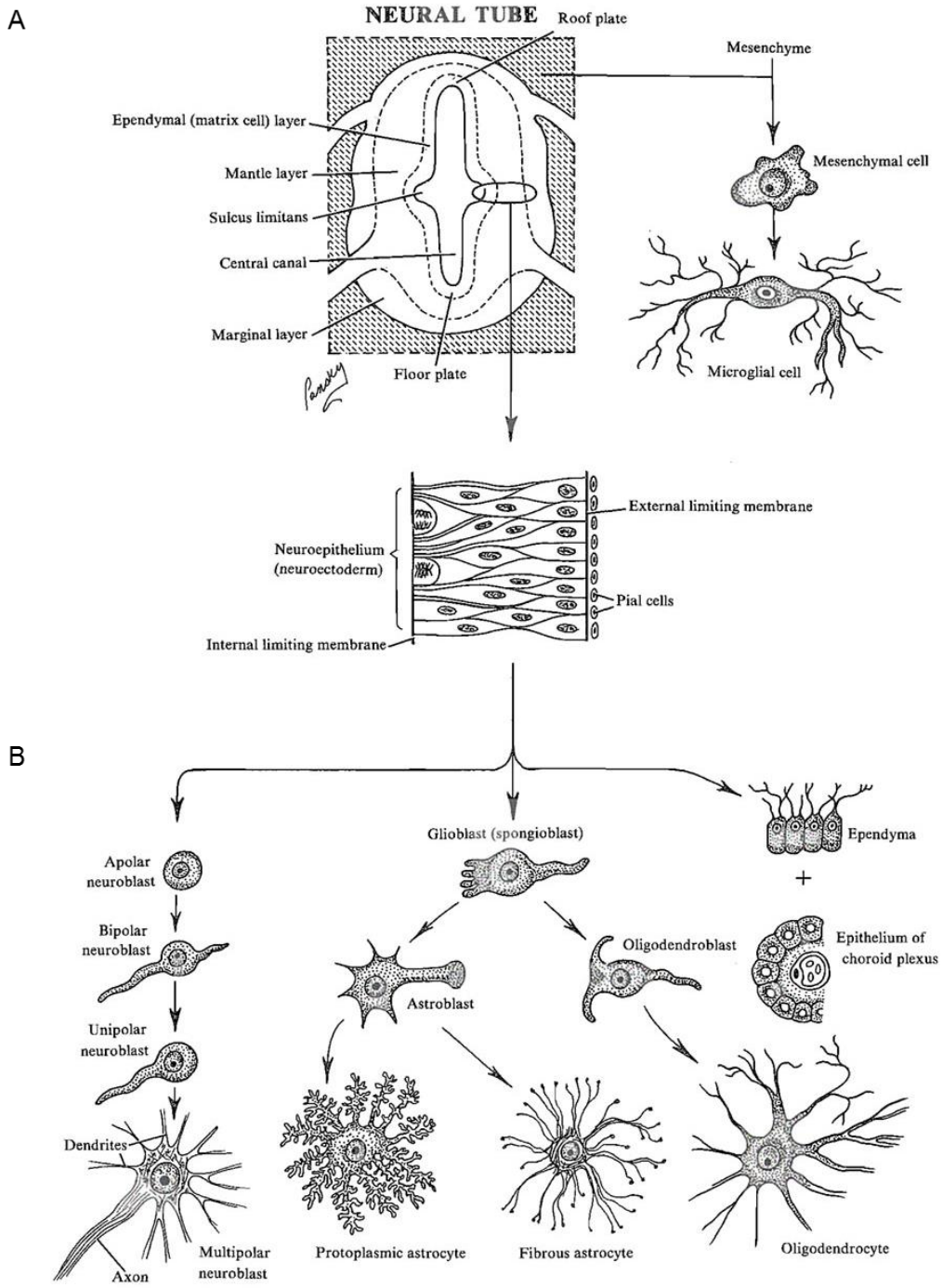

Figure 11. Embryonal development of CNS cells [77]. A) Microglia (brain macrophages) derive from the mesenchyme, surrounding the neural tube. B) The left differentiation scheme indicates the differentiation of an apolar neuroblast into multipolar neuroblasts harboring dentrites and an axon (losing the ability to devide), the middle panel indicates the differentiation of glioblasts into astrocytes and oligodendrocytes whereas the right panel indicates the ependymal cells.

1.4.2. Diagnosis of central nervous system neoplasia

Symptoms indicating brain tumors are often very unspecific. Consequently, intracranial tumors are frequently diagnosed at advanced stages. Occurrence of brain tumor related signs and symptoms strongly depend on the localization of the tumor

and the rapidity of progression. Seizures, strong headache, nausea and vomiting, dizziness, visual defects and speech disorders are examples of symptoms indicating brain neoplasia [78]. To localize, diagnose and identify the tumor type causing a subset of these symptoms, magnetic resonance imaging (MRI), computed tomography (CT), positron-emission tomography (PET) and MR-spectroscopy are performed [78, 79]. To identify the source of the patient's symptoms, CT is mostly performed. This technology provides millimeter thin layered brain pictures [78, 79]. Additionally, MRI enables highly detailed analyses of the size, shape, location and depth of invasion of the malignant tissue in the brain [78, 79]. Further, MR-spectroscopy may provide additional information about the intra-tumoral metabolism which is distinct in more aggressive tumor types (figure 12) [78]. Concerning both CT and MRI, necrosis, inflammation and edema are not always clearly to distinguish from tumor tissue [78-80]. Therefore, PET, measuring metabolic activities (e.g. Warburg effect) is a good tool for clinicians to identify the tumor type [78, 80]. Generally, metabolic alterations are very helpful in the differentiation between certain tumor types (e.g. CNS lymphoma and high-grade glioma) [78, 80]. To identify the tumor tissue on histological level, biopsies are frequently taken from the neoplastic site in the brain.

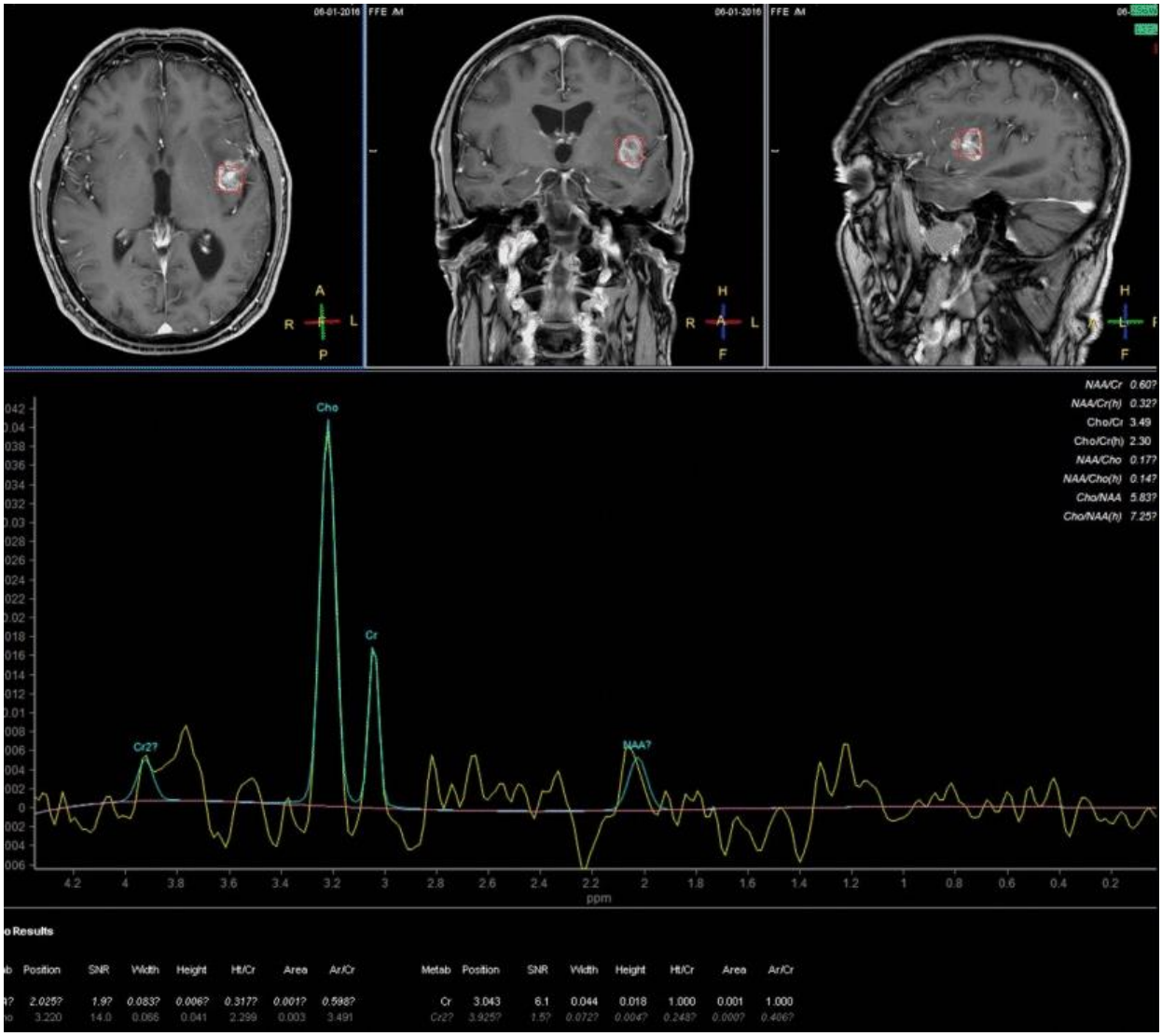

Figure 12. MR-spectroscopy of a patient with GBM [78]. Metabolite spectra can help in the classification and grading of CNS tumors. The enriched choline values and reduced N-acetyl-aspartate (NAA) are a classic indication for GBM [78].

1.4.3. Tumors of the central nervous system

WHO Classification

In 2007, the WHO classified CNS tumors according to their morphological features and grouped all astrocytic tumors separately from oligodendroglial tumors [81]. This classification is mainly based on similarities between the tumor cells and its normal counterparts in the brain [81]. A WHO-CNS classification update in 2016, in addition to the old classification, changed the categorization of CNS tumors by using molecular characteristics in addition to histology (appendix 2) [81]. The incorporation of molecular parameters has led to improved diagnosis of astrocytic tumor types [81]. Accordingly, the diagnostic use of genetic features, in particular isocitrate

dehydrogenase 1 (IDH1), alpha thalassemia retardation syndrome X-linked (ATRX) and 1p19q deletion support the identification of either astrocytoma or oligodendroglioma [81]. Nevertheless, the phenotypic classification remains a major aspect of the CNS tumor classification due to unclear mutation patterns in a subset of tumors [81]. Additional genetic classification markers are TP53, Wnt and RELA [81].

To demonstrate the variety and complexity of the WHO-CNS classification, some tumors are listed in appendix 1, including diffuse or anaplastic astrocytomas, oligodendroglial tumors, glioblastoma (and other astrocytic types), ependymomas, additional gliomas, choroid plexus tumors, pineal region tumors, neuronal and neuronal-glial tumors, embryonal tumors (e.g. medulloblastomas), meningiomas, lymphomas, germ cell-related tumors and many more [81].

It is assumed that gliomas derive from transformed neural stem- or progenitor cell populations. These premalignant precursors undergo several genetic alterations, leading to primary malignant brain neoplasias [82, 83]. The WHO classified gliomas into four groups, related to the grade of malignancy of which grade I astrocytoma is least malignant with good prognosis and grade IV glioblastoma is highly malignant and indicates poor prognosis [83].

Glioblastoma and Gliosarcoma

Glioblastoma multiforme (GBM) is a high-grade malignant glioma and the most aggressive primary brain tumor, also classified as WHO grade IV astrocytoma [81, 84, 85]. The tumor tissue of GBM is very heterogenous (multiforme) characterized by various drug-resistant cell populations and by high vascularization [82, 86]. GBM can be subdivided into *IDH*-wildtype, accounting for 90% of all cases, indicating primary GBM and *IDH*-mutant tumors, taking 10% of all cases into account and mostly indicating secondary GBM [81, 87]. Worldwide, 4% of cancer-related deaths are linked to GBM, making it one of the deadliest tumor types with a median overall survival time of 14 months [81, 88].

Primary GBM is known to be an aggressive, fast progressing, invasive (i.e. into the parenchyma of the brain) tumor, mostly occurring in older patients (>55 years old) [85, 87]. On the contrary, secondary GBM derived from low grade (WHO II or III) astrocytomas, are mainly found in younger patients (<45 years old). Both GBM types

are similar on microscopic level but differ in their genetic patterning (figure 13) [87]. One major difference on the genetic level is the presence of an *IDH1*-mutation in secondary GBM, while primary GBM lack this alteration [87, 89]. Furthermore, in up to 75% of primary GBM tissue, mutations in the telomerase reverse transcriptase (*TERT*) gene have been detected, compared to 20-40% in secondary GBM [90, 91]. O^6-methylguanine DNA methyltransferase (*MGMT*) promoter hypermethylation occurs in 40-60% of primary GBM in contrast to 75% of secondary GBM cases [87, 92, 93].

Representing a small subgroup of GBM (1-8% of all cases), are the so-called gliosarcomas (GS) [94]. This group of high-grade gliomas either recur due to relapse after radiotherapy or develop *de novo*. The GS tissue is heterogenous and the genetic patterns are similar to those of GBM. GS and GBM share the same origin of development but, however, GS exhibits sarcomatoid compartments in addition to glial cells [94].

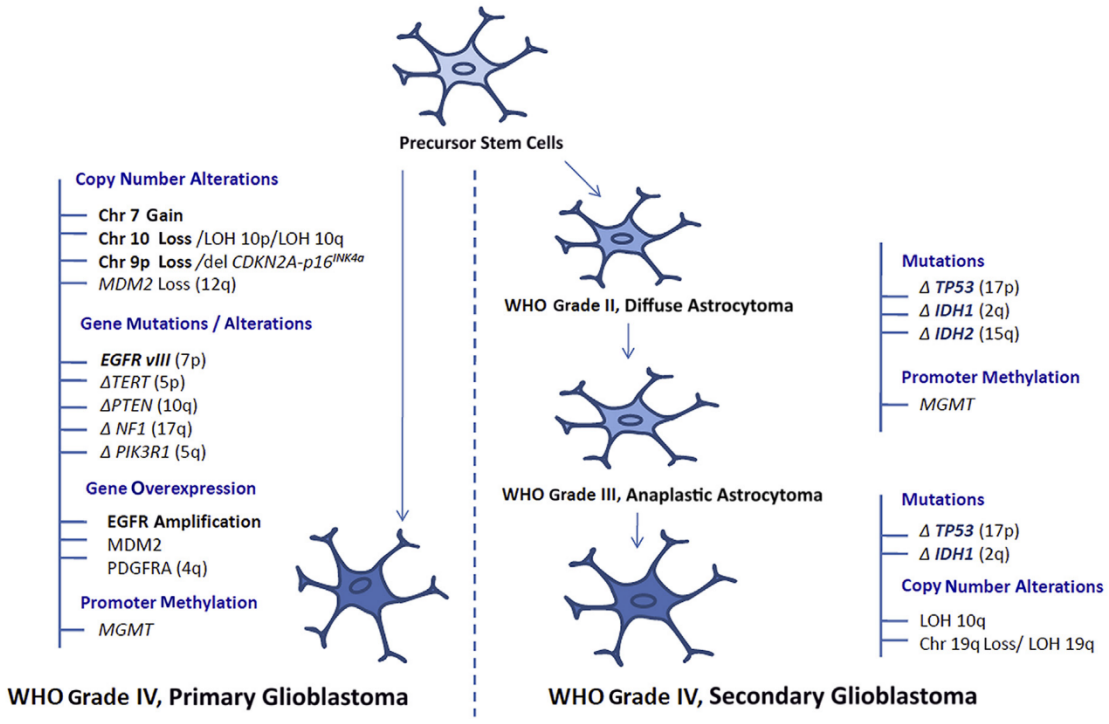

Figure 13. Differentiation of precursor stem cells into glioblastomas [87].

Isocitrate dehydrogenase 1 (IDH1)

Isocitrate dehydrogenase 1 (*IDH1*) mutations are already detected in low-grade gliomas, thus, they are believed to play a pivotal role during the development towards secondary GBM [79, 82, 95, 96]. Somatic point mutations are responsible for most of

the *IDH* mutations leading to an enzymatic gain-of-function (GoF) [79, 82, 95-97]. *IDH1* mutations are found in 83% of all secondary but only in 5% of all primary GBM cases. No statistically significant differences on median survival and progression-free survival rates are found between *IDH1* mutated primary and secondary GBM [82].

O^6-methylguanine-DNA-methyltransferase (MGMT)

O^6-methylguanine-DNA-methyltransferase (MGMT) is a protein that repairs DNA damage by removing adducts from O^6-guanine bases [82, 83, 95, 98, 99]. Tumors characterized by elevated MGMT expression levels are frequently related to resistance against anticancer therapeutics [82, 95, 98, 99]. Accordingly, cells harboring an epigenetically silenced (methylated) *MGMT* promoter show enhanced sensitivity (up to 10-fold) towards alkylating (DNA-methylating) agents [82, 95, 99].

1.4.4. Glioblastoma therapy

Newly diagnosed GBM patients receive the gold standard therapy including maximum tumor resection, radiotherapy and administration of temozolomide (TMZ) concomitantly, followed by adjuvant TMZ-therapy [82, 85, 88]. TMZ is an alkylating agent, synthesized as a prodrug in form of a tablet [82]. TMZ causes G2/S-phase arrest, autophagy and apoptosis by DNA damage via methylation of O^6 and N^7 guanine bases. However, this damage is often rapidly repaired by the protein MGMT [82, 89, 95, 98, 99]. Therefore, *MGMT* promotor-methylated GBM patients exhibit higher benefits from TMZ treatment as compared to unmethylated *MGMT* promotor GBM patients [82].

Due to the distinct heterogeneity of these tumors, treatment of the total cell population is difficult, hence, recurrence appears in the majority of patients [82]. The re-growing tumor tissue frequently depends on the homing of glioma stem cells (GSCs) within the heterogenic GBM tumor [83]. GSCs are able to self-renew and differentiate into various brain-specific lineages or keep the stem cell characteristics to build a pool of GSCs in the tumor tissue [83, 98, 100]. Hence, GSCs are of major interest in therapy resistance and GBM recurrence [83, 100].

Furthermore, drug delivery into the brain tumor tissue is very complex and frequently reduced due to the inefficient penetration of the blood-brain barrier (BBB) [82]. This barrier separates the blood circulation system from the brain parenchyma but likewise also complicates the delivery of substances into the neoplastic tissue [82].

Drug efflux pumps belonging to the ABC transporters (e.g. P-glycoprotein (P-gp) (also known as multidrug resistance protein 1 (MDR1)) and multidrug resistance-associated protein 1 (MRP1) are expressed by brain endothelial cells and are one of the major players causing inefficient drug delivery into brain tumors [82, 101].

Summarized, GBM is hard to treat and therefore a type of cancer with major relapse probability and one of the highest mortality rates [82, 89, 98]. Consequently, personalized medicine is of major interest to treat patients individually based on their genetic, epigenetic and phenotypic tumor characteristics.

1.5. Receptor tyrosine kinases (RTKs) and cancer

Receptor tyrosine kinases (RTKs) are proteins located in the cell membrane consisting of an extracellular ligand binding domain, a transmembrane domain and an intracellular kinase domain [102, 103]. Intracellular signaling is initiated when ligands bind to the receptor, leading to receptor dimerization and auto-phosphorylation of the intracellular tyrosine kinase domains [104]. Subsequently, tyrosine auto-phosphorylation starts intracellular signaling transduction responsible for cellular growth and proliferation, migration and survival [104]. EGFR-, fibroblast growth factor receptor (FGFR)-, Ret-, vascular endothelial growth factor receptor (VEGFR)- and the anaplastic lymphoma kinase (ALK) families are important members of the superfamily of RTKs [105].

Genetic alterations affecting RTKs and their signaling cascades are often identified as drivers of gliomagenesis [106]. Variable mutations present in astrocytomas, and thus in GBM, are found in EGFR, platelet derived growth factor (PDGF/PDGFR), phosphatase and tensin homologue deleted on chromosome 10 (PTEN), Rb, IDH, ATRX and TP53 [104, 107]. Downstream signaling circuits, frequently affected by these mutations, disturb cell cycle regulation (TP53-MDM2 or Rb), or hyperactivate Ras/RAF/MAPK, JAK/STAT and PI3K/AKT pathways (figure 14) [104, 106, 108, 109]. Copy number variations and sequence alterations in modulators related to these pathways increase the risk of neoplastic transformation and uncontrolled progression [104, 106].

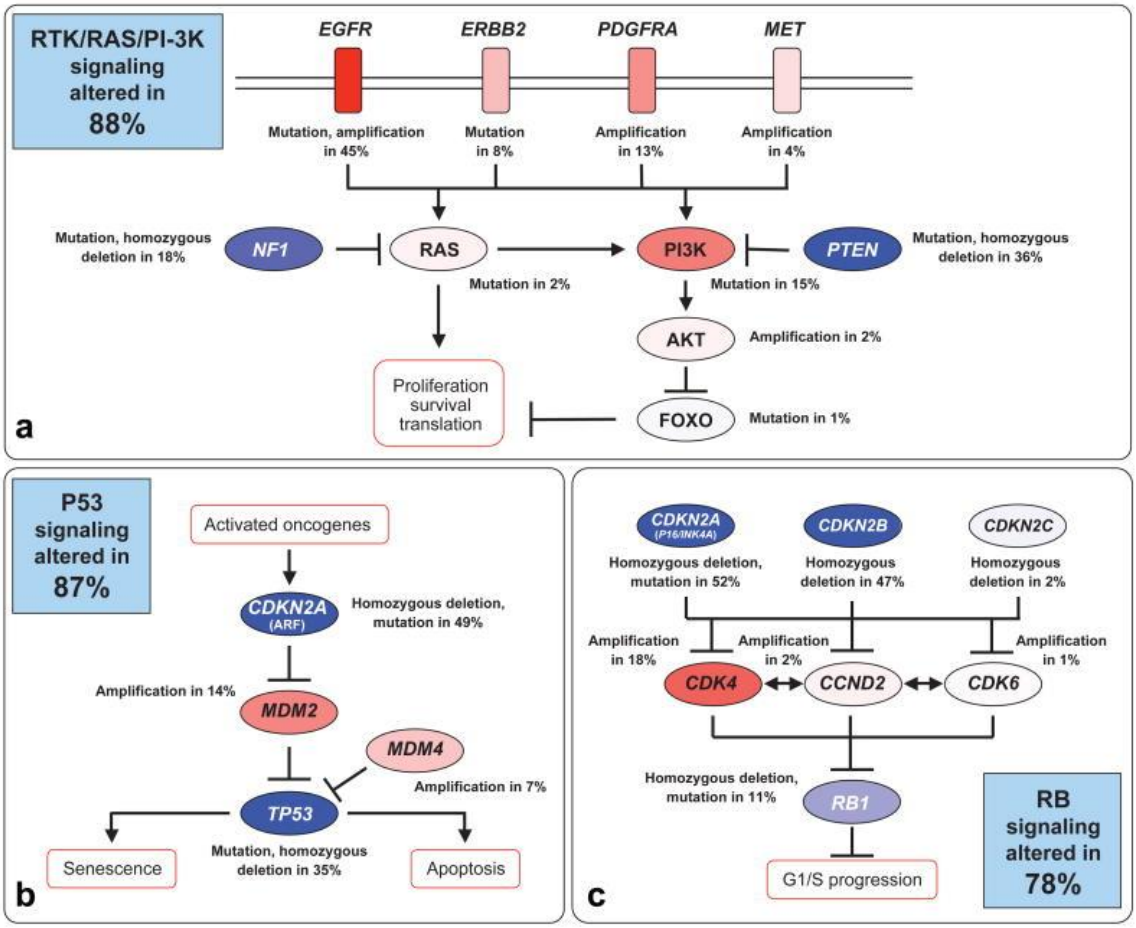

Figure 14. Three main signaling pathways frequently altered in GBM cases [106]. One of the three pathways pictured above is mainly altered in GBM development, including A) RTK/RAS/PI-3K, B) P53, and C) RB [106]. Sequence and copy number alterations are depicted by percentage and indicated per affected gene. Red indicates activation, blue shows inactivation, respectively. The intensity of the color pattern depends on the increase in % [106].

In detail, 36-50% of GBMs harbor a loss or mutation in *PTEN* leading to 80% activation of AKT [108]. Furthermore, *EGFR* mutation or amplification is observed in 40-45% of all GBM patients, indicating the importance of these genes in driving carcinogenesis [108]. Inhibition of mutated genes in GBM is the main target in development of new therapeutic strategies. So far, PDGFR inhibition indicated insufficient activity in GBM patients and only a small subgroup of patients (10-20%) benefits from inhibitors targeting EGFR [108].

1.6. Fibroblast growth factor receptors and their ligands

Fibroblast growth factor receptors (FGFRs) are RTKs and are activated upon binding of their corresponding growth factors (FGFs). FGFRs serve as major regulators in cell homeostasis, angiogenesis, wound repair and embryogenesis [110]. The overall RTKs signaling is known to be part of processes such as proliferation, migration and apoptosis [110].

To date, four *FGFR (FGFR1-4)* and 22 *FGF* genes are known [111]. These 22 *FGF* genes are divided into seven subgroups, all containing between two and four members, based on evolutionary changes (figure 15 A) [1]. The production of intracellular FGFs is regulated by the FGF11 subfamily, providing non-signaling FGFs (cofactors) [1]. Subfamily FGF15/19 stands for endocrine FGFs binding FGFRs including cofactor Klotho, whereas the subfamilies FGF1, FGF4, FGF7-9 encode canonical FGFs, binding FGFRs (including heparin as cofactor) [1]. Furthermore, each subfamily includes a subset of FGFs which are very versatile with respect to receptor binding specificity (table 1.) [1].

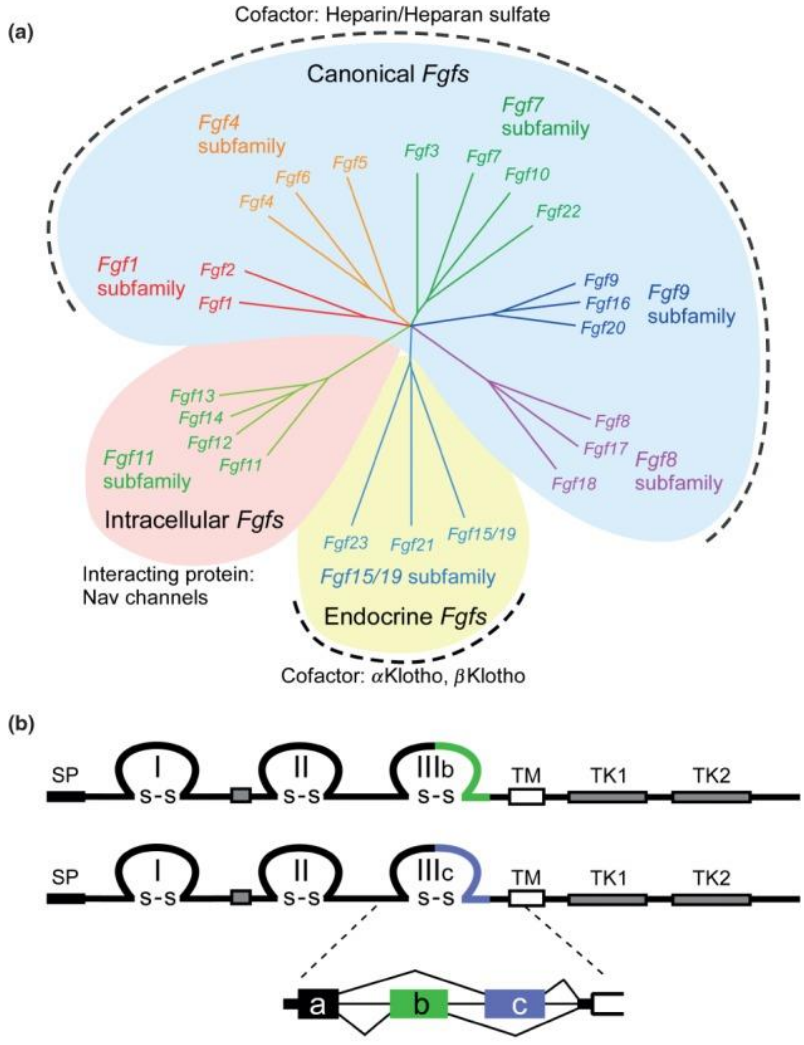

Figure 15. FGF grouping with focus on the evolutionary genetic distance (A) and the structural arrangement of FGFRs schematically depicted (B) [1].

Variation in binding affinity and specificity of FGFs towards FGFR1-4 strongly depends on the c- and n-terminal sequences of the ligands [112, 113]. The involvement of FGFs in pathogenesis is linked to loss-of-function (LoF) or GoF mutations [112, 114].

Table 1. FGF subfamilies and their respective FGFs and FGFR affinities [1].

FGF subfamily	FGF	Cofactor	Receptor specificity
FGF1 subfamily	FGF1		All FGFRs
	FGF2		FGFR 1c, 3c > 2c, 1b, 4Δ
FGF4 subfamily	FGF4		FGFR 1c, 2c > 3c, 4Δ
	FGF5		
	FGF6		
FGF7 subfamily	FGF3	+ Heparin or Heparan sulfate	FGFR 2b > 1b
	FGF7		
	FGF10		
	FGF22		
FGF8 subfamily	FGF8		FGFR 3c > 4Δ > 2c > 1c >> 3b
	FGF17		
	FGF18		
FGF9 subfamily	FGF9		FGFR 3c > 2c > 1c, 3b >> 4Δ
	FGF16		
	FGF20		
FGF15/19 subfamily	FGF15/19	+βKlotho	FGFR 1c, 2c, 3c, 4Δ
	FGF21		FGFR 1c, 3c
	FGF23	+αKlotho	FGFR 1c, 3c, 4

The four FGF receptors are known for their variety in isoforms and share homologous protein sequences of 55-72% [115, 116]. These isoforms are found in FGFR1-3, not in FGFR4, and generated via alternative splicing of the transcripts [115]. Three immunoglobulin (Ig)-like structures form the base of the extracellular binding domain (D1-3) of FGFR, harboring either splice variant b or c, depending on the exon included in the Ig-like structure (figure 15 B) [1, 115]. Variation in the ligand-binding domain interferes with the distinct FGF binding affinity and specificity [112, 115]. FGFR splice variants are frequently coupled to tissue type, in particular splice variant b is majorly present in epithelial cells, whereas c is found in the mesenchyme [112, 117].

The so-called acid box, unique for FGFR molecules, is located between Ig-like domain D1 and D2 [112, 118]. Coupled to D1, this acid box functions as auto inhibitor of the receptor tyrosine kinase [112]. Domains D2 and D3 play important roles in binding ability and sufficiency of FGFs [112]. Upon FGF binding, heparin binding additionally occurs in close proximity of D2 between D2 and D3, thereby strengthening

the binding between ligand and receptor and protecting the ligands from degradation [112, 119].

Cancer development is coupled to somatic mutations in FGFRs [112, 120]. The majority of FGFR-related mutations are GoF mutations in the autocrine signaling of the receptors [112, 121]. FGFR-mutations linked to malignancies are mostly ligand-independent and promote tumorigenesis [112, 121]. For example, FGFR1-related carcinogenesis is coupled to GoF-mutations of the receptor in GBM and prostate cancer patients, whereas FGFR2 kinase domain mutations play an essential role in endometrial cancer development and BRCA-mutated breast cancer cases [112, 122-124]. Germline SNPs causing transmembrane domain mutations in FGFR3 and 4 are frequently found in bladder cancer, rhabdomyosarcoma, prostate cancer, colon cancer and multiple myeloma and often lead to more aggressive infiltration of cancer cells [125]. Furthermore, high expression of FGFR4 in breast cancer is known to play a crucial role in the low response rates upon tamoxifen treatment [112, 122].

1.6.1. Fibroblast growth factor receptor signaling

Activation of FGFRs occurs when two FGFs bind to the extracellular ligand-binding domain [103, 111, 126]. FGFs are either paracrine/endocrine (coming from distant tissues or different adjacent cell types)) or autocrine (originating from the cell itself) ligands [103]. Paracrine FGFs bind to heparin-sulfate proteoglycans (HSPG) followed by FGFR binding, whereas endocrine FGFs bind to both FGFR and the cofactor Klotho (figure. 16) [1, 103, 126]. Upon ligand binding, the two receptors dimerize, leading to conformational shifts in the structure of the receptor and finally to intracellular kinase activation by tyrosine phosphorylation [103, 112, 126].

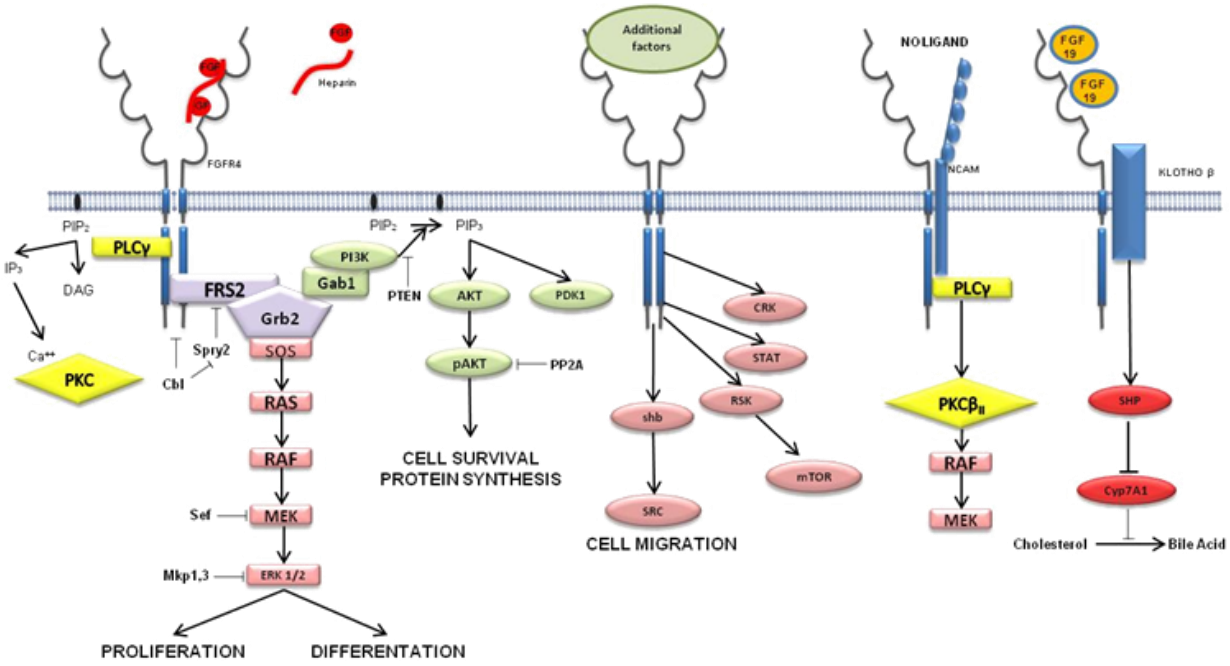

Figure 16. Canonical FGFR signaling pathways majorly responsible for proliferation, survival, differentiation and migration. [http://atlasgeneticsoncology.org].

Activation of the intracellular tyrosine kinase residues takes place upon auto- and trans-phosphorylation, transforming this part of the receptor into a docking site for effectors activating intracellular downstream signaling [127-129]. Ligand binding and activation of the FGFR induces downstream cascades including phosphotidylinositol-3-kinase (PI3K)/AKT, mitogen activated protein kinase (MAPK) and signal transducer and activator of transcription (STAT) (figure 16) [126, 130-134]. Subsequently, transcription factors are activated, e.g. nuclear translocation of STATs, thereby further inducing transcription of target genes [103, 129, 133].

1.6.2. Fibroblast growth factor receptor 4 and its role in cancer

The gene encoding FGFR4 lies on chromosome 5q35.2, the genomic size is 18 Kb, exhibits 18 exons and the mRNA size is 3.1 Kb [135]. FGF19 (mouse homolog FGF15) is one of the main ligands of FGFR4, important in the regulation of hepatic bile acids synthesis [110, 136]. Furthermore, FGF19 belongs to a subfamily of FGF genes responsible for lipid metabolism, glucose uptake as well as phosphate and vitamine D regulation [136].

A well-known alteration in the transmembrane domain of the FGFR4 is a germline single nucleotide polymorphism (SNP) at codon 388 [110, 136]. This

polymorphism in the *FGFR4* gene was discovered several years ago, and causes a change in a codon at position 388 leading to an amino acid conversion from glycine (Gly388) to arginine (Arg388) [137]. The Arg388 variant is associated with enhanced progression and aggressiveness of tumors in breast, liver and colon cancers [125, 138]. Since 2004, it is known that FGFR4 plays a major role in the neoplastic development and progression of prostate cancer [125, 137]. Furthermore, overexpression of FGFR4 has been observed in pancreatic cancer, rhabdomyosarcoma, adrenocortical carcinoma and hepatocellular carcinoma (HCC) patients. In the latter cancer entity, the oncogenic potential of FGFR4 is likely due to its important role in regulation of bile acids production [110, 139].

1.6.3. Previous findings in our laboratory

Several reports in the literature as well as preliminary data generated in our lab point to a contribution of hyperactivated FGFR4 signaling to a malignant phenotype in GBM cells. Importantly, the role of this receptor in GBM/GS is largely unknown. Screening of an extended panel of GBM and GS cell lines established in collaboration with the Department of Neurosurgery in Linz revealed a subset of FGFR4-high expressors that were strongly susceptible to pharmacological FGFR inhibition. Notably, the cytotoxic potential of FGFR inhibitors proved to be even stronger in 3-dimensional growth conditions, representing the so-called cancer stem cell subpopulation. This points to a role of FGFR4 in maintaining a stem cell-like niche in the investigated cell lines, a program which might recapitulate the role of FGFRs in early developmental processes. This was also reflected in ablated growth of xenografted GBM tumors overexpressing a dominant-negative version of FGFR4.

2. Aim of the study

Glioblastoma multiforme (GBM) represents the most common and aggressive type of malignant primary brain tumors. Gliosarcoma (GS), a subgroup of GBM, exhibits a biphasic morphology, harboring besides glial also sarcomatoid components. Despite intensive research in the last decades, leading to a deeper understanding of the genetics and biology of this disease, targetable biomarkers have still not been identified. Therefore, prognosis for patients suffering from GBM or GS remains dismal.

Fibroblast growth factor receptors (FGFRs) are a group of receptor tyrosine kinases representing a complex signaling network that is imperative in tissue development and homeostasis. In malignant cells, aberrant activation of FGFRs exerts pro-tumorigenic effects by employing downstream signaling modules such as the MAPK and PI3K/AKT pathways, which stimulate uncontrolled cell proliferation, survival and metastasis.

This study aims to investigate the contribution of FGFR4 to a malignant phenotype of GBM and GS in order to clarify whether targeting of this receptor might represent a feasible novel treatment strategy. We will address these questions by modifying FGFR4 expression in GBM by genetic engineering.

A small panel of FGFR4 high and low expressing GBM/GS cell lines will be selected and FGFR4 expression levels will be verified by qPCR and Western Blot. FGFR4 expression constructs will be generated in the form of plasmid DNA or viral vectors by cloning the wild-type full length gene bearing a C-terminal GFP tag, followed by transduction of- and overexpression in $FGFR4^{low}$ expressing primary GBM cell lines. After selection of transfected/edited cells, the impact of *FGFR4* manipulation on cell viability, sensitivity towards pharmacological FGFR inhibition, 3D/stem cell-like growth, migration and invasion will be investigated. This technique, along with the establishment of chemically inducible CRISPR/Cas9 in the future will allow us to precisely dissect the oncogenic role of FGFR4 in GBM and GS *in vitro* as well as *in vivo*.

3. Material and methods

3.1. Standard cell culture

Indicated in Table 2 are all human cell lines used during this project. GBM and GS cell lines established in Linz are primary GBM primo-cell cultures (not cultured to immortalization *in vitro*). Cells were grown in their respective media supplemented with 10% fetal calf serum (FCS, PAA, Pasching, Austria), without antibiotics, in a humidified atmosphere at 37°C containing 5% CO_2. Cells were cultured in T25 (25 cm^2) and T75 (75 cm^2) culture flasks and passaged twice a week. For passaging, media and floating cells were removed and trypsin/EDTA (Sigma Aldrich, St. Louis, MO, US) was added to detach cells. After cells were detached, they were split 1:2 up to 1:8 and new media was added into the same flask. Cell cultures were regularly tested for *Mycoplasma* contamination (Mycoplasma kit, Sigma) and cells were constantly monitored before use with help of a Zeiss Primo Vert light microscope and Zeiss AxioCam ERc5s camera (Carl Zeiss microscopy, Germany).

Table 2. Summary of all cell lines used for *in vitro* analyses during this thesis project

Cells lines used in this project			
Cell Line	**Tumor tissue**	**Growth medium**	**Source**
U251MG	GBM grade IV	MEME +NEAA + Pyruvate	ATCC
T98G	GBM grade IV	RPMI 1690	ATCC
HU-MI	GBM grade IV	RPMI 1690	Linz*
PÖ-RU	GBM grade IV	RPMI 1690	Linz*
PU-MA	GBM grade IV	RPMI 1690	Linz*
SI-WA	GBM grade IV	RPMI 1690	Linz*
BTL53	GBM grade IV	RPMI 1690	Linz*
BTL90	GBM grade IV	RPMI 1690	Linz*
BTL1376	GS grade IV	RPMI 1690	Linz*
BTL1377	GS grade IV	RPMI 1690	Linz*
pGli43	Paediatric Alveolar Rhabdomyosarcoma	RPMI 1690	ICR
Hep3B	Hepatocellular carcinoma	MEME	ATCC

MEME: Minimal essential eagles medium (+ 0.2% Na-pyruvate + 1% non-essential amino acids (NEAA), Sigma); ATCC: American Type Culture Collection Manassas, VA; *Established at the neurosurgery and neuropathology departments in the Wagner-Jaureg Hospital in Linz, kindly provided by Dr. S. Spiegl-Kreinecker; ICR: Institute for Cancer Research Vienna.

3.2. Chemicals

Most anticancer compounds used for *in vitro* experiments during this thesis project were dissolved in dimethyl sulfoxide (DMSO, Sigma) to stocks of 10mM. All pure powders were stored at -80°C and working stocks at -20°C in small aliquots to avoid repeated freeze-thaw cycles. Before application, drugs were diluted in culture medium to reduce DMSO concentrations to < 1% in all *in vitro* experiments. The applied compounds, including their chemical structure, type and source are listed in table 3.

Table 3. Compounds used for *in vitro* experiments in this project

Compounds used in this project			
Compound	**Mode of action**	**Source**	**Chemical structure**
Ponatinib	TKI	LC Labs	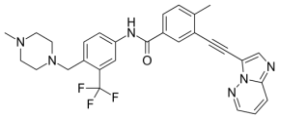
Nintedanib	TKI	Selleckchem	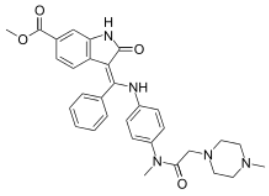
AZD4547	TKI	Selleckchem	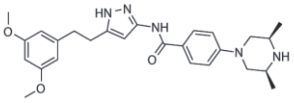
Puromycin	Antibiotic inhibiting protein synthesis during translation	Thermo Fisher	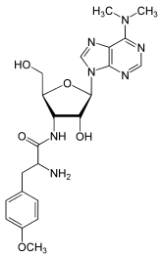

TKI: Tyrosine kinase inhibitor; LC laboratories, Woburn, MA, US; Selleckchemicals, Houston, TX, US; Thermo Fisher Scientific, Waltham, MA, US.

3.3. Cell viability and proliferation analyses

3.3.1. Cell viability assay (MTT)

Background

Anticancer compound screens are frequently performed using cell-based assays *in vitro*. The toxic effect of a compound is investigated by determination of the impact on cell viability as compared to an untreated control.

One method to identify viable cells relies on the reduction of tetrazolium to formazan. The tetrazolium-based cell viability assay applied in this project is called MTT (3-(4,5-dimethylthiazol-2-yl)-2,5-diphenyltetrazolium bromide) and is based on enzymatic and metabolic activity of the cells. Incubation of tetrazolium with viable cells leads to mitochondrial supported metabolic reduction of tetrazolium to formazan, resulting in a brown-orange color change [140]. The intensity of generated color directly correlates to the metabolic activity and viability of the cells. Absorbance can be measured with a plate reader at 450nm and in addition 620nm as reference [140].

Method

Primary glioblastoma cell lines (table 2) were seeded in 96-well plates at a density of 2-4x10^3 cells in 100 µl standard growth medium per well and placed in a humidified atmosphere at 37°C with 5% CO_2 overnight to recover. The following day, drugs (table 3) were diluted in growth medium and added to the cells at the indicated concentration range. In single drug treatment experiments, 100 µl of the 2-fold concentrated compound was added to a final volume of 200 µl per well. After a 72 h incubation time (in a humidified atmosphere at 37°C with 5% CO_2) the population of viable cells was determined by MTT assay, using the manufacturer's procedure (EZ4U, Biomedica, Vienna, Austria). After an incubation time of approximately 3.5 h for all cell lines mentioned in table 2, the color intensity was high enough for analysis. To start a measurement, plates were shaken gently beforehand and color intensity was measured on a plate reader (Tecan infinite 200 pro, Lifesciences, Switzerland) at an absorbance wavelength of 450 nm including 620 nm as reference. Cytotoxic effects were expressed as half maximal inhibitory concentration (IC_{50}) values, calculated by the software GraphPad Prism 5.0 (La Jolla, CA, USA) from dose-response curves.

3.3.2. Clonogenicity assay

Background

The clone formation assay is a classical method, developed in the late 1950's [141]. This assay allows researchers to analyze the capacity of a single cell to proliferate and form a colony [141]. Using this assay, parental as well as transfected cells were investigated to identify the changes in clonogenic potential induced by genetic modifications.

Method

Parental HU-MI and U251MG cells, as well as the transfected sublines were seeded at low cell densities of 1-2 x 10^3 cells per well in 24-well plates, in their respective media. Cells were incubated for 7 days at 37°C under standard conditions to let the single cells generate colonies of about 50 cells. Before fixation with ice-cold methanol (and crystal violet staining), photomicrographs were taken using a Nikon Ti Eclipse fluorescent inverted microscope (Nikon, Tokyo, Japan). After staining the cells with crystal violet (0.1 mg/ml) dark violet, plates were dried to the air and a picture of each well was taken with a Nikon D3200 (Tokyo, Japan). Quantification of clones was carried out by counting the number of clones and measuring the area (μm^2) of the clones using ImageJ software (Java software developed at the NIH).

3.3.3. Soft agar colony formation assay

Background

The idea behind a soft agar colony formation assay is to test the ability of cells for anchorage-independent growth without adhering to a solid support. Culturing plates are coated with soft agar, mixed with growth medium, to interrupt the contact between cells and coated plastic. On the one hand, healthy cells need extracellular matrix (ECM) contact to grow and proliferate, and therefore, to form 2D-clones. On the other hand, transformed cells are less dependent on cell-ECM contact and, in addition to 2D adherent cultures, might be able to form clones in 3D growth conditions. Summarized, the more 3D-clones are formed, the more transformed and, thus, malignant/carcinogenic cells are.

Method

Prior to seeding cells in a density of 5000 cells / well, 6-well plates were coated with a mixture of soft agar (1.2% in ddH_2O) and cell culture medium (1:1) and incubated at 37°C O/N. The left over soft agar mixture was diluted in ddH_2O (1:1) and warmed up to 40°C followed by resuspension of cells in a mix of medium and soft agar mix (1:1). Soft agar-cell mixture was plated onto the coated 6-well plates (figure 17). Polymerization of agar was induced by incubation of the plates at 4°C for 2-5 min. After agar gelling, plates were incubated for 1-2 weeks at 37°C. 3D clone formation was documented and analyzed using photomicrographs using the Zeiss Primo Vert light microscope and Zeiss AxioCam ERc5s camera. Clones were quantified by counting the number of clones formed per well and, in addition, clone areas (µm^2) were calculated using ImageJ.

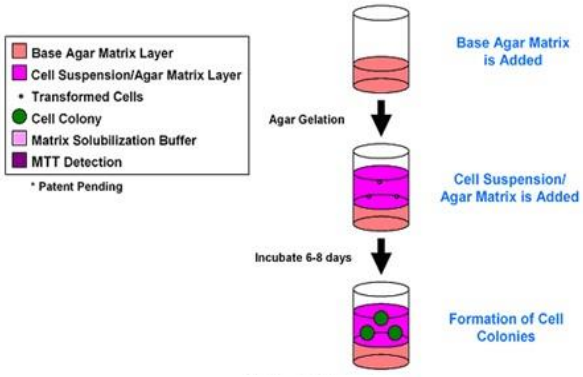

Figure 17. Soft agar colony formation processing. Obtained from Cambridge Bioscience.

3.3.4. Flow cytometry

Background

The main technique behind flow cytometry is the ability to measure fluorescence-based characteristics of single cells in suspension at a speed of up to 10,000 cells per second. A flow cytometer measures the emitted fluorescence of stained/fluorescent cells and has the ability to sort these cells on fluorescent dye/color, called fluorescence-activated cell sorting (FACS). Further, the scattering (forward and side scatter) of the laser when cells pass the light beam is measured. The side scatter correlates with the granulation in the cells, whereas the forward scatter indicates the size of cells. In this project, we applied flow cytometry to quantify transfection efficiency by measuring GFP-positive and -negative cells.

Method

Transfected cells were trypsinized, media was added to stop trypsinization reaction followed by centrifugation at 1200 rpm for 8 min. Supernatant was discarded and cell

pellets were washed with 1xPBS, centrifuged again and pellets were resuspended in a solution of $10x10^5$ cells/ml in 1xPBS. The cell suspension were transferred to FACS tubes (5 ml). A total of 30,000 cells was measured for GFP positivity by flow cytometry (FACS Calibur, Becton Dickinson, Palo Alto, CA). FACS data were analyzed using Flowing software (Cell Quest Pro).

3.3.5. 3D-sphere formation assay

Background

3D growth in cell culture assays is frequently used to identify the stemness capacity of the investigated cell types. Cells are cultured in ultra-low attachment plates with addition of growth factors to stimulate the undifferentiated state. 3D cultures are known to express (embryonal) reprogramming factors indicating stem-cell-like characteristics [142].

Method

To grow 3D-spheres, ultra-low attachment 24-well plates were used for cultivation. Adherent cells were detached by using StemPro Accutase cell dissociation reagent (Thermo Fisher Scientific, Waltham, MA, US) and seeded in a density similar to the respective clonogenic assay cell counts. Cells were seeded in Dulbecco's modified eagle's medium (Sigma) without serum but supplemented with growth factors (e.g. EGF and bFGF), B-27 supplement, N-2 supplement and L-glutamine (Thermo Fisher). After 72 h, 96 h, and 7 days, photomicrographs were taken using a Nikon Ti Eclipse fluorescent inverted microscope. Spheres were quantified calculating the sphere-area (μm^2) with ImageJ.

3.3.6. Transwell migration assay

Background

Migration is a normal characteristic of living cells during development and immune responses but also during cancer development and metastasis. To investigate the migratory potential of cells, transwell assays were performed. These assays are

based on the migration of cells from the inserted well into the lower well through small pores measuring 8 µm. Cells with high migratory potential are suspected to be more metastatic than less motile cells.

Method

To investigate the invasive and migratory potential of GBM cells and transfected sublines, wells of a 24-well plate were filled with 800 µl of growth medium with 10% FCS. Transparent PET membrane inserts with pores (8 µM, Falcon, Starlab, UK) were placed into each well. Cell suspension of 3 x 10^3 cells in serum-free growth medium per well (300 µl) was added into these inserts. After a settle and migration time of 24 to 48 h, inserts were taken out, cells on the lower side of the membrane were fixed in methanol and stained with crystal violet. The remaining cells in the lower plate were incubated for another 3-5 days followed by fixation and staining of the adherent and, thus, migrated cells. Pictures were taken with a Nikon D3200, integrated density was measured and clones were counted using ImageJ.

3.3.7. Wound-healing assay

Background

The wound-healing assay, also called “scratch” assay, is a simple assay applied to measure migratory capacity of cells *in vitro*. This assay is supposed to mimic the process of wound healing *in vivo*. To start the assay, a “wound” is scratched into a confluent cell monolayer. Afterwards the migration rate is analyzed microscopically at meaningful time intervals until the wound is healed. The speed, in which this entire process happens, is a measure to quantify the differences between cell lines.

In this study, the wound-healing assay was performed in combination with live-cell imaging to follow the closure process precisely and continuously over 48 h.

Method

Cells were seeded densely (1x10^5/well) into the wells of an 8-well glass chamber slide. After O/N settling time, scratches were made using a p10 micropipette

tip in each well from top to bottom and three times from left to right side. After scratching, wells were washed to remove loose cells and new medium was added. Live-cell microscopy immediately started to include a zero time point in the quantification of the assay. Three positions of the scratches per sample were recorded every 30 minutes for a total of 48 h, in brightfield as well as GFP wavelength, using the Nikon Eclipse Ti Livecell Inverted Widefield microscope and Visiview software. Scratches were analysed by quantification of the open area over the total length of 48 h using Tscratch software (CSE Lab, Zurich).

3.3.8. Transient transfection of FGFR4^{low} expressing GBM cell lines

Background

Gene transfection is the principle to manipulate gene expression of cells by transiently or stably introduce expression vector plasmids encoding open reading frames or regulatory RNA molecules of interest. The efficiency of gene transfection depends on the coping mechanism of the cells towards transfection reagents but also on the elements included in the vector. Vectors used in this thesis project were generated during this study as described in 2.6., consisting of retroviral plasmids coding for i) GFP (pQCXIP_EGFP (internally called A-174_GFP), Addgene, kindly provided by Prof. M. Grusch (Institute of Cancer Research, Medical University of Vienna)), ii) full length FGFR4_Gly_GFP and, iii) full length FGFR4_Arg_GFP c-terminal GFP fusion proteins.

Method

U251MG, HU-MI, BTL53, BTL90 and PU-MA cell lines were seeded in 6-well plates in concentrations of 1-3 x 10^5 cells per well (2 ml per well). After a 24 h recovery period, per each well 1 µg construct was mixed with 250 µl of serum-free growth medium. Additionally, 10 µl of Lipofectamine® 2000 (Thermo Fisher) was mixed with 240 µl serum-free growth medium. After mixing, 250 µl DNA mix was drop-wise added to the Lipofectamine® suspension followed by 20-30 min incubation time at RT. 500µl growth medium was removed from the wells and 500 µl serum-free DNA-Lipofectamine® mixture was added to the cells. Transfection reagent was incubated for 8 h, then removed, fresh medium was added, and cells were incubated for 24-48 h

at 37°C. Transfection efficiency was analyzed using the Nikon Ti Eclipse fluorescent inverted microscope and FACS measurements by assessing the percentage of GFP-positive cells. The vectors contained a puromycin-resistance cassette. Therefore, selection for transfected cells was possible. The cells were kept in cell culture under constant puromycin selection (1 µg/ml) and used for the described experiments.

3.3.9. Confocal laser scanning microscopy

Background

Confocal laser scanning microscopy (CLSM) is a more detailed form of microscopy compared to standard fluorescence (wide-field) microscopy. CLSM makes use of a pinhole system, generating high-resolution images. A CLS microscope includes two focal planes, which can be adjusted separately, resulting in removal of unfocused light to reduce background. Adjusting the focal planes increases image specificity and optimizes the maximum resolution of the microscope. By recording a set of focal planes, a z-stack is generated, providing high-resolution 3D images of the sample.

Method

Transfected (GFP, FGFR4_Gly_GFP and FGFR4_Arg_GFP) and the respective parental cell lines were seeded ($3x10^4$/well) in 8 well glass chamber slides with silicon wall (Ibidi) and left to adhere O/N. Cells were treated with 10µM ponatinib for 1 h, followed by removal of supernatant, washing with 1xPBS and fixation of the cells with fresh 4% paraformaldehyde (PFA) in PBS for 20 min. After fixation, wells were washed out with 1xPBS, cells were incubated with 4#, 6-diamidino-2-phenylindole (DAPI, 1.5 ug/ml, Thermo Fisher) and wheat germ agglutinin (WGA, 5 ug/ml, Thermo Fisher) for 20 min, washed with 1xPBS and covered with mounting medium (Vectashield) and a cover glass. Samples were directly analyzed by CLSM (Zeiss LSM700 confocal microscope) creating images in DAPI, Alexa488 and Alexa594 channels, with a 63x objective and immersion oil, using Zeiss Zen software.

3.4. Protein extraction and expression analysis

Background

Protein expression levels are an important source of information about biological mechanisms in cells of interest. By extracting proteins after cell lysis, the soluble proteins are separated from DNA and other non-protein cellular components. Protein samples loaded on a gel are separated based on size with help of electrophoresis followed by blotting on a membrane to make antibody detection possible.

Methods

3.4.1. Total protein isolation

Cells were seeded in T25 culture flasks at a density of $1x10^6$ cells per bottle and incubated for 24 h (up to 48 h) in a humidified atmosphere at 37°C containing 5% CO_2. Cells were scraped into growth medium on ice and centrifuged at 1200 rpm for 8 min at 4°C. After centrifugation, cells were washed with 1x PBS and lysed in 40 µl lysis buffer (500 µl lysis buffer contains: 5 µl PMSF (serine protease inhibitor, Roche), 12.5 µl Complete (protease inhibitor cocktail, Roche), 25 µl PhosSTOP (phosphatase inhibitor cocktail, Roche) for at least 45 min (cells were resuspended every 10 minutes during lysis process). Afterwards, samples were sonicated for 5 min in an ultrasound water-bath (Bandelin, Sonorex) and centrifuged at 14.000 rpm at 4°C for 15 min. The supernatant, containing the proteins, was collected and stored in aliquots at -80°C. Protein concentrations were determined with a plate reader (Tecan) by using the Micro BCA™ Protein Assay Reagent Kit (Pierce Biotechnology, Rockford, USA) according to manufacturer's instructions.

3.4.2. Nuclear & cytoplasmic cellular fractionation

Separation of nuclear and cytoplasmic protein fractions was carried out using the NE-PER Nuclear and Cytoplasmic Extraction Reagent kit (Thermo Fisher) following the manufacturer's recommendations. Fresh cell cultures were used for these extractions and protease inhibitors were added to the CERI and NER reagents (see recipe for lysis buffer) shortly before use. Isolates were stored at -80°C until use.

3.4.3. Membrane protein-enriched fractions

To isolate fractions enriched in cell membrane-associated proteins, cells were seeded in T150 cell culture flasks and grown up to a confluency of 70-90%. Cells were scratched into medium and centrifuged at 1.200 rpm for 8 min at 4°C in 50 ml centrifuge tubes. Pellets were resuspended in ice cold 1xPBS and centrifuged again. Supernatant was discarded and pellets resuspended in 1-1.5 ml Dounce buffer (500 µl buffer contains: 5 µl PMSF; 12.5 µl Complete; 25 µl PhosSTOP). After a 10 min incubation step on ice, suspensions were filled into a homogenisator and cells were mechanically lysed by destroying the cell walls with 35-40 slow beats per sample. Accuracy of homogenization process was tested by mixing cells with trypan blue, 90% or more blue cell nuclei (indicating disrupted membranes) were considered enough to continue the process. After addition of 50µl neutralization buffer, samples were centrifuged at 1.600 rpm for 5 min. The pellets containing DNA were discarded, whereas the supernatant with membrane and cytosolic protein fractions were transferred to special tubes (UZ Beckmann, Sorvall) for ultracentrifugation at 100.000 rpm for 1 h in an ultracentrifuge (Sorvall, RC M150, GX). After centrifugation, membrane protein-enriched pellets were dissolved by sonication for 3 min in 30-70 µl lysis buffer and stored at -80°C until use.

3.4.4. Sodium dodecyl sulfate polyacrylamide gel electrophoresis (SDS-PAGE)

Proteins were separated on polyacrylamide gels according to their molecular weight (kDa, figure 18). Per sample, 15 µg protein was diluted in lysis buffer and mixed with 4x loading buffer to a volume of 15-20 µl. SDS-PAGE was performed using a 12% separating gel (25-200 kDa) and a 4.5% stacking gel.

Table 4. SDS-PAGE ingredient summary of separating (12%) and stacking (4.%) gels, for 1 gel with 10-15 slots.

SDS-PAGE		
Ingredient	**Separating gel (12%)**	**Stacking gel (4.5%)**
ddH_2O	6.44 ml	3.11 ml
Tris pH 8.8	3.75 ml	-
Tris pH 6.8	-	1.25 ml
Acrylamide (40%)	4.60 ml	562 µl
10% SDS	100 µl	50 µl
TEMED	10 µl	5 µl
10% APS	50 µl	25 µl
Total volume	15 ml	5 ml

All separating gel ingredients were mixed, loaded onto a loading station (for polymerization (Bio Rad, Hercules, CA, US)) and gels were allowed to polymerize for at least 30 min. After polymerization of the separating gel, all stacking gel ingredients were mixed, poured into the loading station and, after placement of the sample comb (for 15 slots), allowed to polymerize for at least 30 min. After polymerization, gels were placed in an electrophoresis chamber (Bio Rad) filled with 1x Laemmli-Electrophoresis buffer. Protein samples were loaded into the slots in the gel and 5 µl Precision Plus Protein marker (Bio Rad) was used as molecular weight reference in a separate slot. Electrophoresis was started at a constant of 90 V for approximately 3-4 h, or until bands reached the end of the electrophoresis chamber.

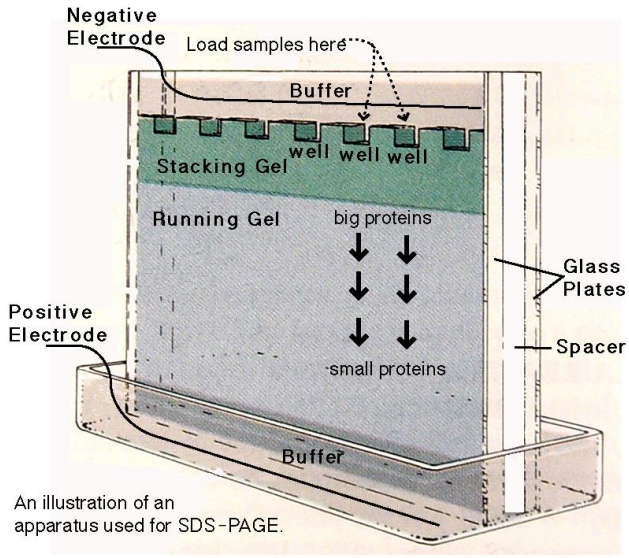

Figure 18. SDS-PAGE illustration indicating the loading gel in green and separation gel in grey. Adapted from creative-proteomics.com

3.4.5. Western blotting

Proteins were blotted onto PVDF membranes (1 membrane (6 cm x 9 cm) per gel) using a Trans-Blot Turbo (Bio Rad). The order of filters, gel and membrane was the following started from the bottom: i) wet filter paper soaked in Bjerrum-Blotting buffer containing methanol, ii) PVDF membrane activated with methanol, wetted in Bjerrum-Blotting buffer containing methanol, iii) SDS-PAGE gel wetted in Bjerrum-Blotting buffer containing SDS and iv) filter paper soaked in Bjerrum-Blotting buffer containing SDS. Blotting was performed for 30 min at constant 90 V.

After blotting, membranes were stained with Ponceau solution (0.1% ponceau in 5% acetic acid) to control equal protein loading followed by three washing steps (3 x 10 min) in 1x TBST. Before protein analysis, membranes were blocked in a milky solution (10 ml per membrane consisting of 1x TBST, 1% fat-free powdered milk, and 0.5 % BSA) for 1 h and washed again with 1x TBST.

3.4.6. Antibody incubation

Membranes were incubated overnight at 4°C with primary antibodies directed against FGFR4 C-16 (C-124, Santa Cruz, CA, US; 1:1000 dilution in 1x TBST and 3% BSA, rabbit polyclonal) and β-actin (BA3R, Thermo Fisher, 1:1000 dilution in 1x TBST and 3% BSA, mouse monoclonal). A primary antibody against β-actin was used as loading control. After incubation, membranes were washed three times 10 min with 1x TBST and incubated with the secondary antibody (anti-mouse-HRP or anti-rabbit-HRP (1:10.000), Pierce, IL, USA) for 1 h followed by three washing steps (10 min in 1x TBST). Proteins were visualized using the Luminol Reagent (Santa Cruz) and exposure to Amersham Hyperfilms™ ECL (GE Healthcare, Vienna, Austria, figure 19).

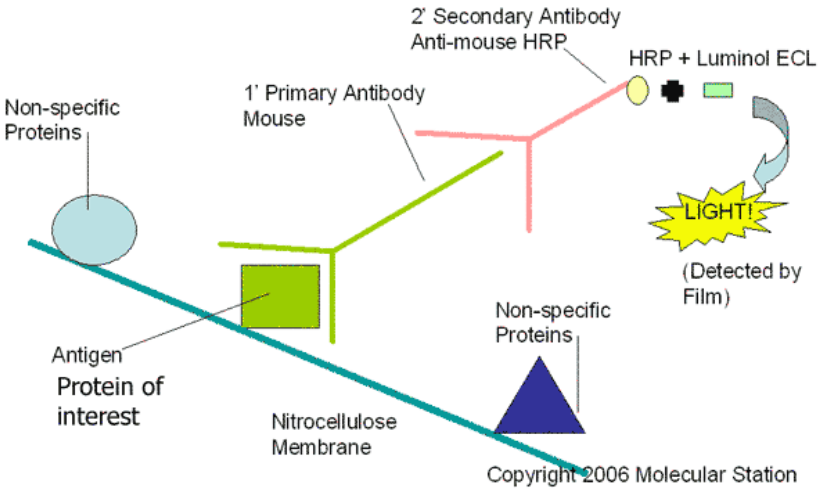

Figure 19. Detection mechanism for Western blot using indirect detection with antibody-HRP and luminol. Obtained from Woldpress.com

3.4.7. Buffers and other components needed for protein analysis

Lysis buffer	***Additions per 500µl lysis buffer***
50 mM Tris	25 µl Phospho-Stop (phosphatase inhib. Roche)
300 mM NaCl	12.5 µl Complete (protease inhib. Roche)
0.5% Triton X-100	5 µl phenylmethanesulphonylfluorice (PMSF, serine protease inhib., Roche)

Tris-HCl 1.5M pH8.8	**Tris-HCl 0.5M pH6.8**
18.2 g Tris	3 g Tris
Filled up to 100 ml with ddH_2O	Filled up to 50 ml with ddH_2O
pH adjusted to 8.8	pH adjusted to 6.8

10x TBS	**1x TBST**
120 g Tris	100 ml 10x TBS
90 g NaCl	Filled up to 1 L with ddH_2O
Filled up to 1 L with ddH_2O	1 ml Tween-20
pH adjusted to 7.6	

Dounce buffer	**Neutralization buffer**
0.12 g Tris-HCl (10mM, pH7.6)	0.12 g Tris-HCl (10mM, pH7.6)
0.01 g $MgCl_2$ (0.5 mM)	0.01 g $MgCl_2$ (0.5 mM)
Filled up to 100 ml ddH_2O	3.5 g NaCl (0.6 M)
	Filled up to 100 ml ddH_2O

10x Lämmli-buffer	**4x Sample loading buffer**
30 g Tris	4 ml 10% glycine
144 g Glycine	2 ml 2-mercaptoethanol
10 g SDS	0.92 g (9.2%) SDS
Filled up to 1 L with ddH_2O	2.5 ml 1M Tris-HCl (pH 6.8)
	Dissolved in ddH_2O up to 10 ml
	Aliquots stored at -20°C

Bjerrumbuffer + SDS	**Bjerrumbuffer + Methanol**
5.82 g Tris	5.82 g Tris
2.93 g Glycine	2.93 g Glycine
200 ml Methanol	0.375 g SDS
Filled up to 1 L with ddH_2O	Filled up to 1 L with ddH_2O

3.5. Classical polymerase chain reaction (PCR) and quantitative real-time PCR (qPCR)

Background

The polymerase chain reaction (PCR) technique implies the amplification of DNA fragments with help of target specific primers and a thermostable Taq polymerase enzyme. Three main steps in the PCR cycle are i) denaturation, during which the temperature is higher (92-98°C) than the melting point of the complementary target strands, resulting in separation of the strands followed by ii) primer binding onto target sequence at the free 3' OH at lower temperature (55-70°C), called annealing, and iii) elongation (72°C) of the sequence by a polymerase in 5' → 3' direction starting at a free 3'-OH group of the primer. The quantity of amplified DNA after performing a basic PCR can only be analyzed at the end of the total number of cycles (e.g. 35 cycles).

More precise quantification of amplification is performed by measuring the DNA or RNA amount in a solution in a real-time setting. This method is called quantitative real-time PCR (qPCR) and analyses genomic/plasmid DNA or RNA that has been reverse transcribed into cDNA. The latter reverse transcription (RT-) qPCR gives the opportunity to monitor the quantity of amplified cDNA by detection of fluorescent probes, such as Taqman probes or SYBR Green. RT-qPCR enables the interpretation of relative mRNA expression by measuring the intercalation of a reporter dye with the use of fluorescence and, in addition, indicates when samples reach a plateau during amplification, which is invisible in basic PCR.

Methods

3.5.1. Conventional PCR

A construct containing a full length FGFR4_Arg variant (#F36) was used to test primers, which were designed in Clone Manager software to target FGFR4 and produce a product that can be used for In-Fusion® HD Cloning, see 2.6. DNA-free water was used as negative loading control. Q5® high-fidelity DNA Taq polymerase (#E0555L, New England Biolabs, Ipswich, MA, US) was used for this PCR because the FGFR4 amplification product is ~3Kb. A master mix was made and, in total, the DNA sample was prepared five times to perform a gradient PCR reaching from 55-70°C to optimize the melting temperature fitting to the DNA fragment and primers. The PCR was performed on an iCycler (Biorad).

Primers (10 µM stocks)

Forw. IFU. 5'-GGCCTCGTACGCTTACCATGCGGCTGCTGCTG-3'

Rev. IFU. 5'-ATGGTGGCGATGGATTCTGTCTGCACCCCAGACC-3'

Master mix (1 sample)

DNA free ddH_2O	7.5 µl
5x Q5 Buffer	4 µl
dNTPs (1 mM)	2 µl
Fw. Primer (1µM)	2 µl
Rev. Primer (1µM)	2 µl
Q5 polymerase (50 U/ml)	0.5 µl
#F36 construct DNA (20 ng)	2 µl
Total volume	***20 µl***

dNTPs (per NTP 10mM)

10 µl dATP

10 µl dTTP

10 µl dCTP

10 µl dGTP

60 µl DNA free ddH_2O

Cycle conditions gradient basic PCR

Initial denaturation	98°C	30 sec	
Denaturation	98°C	10 sec	
Annealing	55-70°C	30 sec	35 cycles
Elongation	72°C	2 min	
Final elongation	72°C	3 min	

After running the basic PCR, a 0.8% (due to ~3 Kb fragment size) agarose gel in 1x TBE was made, samples were mixed with loading buffer (1:3, Thermo Fisher), loaded onto the gel and ran at 90V for 1-2 h in a 1x TBE buffer. After electrophoresis, gel was stained with an ethidium bromide mix (10 µl / 100 ml, Merck) for 10 minutes, washed 2x with ddH_2O and analyzed using a GelDoc 2000 (Biorad). Bands were visualized with UV-light and photographed using software provided with the GelDoc system.

3.5.2. RT-qPCR

Total RNA was isolated from all cell lines listed in table 2. Trizol® reagent (Life Technologies, Carlsbad, US) and chloroform were used to isolate total RNA. RNA samples were stored at -80°C until reverse transcription to complementary DNA (cDNA) was performed. Reverse transcription of 500 ng RNA to cDNA was carried out using the Revert Aid reverse transcriptase enzyme (Thermo Fisher) at 40°C. cDNA samples were stored at -20°C, in small 1:25 diluted aliquots to prevent repeated freeze-thaw cycles.

RT-qPCR with 1:25 dilutions of cDNA was performed using TaqMan *FGFR4* and TaqMan *ACTB* probes (Thermo Fisher) containing a FAM fluorophore. Samples were pipetted in a MicroAmp® Fast Optical 96-Well Reaction Plate (Thermo Fisher, Applied Biosystems) and qPCR was performed using the ABI 7500 real time PCR-machine and software (Applied Biosystems). *ACTB* served as housekeeping gene, to normalize *FGFR4* cycle thresholds (ΔCt). Relative expression levels of each sample were compared to a positive control (Hep3B), depicted in ΔΔCt values.

Master mix (1 sample)

cDNA (1:25)	5 µl
TaqMan probe	0.5 µl
2x TaqMan qPCR master mix	5 µl
Total volume	***10.5 µl***

3.5.3. Restriction fragment length polymorphism (RFLP)

Restriction fragment length polymorphism was performed to test the G388R SNP status of the generated FGFR4 constructs (#F36 & #F37 kindly provided by Prof. M. Grusch). Primers target a part of the transmembrane domain sequence of FGFR4 (the critical part of exon 9 including codon 388) resulting in a PCR product of ~168 bp (figure 20).

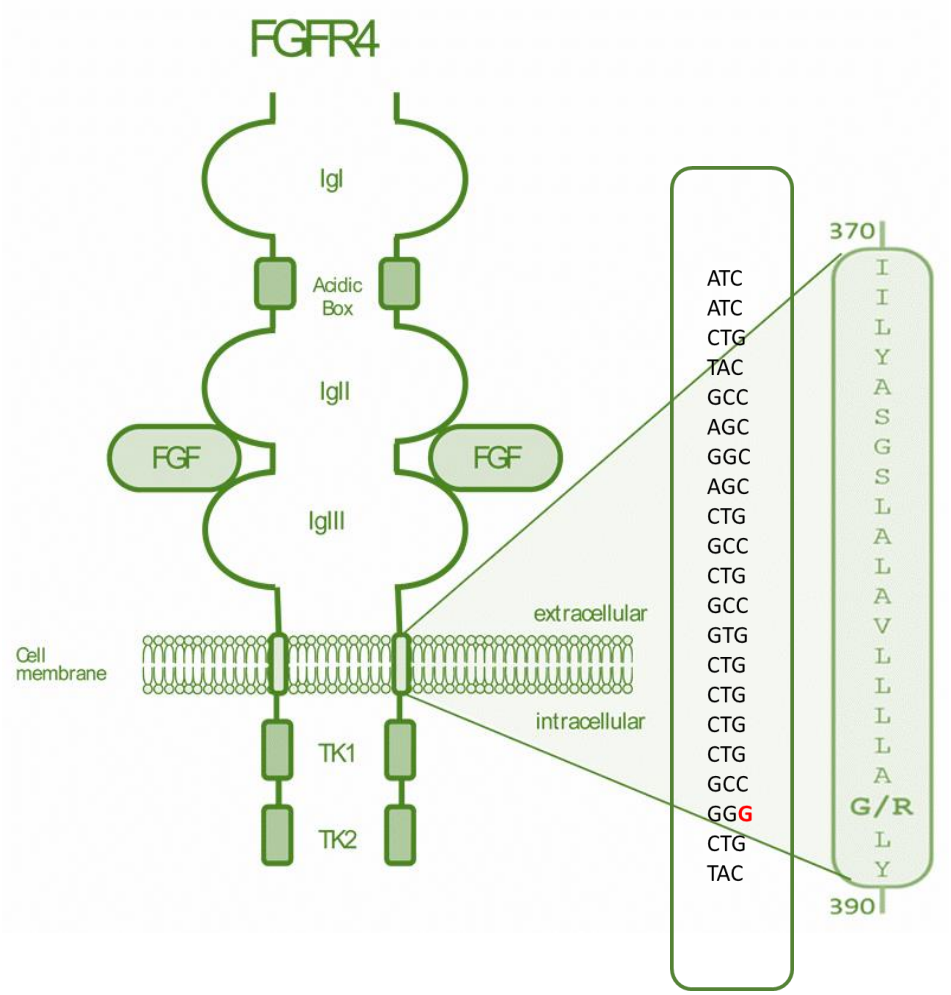

Figure 20. FGFR4 and a schematic indication of the localization of the widely known G388A polymorphism. Adapted from *Heinzle et. al.* [111].

Primers

Forw. RFLP 5'-GACCGCAGCAGCGCCCGAGGCCAGGTATACG-3'

Rev. RFLP 5'-AGAGGGAAGCGGGAGAGCTTCTGCACAGTGG-3'

Two samples carrying either a Gly388 or Arg388 polymorphism were additionally added to the set of samples to serve as positive restriction controls (RFLP) and, in addition, one ß-actin sample was used, serving as positive PCR control.

Master mix (1 sample)

DNA (20 ng)	2 µl
Fw. Primer (1µM)	2.5 µl
Rev. Primer (1µM)	2.5 µl
2x PCR master mix	12.5 µl
DNA free ddH_2O	5.5 µl
Total volume	***25 µl***

PCR amplified products were treated with the restriction enzyme BstNI (isoschizomere of MvaI, Thermo Fisher) at 60°C for 1 h.

Restriction mix (1 sample)

PCR product	10 µl
Enzyme BstNI	0.5 µl
10x NEB Buffer #2	2 µl
BSA (0.2 mg/ml)	0.2 µl
DNA free ddH_2O	7.3 µl
Total volume	***20 µl***

BstNI cuts the sequence “CCWGG” where W stands for an A or T. The 168 bp fragment harbors two restriction sites for BstNI in both SNP variants, at base position 22 and 59. Furthermore, the Gly388 variant exhibits the sequence CCGGG, whereas the Arg388 variant has CCAGG. Thus, the Arg388 sequence yields an additional restriction site at base position 88. In summary, restriction with BstNI resulted in three fragments for the Gly388 variant (22, 37 and 109 bp) and four fragments of the Arg388 variant (22, 37, 29 and 80 bp).

Restricted samples, and in addition some undigested samples as negative controls, were mixed with loading dye (1:3), loaded on a 15% polyacrylamide gel or 2% agarose gel and run for 1 h at 90V. Gel was stained with ethidium bromide and washed with ddH_2O for 10 minutes. Bands were visualized with UV-light and photographed with the software provided with the GelDoc system (Biorad).

3.6. Molecular cloning

Background

During this project, we used the In Fusion® HD Cloning Kit (Takara Bio Inc., MV, CA, US). This kit is supposed to be used for directional cloning of single or multiple small or large fragments. PCR fragments of the target gene are generated containing a 15 bp overhang complementary to the sequences flanking the restriction site of a target-vector backbone. In-fusion cloning makes specific cloning, without addition of extra bases between targets, possible. Figure 21 serves as graphical abstract indicating the In-Fusion cloning method.

The FGFR4 full-length gene, harboring either the Gly388 or Arg388 polymorphism, was cloned into the pQCXIP-EGFP expression vector, generating a FGFR4_GFP fusion gene containing an in-frame c-terminal GFP tag.

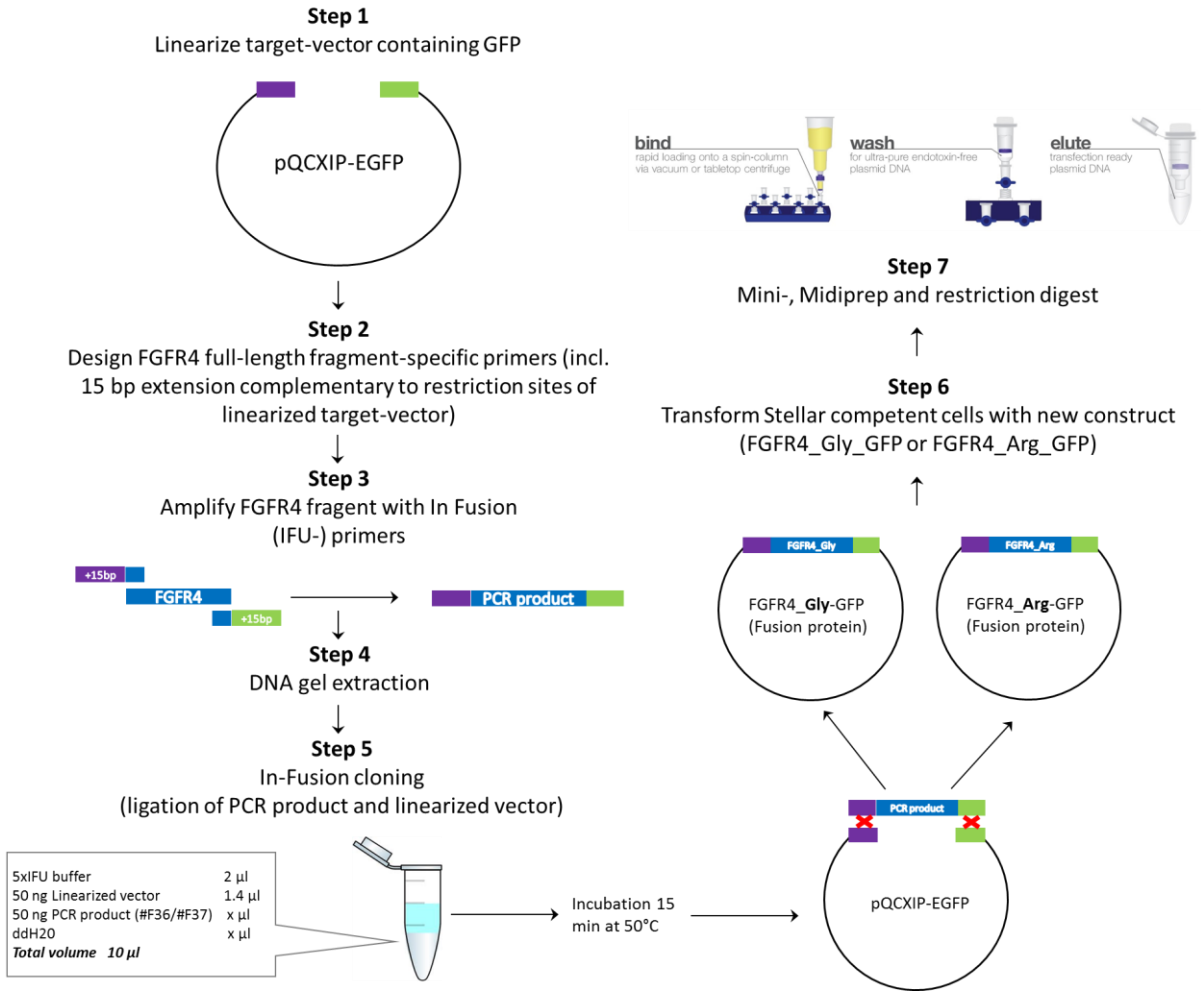

Figure 21. In-Fusion cloning procedure. Adapted from In-Fusion HD cloning, Takara Inc. and Zymoresearch.

3.6.1. Target-vector selection

Target-vector pQCXIP-EGFP was kindly provided by Prof. M. Grusch. This construct was selected because it contains one single BamHI (New England Biolabs) restriction site close to the multiple cloning site (MCS), upstream of the *EGFP* gene, as indicated in figure 22. Furthermore, this vector contained an ampicillin bacterial resistance gene and a puromycin mammalian selection marker downstream of the cloning site after an internal ribosomal entry site (IRES). Additionally, it contained a CMV promotor in front of the BamHI restriction site, and a SV origin of replication (ori).

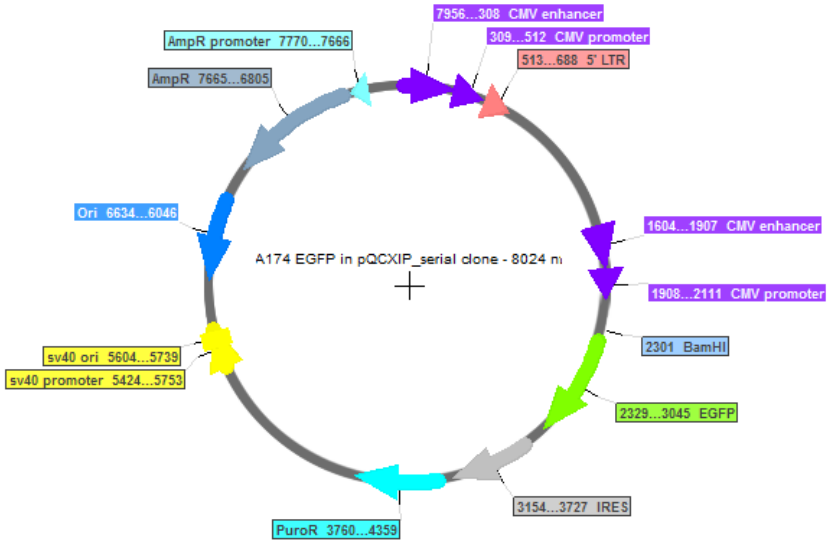

Figure 22. Plasmid map of pQCXIP-EGFP containing a single BamH1 restriction site before the EGFP sequence.

3.6.2. In-Fusion® primer design

In-Fusion® primers were designed with help of Prof. M. Grusch using Clone Manager software (Scientific & Educational Software, Denver, CO, US). The 5' ends of both the forward- and reverse primer contained 15 bp extensions, designed to be complementary to the sequence flanking the target-GFP vector at the restriction site for BamHI. The other 18 bp of the forward primer were complementary to the sequence starting at the start codon whereas the 18 bp of the reverse primer were complementary to the sequence starting upstream the 3 bases coding for the "stop". These primers create a PCR product containing full-length FGFR4 lacking the "stop" codon and flanking the insertion site of the target-vector.

3.6.3. Amplification of FGFR4 full-length with Q5 polymerase

Full-length FGFR4 containing either the Gly388 or Arg388 SNP variant was amplified by basic PCR with the Q5 polymerase using construct #F36 (FGFR4_Arg) and #F37 (FGFR4_Gly) according to section 2.5.1. and PCR fragments were separated by agarose gel electrophoresis. Bands were visualized using UV light and cut out with a scalpel. DNA clean-up was performed using the Monarch DNA gel extraction kit (New England Biolabs) according to the manufacturer's instructions.

3.6.4. In-Fusion® cloning

The In-Fusion® cloning was performed by mixing 50 ng of purified PCR product and 50 ng of the linearized vector with 5x In-Fusion enzyme buffer in a total volume of 10 µl. This ligation mixture was incubated at 50°C for 15 minutes, followed by a stop of the reaction on ice. Successful cloning resulted in new constructs with a size of ~10Kb.

3.6.5. Heat-shock induced transformation of Stellar competent cells

Stellar competent cells were transformed with the new constructs harboring either a FGFR4_Gly_GFP or FGFR4_Arg_GFP fused open reading frame. Competent cells were thawed on ice, slowly, and added in 14 ml round bottom tubes in a volume of 50 µl per transformation. To each of the tubes, 2.5 µl of the newly ligated vector was added. Cells were placed on ice for 30 minutes, followed by heat shock at 42°C for 45 sec and 1-2 minutes on ice. SOC growth medium was added to a final volume of 500 µl and cells were incubated for 1 h at 37°C whilst shaking at 200 rpm. Cells were diluted 1:10 in SOC medium (to generate a concentration of approximately 1 x 10^8 cfu/µg) and plated on LB plates containing ampicillin (50 µg/ml). The remaining cells were additionally centrifuged, resuspended in 100 µl SOC medium and plated on LB plates containing ampicillin (50 µg/ml). Cells were incubated O/N at 37°C.

To amplify transformed colonies, per cloned construct (FGFR4_Gly_GFP or FGFR4_Arg_GFP), ten colonies were picked and grown up O/N at 37°C in liquid LB medium containing ampicillin (50 µg/ml).

3.6.6. Mini- and Midiprep of transformed Stellar competent cell colonies and restriction digest of isolated plasmid DNA

For isolation of plasmid DNA from transformed bacterial cultures, PureYield™ plasmid mini- and midiprep systems (Promega) were used according to the manufacturer's recommendations. Elution was performed using the vacuum technique and plasmid DNA was washed off the membrane with 30 µl of nuclease free ddH_2O for miniprep samples or 500 µl of nuclease free ddH_2O for midiprep samples.

To verify cloning accuracy, mini- and midiprep isolated plasmid DNA samples were digested with restriction enzyme NotI (Fast digest, Thermo Fisher). The recognition site for NotI is 5'-GCGGCCGC-3' and cuts between the first C and GG resulting in GC GGCCGC.

With focus on the plasmid DNA, NotI was incubated with either the mini- or midiprep plasmid DNA samples and fast digest buffer (New England Biolabs) for 20 minutes at 37°C. NotI cut upstream and downstream of the inserted FGFR4_GFP sequence which resulted in fragments of 3184 bp and 7175 bp, indicating accurate cloning. Empty plasmids showed fragments of 772 bp (GFP-only) and 7175 bp. After incubation, digested and the respective undigested samples were loaded onto a 0.8% agarose gel and run for 30 minutes at constant 90 V. Bands were visualized with UV light on a GelDoc and documented with provided GelDoc software (Biorad).

Glycerol stocks were prepared of transformed bacterial cultures by resuspension of cell pellets into LB medium with 15% glycerol. Stocks were stored at -80°C until further use.

3.6.7. Sequencing of isolated FGFR4_Gly/Arg_GFP constructs

The FGFR4_Gly_GFP and FGFR4_Arg_GFP constructs were sequenced using primers directed to either i) the CMV promoter located upstream of the FGFR4 insertion site or ii) the GFP sequence located downstream of the inserted FGFR4. Primer sequences were the following:

Forw. CMV: 5'- GCAGAGCTCGTTTAGTGAACC -3'

Rev. GFP: 5'- CTGAACTTGTGGCCGTTTAC -3'

Rev. EGFP: 5'- AAGTCGTGCTGCTTCATGTG -3'

A basic PCR was performed with the selected primers to test if these were suitable for sequencing before sending the samples to Eurofins (Laboratory testing services, Vienna, AT). PCR samples were loaded onto a 0.8% agarose gel, run for 30 min at a constant 90V and bands were visualized with UV light on a GelDoc (Biorad)

Samples for Sanger sequencing were prepared using 100 ng/µl plasmid DNA and 10 µM single primers filled up to a total volume of 15 µl with DNA-free ddH_2O in 1.5 ml DNA free “safe lock” Eppendorf tubes. These tubes were sent to Eurofins at RT for sequencing. Results were analyzed by blasting the obtained sequences to the construct and FGFR4 full-length (GeneBank) sequences.

3.7. *In vivo* tumor formation in severe combined immunodeficient (SCID)-mice

Background

All procedures involving animals and their care were approved by the Ethic Review Board of the Medical University of Vienna and performed following (Austrian) FELASA guidelines [48]. Normal food and water was provided *ad libitum* for the animals during experiments.

Figure 23. SCID mouse. Obtained from Taconic Biosciences.

Method

3.7.1. Anticancer activity in GBM xenografts

The tumorigenicity of GBM cell lines was tested in 8-week old female severe combined immunodeficient (SCID) mice. GBM xenografts were obtained by subcutaneous (s.c.) injection of 1 x 10^6 U251MG (including indicated transfected sublines), HU-MI and SI-WA cells in 50µl (serum-free medium supplemented with 25% matrigel™ membrane matrix, Corning, Thermo Fisher) into the right flank of the mice. Body-weight and s.c. tumor growth was measured every second day using a micro-caliper. Animals were sacrificed by cervical dislocation when humane end-points (2.7.2.) were reached (or 6 months after cell injection without tumor formation). Upon death, mice were dissected, organs (e.g. lung, liver, kidney, brain) and tumor(s) were collected and processed for histological evaluation.

3.7.2. Humane end-points

Animals were sacrificed when they showed: i) a weight loss of ≥ 15% in a short time-frame or more than 20% since the beginning of the experiment, ii) eating disorders (e.g. strong reduction in food uptake), iii) changed/abnormal general appearances (e.g. self-harming and irregular sleeping pattern), iv) changed/abnormal social interaction (e.g. unwilling to play), v) changed/abnormal exploratory behavior (e.g. no nesting, aggressive digging, climbing and not being able to stand on two legs) and vi) abnormal breathing frequency.

3.8. Statistical analysis

All MTT data are presented as means ± standard deviation (S.D.) of at least three ‘identical’ experiments, each performed in triplicates. *In vivo* experiments consisted of n = 4 per group.

Statistical significance between treatments and IC_{50} values were analyzed in GraphPad Prism 5.0 using as appropriate student’s t-test, one- or two-way ANOVA or column statistics against a hypothetical value “1.0”. In all cases, $p \leq 0.05$ was considered statistically significant (labeled as *), p-values ranging from 0.01 to 0.001 as very significant (**) and those below 0.001 as highly significant (***).

4. Results

Up- or downregulation of FGFR4 expression is known to play an important role during the process of tumorigenesis in many cancers types (e.g. colorectal, prostate, breast, bladder and lung cancer, multiple myeloma and rhabdomyosarcoma) [143-145]. The Gly388Arg polymorphism is frequently described and suggested to be related to a more aggressive tumor phenotype and increased migratory potential [146, 147]. Detailed roles of FGFR4 and the differences between the Gly388 and Arg388 variant in GBM/GS are still poorly understood.

Previous experiments indicated decreased proliferation rates and impaired 3D-growth capacities upon FGFR4 blockade. To assess the role of FGFR4 in GBM, we analyzed endogenous FGFR4 expression on mRNA as well as on protein levels in a subset of primary GBM and GS primo-cell cultures. Further, FGFR4 low-expressing cell lines were transfected with fused, wild-type, full length FGFR4_GFP expression plasmids harboring either the Gly388 or Arg388 variant. Proliferation, migratory potential as well as the effects of pan-FGFR inhibitors on 2D- and 3D-growth were analyzed.

4.1. Endogenous FGFR4 in GBM samples

4.1.1. Endogenous mRNA and protein expression of FGFR4 in primary adult GBM and GS primo-cell cultures

Previous studies performed by Lötsch *et al*. (unpublished) revealed variable mRNA expression of FGFR4 in a subset of patient-derived primary GBM primo-cell cultures and tumor tissue samples as compared to non-malignant epileptic brain foci (tissue samples) (figure 24). Several samples reached expression levels similar to the FGFR4-overexpressing hepatocellular carcinoma cell line Hep3B.

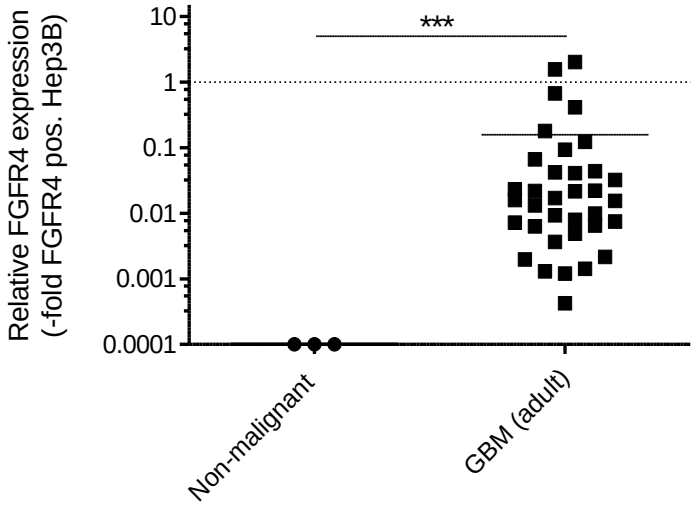

Figure 24. Relative FGFR4 mRNA expression in primary GBM primo-cell cultures and tumor tissue samples. GBM expression is normalized to the high FGFR4-overexpressing cell line Hep3B (set as 1) and compared to non-malignant epileptic foci tissue samples. Significance was calculated using student's t-test (*** = p <0.001).

In silico analysis of a GBM whole genome mRNA expression data set, obtained from The Cancer Genome Atlas (TCGA), was performed to analyze the 4000 most variably expressed genes in GBM correlated to FGFR4 overexpression. Unsupervised clustering of this dataset revealed a distinct cluster of $FGFR4^{high}$ GBM samples (figure 25). These $FGFR4^{high}$ GBM samples mainly belong to mesenchymal and neural subtypes [148]. In addition, a subgroup was found to represent GS.

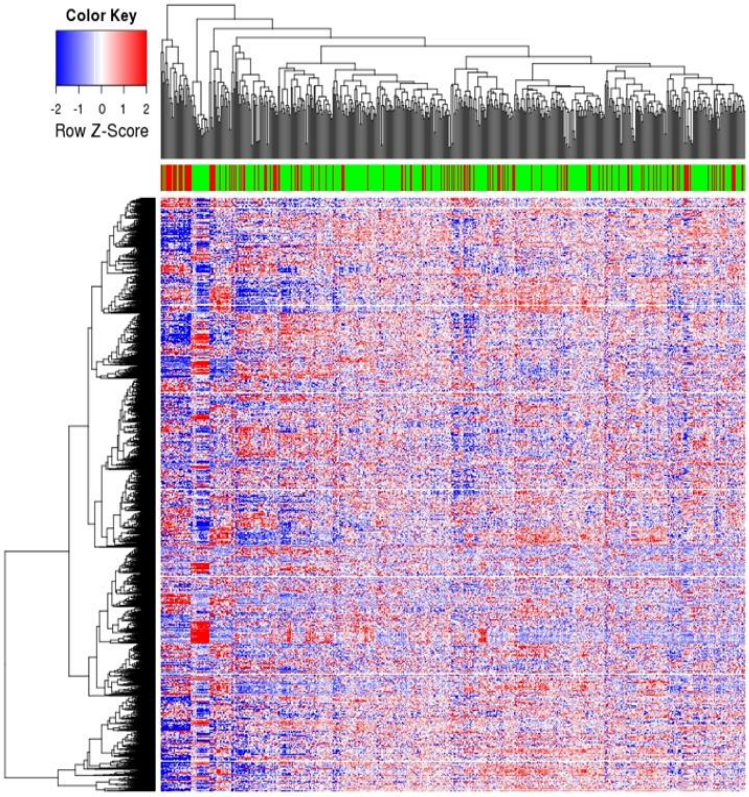

Figure 25. Heat map depicting FGFR4 expression correlated to the 4000 most variably expressed genes in adult GBM. Samples are clustered in the upper panel, left panel indicates the subset of 4000 most variably expressed genes in GBM. Red bars indicate $FGFR^{high}$ and green bars indicate $FGFR4^{low}$ samples.

A set of 11 primary GBM cell lines (primo- and immortalized cultures) was selected to investigate the endogenous protein expression levels of FGFR4, while Hep3B cells served as positive control. The cell lines SI-WA, BTL1376 and BTL1377 displayed significant FGFR4 protein expression, although, to a distinctly lower extend than Hep3B (0.25-fold, 0.56-fold and 0.19-fold Hep3B, respectively) (figure 26A). Accordingly, relative FGFR4 mRNA expression (again normalized to Hep3B) reflected low FGFR4 gene expression in U251MG and HU-MI as well as an elevated one in SI-WA and BTL1376 cells. These data suggest regulation of FGFR4 expression mainly on the transcriptional level (figure 26B). Interestingly, despite the fact that HU-MI cells showed comparable mRNA expression levels to SI-WA, no FGFR4 expression was detectable in HU-MI but readily in SI-WA protein samples.

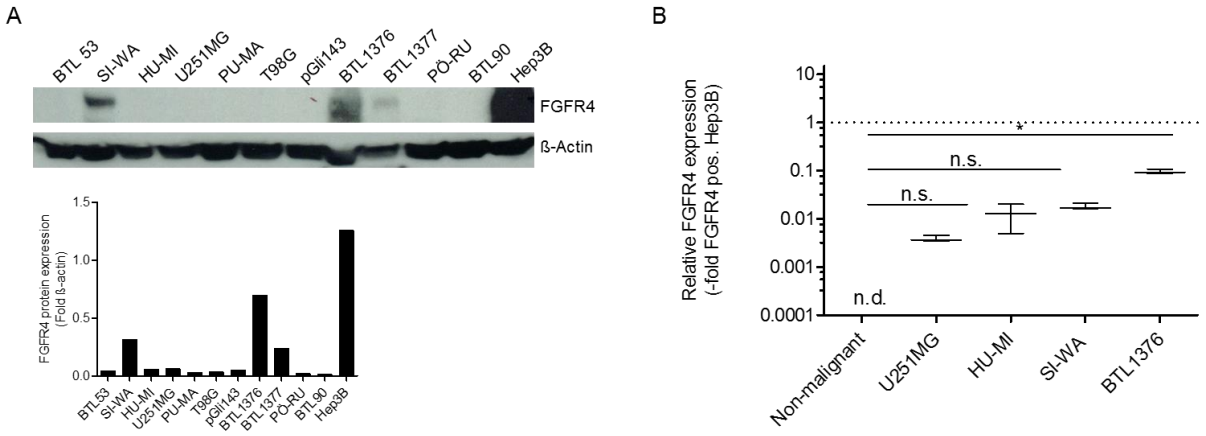

Figure 26. Endogenous FGFR4 expression levels in primary GBM cell lines. A) FGFR4 protein expression analysed in a panel of GBM primo-cell cultures and immortalized cell lines in relation to the highly positive FGFR4 expressing cell line Hep3B, detected by western blot (upper panel) and quantified, ß-actin served as loading control (lower panel). B) Relative FGFR4 mRNA expression levels in the commercially available cell line U251MG and primo-cultures HU-MI, SI-WA and BTL1376. Data are given normalized to Hep3B and compared to non-malignant epileptic foci tissue samples, significance calculated by one-way ANOVA, *p <0.05.

Investigation of the *FGFR4* gene locus (by array comparative genome hybridization (aCGH) and conventional CGH on metaphase chromosomes) demonstrated that overexpression of FGFR4 in BTL1376 (and Hep3B, data not shown) is not based on gene amplification, indicated by lack of copy number gains on chromosome 5q35.1 (figure 27). On the contrary, SI-WA cells harbored a gain at both (sub)telomeric regions of chromosome 5, indicating DNA amplification of chromosomal regions comprising the *FGFR4* locus. However, in this case, gene dose could not be

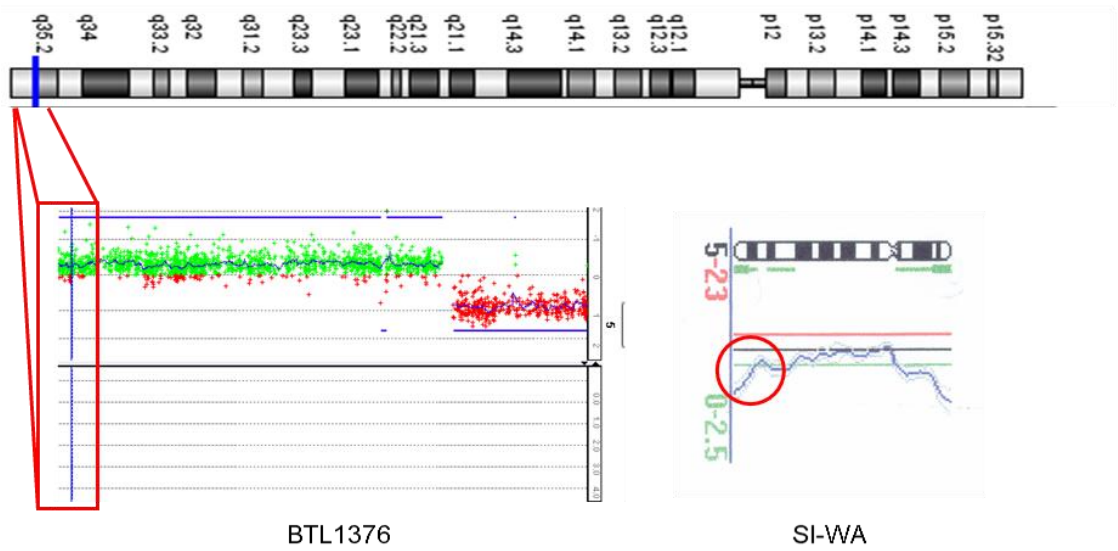

Figure 27. Analysis of *FGFR4* copy number alterations in BTL1376 and SI-WA by CGH. Relative gene-dose alterations of BTL1376 and SI-WA were analyzed by aCGH and conventional CGH using normal diploid chromosomal DNA as reference. Chromosome 5 of BTL1376 (left panel) and SI-WA (right panel) are shown. The *FGFR4* locus is indicated by the blue line in the red rectangle (left) and circle (right).

determined exactly due to the low resolution of conventional CGH. The respective array CGH experiment is ongoing.

4.1.2. The effects of FGFR inhibition on FGFR4^{high} and FGFR4^{low} expressing cell lines

To investigate the dependency of selected GBM cell models on FGFR4 and to observe the effect of pharmacological FGFR inhibition on the FGFR4^{low} and FGFR4^{high} expressing cell lines, the pan-FGFR inhibitors ponatinib and nintedanib were used. To this end, viability assays after 72 h drug exposure were performed. The obtained results indicated hypersensitivity towards ponatinib of the FGFR4^{high} expressing cell lines BTL1376 and Hep3B (IC_{50}: 0.35 µM and 0.48 µM, respectively) in contrast to the FGFR4^{low} expressing cell lines U251MG and HU-MI (IC_{50}: 4.75 µM and 8.38 µM, respectively, figure 28). Upon nintedanib treatment, BTL1376 exhibited the strongest sensitivity towards the TKI, with an IC_{50} below 5 µM. On the contrary, U251MG and HU-MI were non-responsive after treatment with up to 10 µM. The same sensitivity tends, but generally at lower concentrations, were observed in ponatinib treated cells. Overall, ponatinib showed higher anticancer activity in all cell lines tested (table 5). Therefore, this TKI was selected for further experiments.

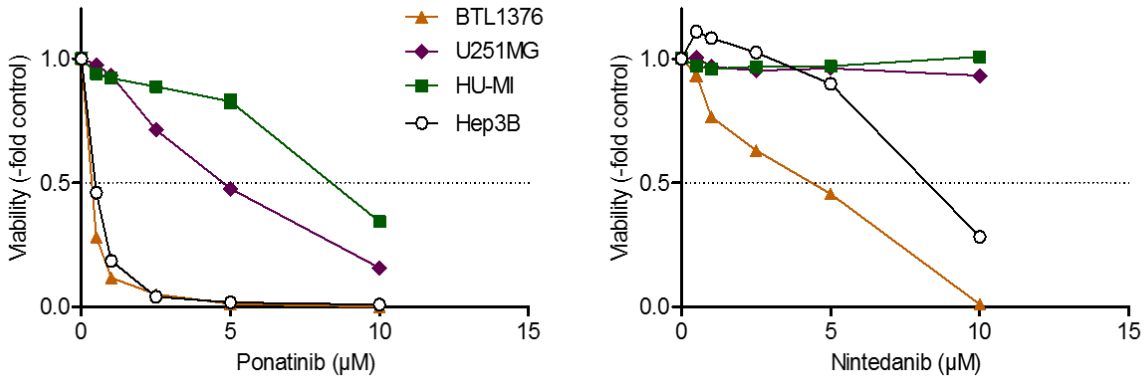

Figure 28. Effect of FGFR inhibition by pan-FGFR inhibitors ponatinib and nintedanib in GBM. Indicated cell lines were exposed to increasing concentrations of ponatinib and nintedanib for 72 h. Viability was determined using MTT assay. The FGFR4 overexpressing cell line Hep3B served as positive control. Each data point represents the mean ± SD of three values of a representative experiment, performed in triplicates.

Table 5. IC_{50} values indicating cytotoxicity of the pan-FGFR inhibitors ponatinib and nintedanib on primary GBM cell lines and the FGFR4 positive control Hep3B. (SD, standard deviation)

	Ponatinib (µM)		Nintedanib (µM)	
Cell line	**Mean IC_{50}**	**± SD**	**Mean IC_{50}**	**± SD**
U251MG	4.75	± 0.02	>10	
HU-MI	8.38	± 0.04	>10	
BTL1376	0.35	± 0.04	4.36	± 0.04
SI-WA	2.81	± 0.02	>10	
BTL1377	0.38	± 0.02	3.66	± 0.02
PÖ-RU	0.99	± 0.04	>10	
PU-MA	4.50	± 0.05	8.54	± 0.02
BTL53	2.36	± 0.05	>10	
BTL90	1.78	± 0.02	6.94	± 0.03
pGli143	2.20	± 0.02	7.35	± 0.04
T98G	4.27	± 0.03	>10	
Hep3B	0.48	± 0.03	8.24	± 0.02

To investigate the dependency on FGFR with respect to 2D- and 3D-growth, clone- and neurosphere-formation capacities, the three selected GBM cell lines (HU-MI, U251MG and BTL1376) were tested under treatment with ponatinib (7 day drug exposure) at indicated concentrations. The $FGFR4^{high}$ cell line BTL1376 showed significantly impaired colony forming capacities after ponatinib treatment compared to the control samples, already at nanomolar concentrations (500 nM, $p < 0.001$, figure 29). Additionally, clone-forming capacity was significantly reduced in the $FGFR4^{low}$ cell lines HU-MI and U251MG, albeit to a lesser extent. These findings are in line with the cell viability data indicated in figure 28. Furthermore, significant differences were observed between the reduction of clone-formation by ponatinib in $FGFR4^{high}$ versus $FGFR4^{low}$ expressing cell lines ($p < 0.001$).

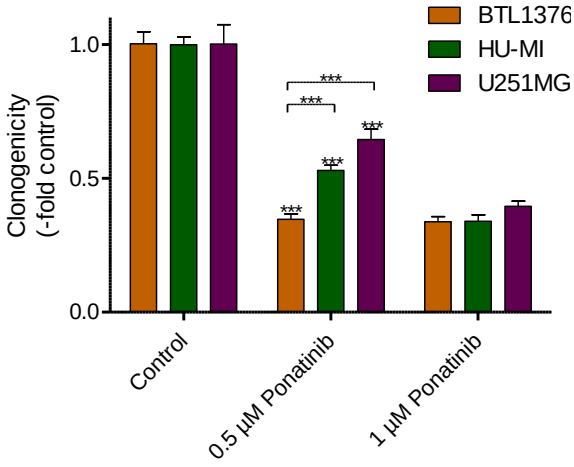

Figure 29. Reduced clone-forming capacity of $FGFR4^{high}$ and $FGFR4^{low}$ expressing GBM cell lines BTL1376, HU-MI and U251MG upon ponatinib treatment. Ability of single cells to form clones in the presence of indicated ponatinib concentrations was determined by clonogenicity assays. All cell models were seeded in a density of 2000 cells per well and exposed to ponatinib for 7 days. Clonogenicity was determined on crystal violet-stained, fixed cells photometrically. Values of treated samples (of at least three experiments performed in duplicates) are normalized to their respective control, significant difference is calculated with two-way ANOVA and indicated as *** $p < 0.001$ (asterisks on top of bars indicate the significant differences between treated versus control samples, those above lines show significant differences between $FGFR4^{high}$ and $FGFR4^{low}$ expressing cell lines, error bars indicate mean ± SD).

To investigate the effect of ponatinib on 3D-growth, neurospheres were grown from single cells, using NB^+ medium supplemented with growth factors to induce stem cell-like differentiation of the GBM cell lines. Drug exposure for 7 days started 96 h after seeding to measure the inhibitory effects on spheres and not on single cells. FGFR inhibition on 3D-cultures showed comparable effects as previously observed in clone formation- and viability assays. BTL1376 was sensitive to FGFR inhibition by ponatinib whereas the sphere density and diameters remained widely unchanged in HU-MI and U251MG treated spheroids (figure 30). Interestingly, 3D-growth capacity in BTL1376 was affected only at a higher drug concentration, 2.5 µM, in contrast to the effect in cell viability and clone formation (0.35 µM and 0.5 µM, respectively). This indicates that high FGFR4 expression levels might play an important role in stemness of GBM cells.

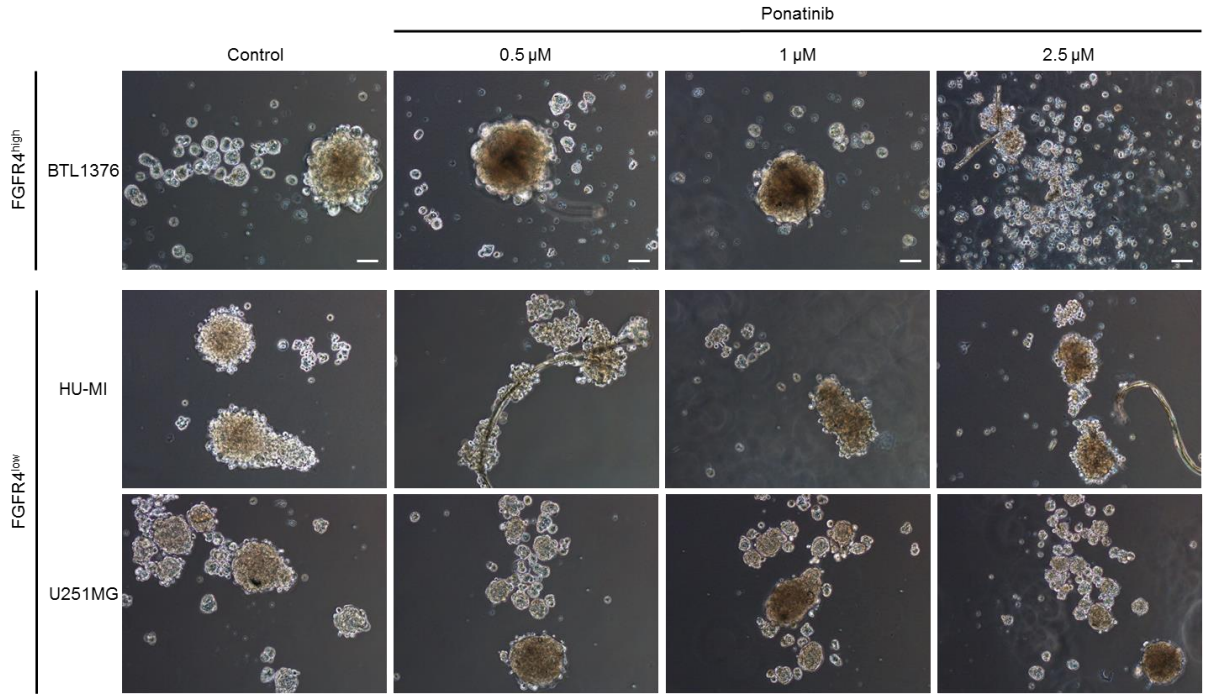

Figure 30. Impaired neurosphere formation after ponatinib treatment in $FGFR4^{high}$ expressing cell line BTL1376. Neurosphere formation of suspended GBM cells was induced by culturing in NB+ medium for 96 h. Subsequently, spheres were exposed to ponatinib for 7 days at indicated concentrations. Photomicrographs show neurospheres with indicated concentrations of ponatinib, bars are equal to 100 µm. Photomicrographs were taken at identical time points (after 7-day drug exposure).

4.2. The impact of ectopic overexpression of a dominant-negative FGFR4 variant on GBM cell lines and their proliferative behavior

In order to gain more insights into the dependency of GBM malignancy on FGFR in general and FGFR4 in particular, FGFR4 signaling was blocked in U251MG and MGC cells by introducing an expression vector harboring dominant-negative FGFR4 (dnFGFR4). Tumorigenic capacity of the dnFGFR4 transfected cell lines *in vitro* as well as *in vivo* has been analyzed prior to this project, by D. Lötsch and S. Allerstorfer.

4.2.1. FGFR4 blockade in U251MG and MGC cells leads to lower proliferation and impaired clonogenicity

U251MG and MGC cells were transfected with dnFGFR4 constructs and tested for their proliferative and clonogenic characteristics in relation to GFP-transfected control cells. Both, U251MG and MGC, exhibited significantly lower proliferation rates (0.8- and 0.5-fold) upon blockage of FGFR4 as compared to their respective GFP-controls (figure 31A). Additionally, introduction of a dnFGFR4 construct resulted in impaired clonogenicity of U251MG cells in relation to the untransfected parental as well as the GFP control cell line ($p < 0.01$, figure 31B).

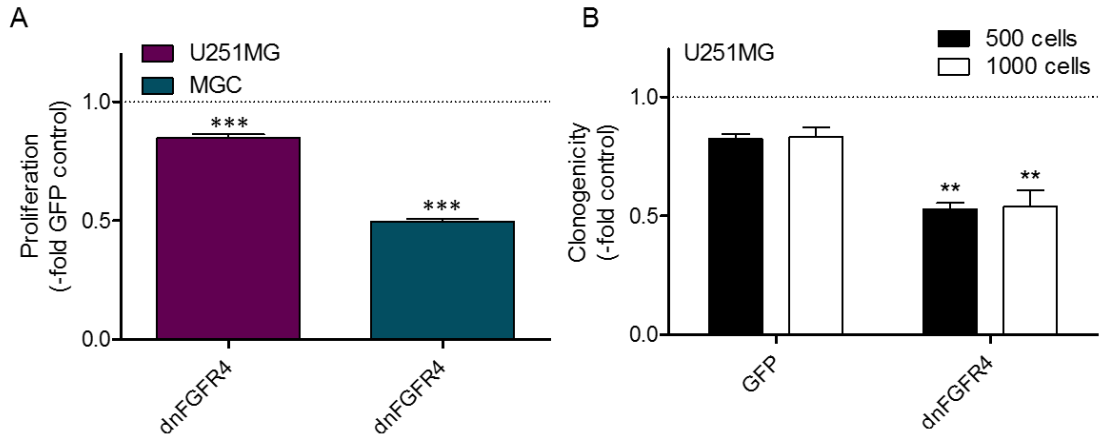

Figure 31. Impaired proliferation and clone forming capacity of U251MG and MGC cells after FGFR4 blockade. A) dnFGFR4 transfected cells were seeded at a density of $1x10^5$. After 72 h, cells were trypsinized and counted. Values are given relative to the GFP-control (set as 1). B) The potential of transfected cells, seeded at low density, to form multicellular clones was determined by clonogenicity assay. Indicated cell numbers were seeded and incubated for 7 days. Clonogenic potential was determined by photometric quantification of fixed, crystal violet-stained cells. Values are given relative to untransfected control (set as 1). Bars indicate triplicate values of a representative experiment, performed at least three times (mean ± SD). Statistical differences (student's t-test) are marked with **p <0.01, ***p <0.001.

4.2.2. Impaired 3D-growth capacity in vitro and subcutaneous tumor formation in vivo upon transfection of GBM cells with dnFGFR4

Transfection of U251MG cells with dnFGFR4 vector negatively affected proliferation and clonogenicity. Further, we observed impaired 3D-growth upon FGFR4 blockade in U251MG cells as compared to the respective GFP-control *in vitro* (figure 32 A & B). To investigate the impact of FGFR4 blockade *in vivo*, dnFGFR4-transfected U251MG cells were injected subcutaneously into the right flank of 8-week old female SCID mice. Control GFP xenograft models had to be sacrificed between day 90 and 120, whereas all dnFGFR4 U251MG xenograft mice were still alive at day 350. These results indicate that 3D-growth *in vitro* as well as tumorigenicity *in vivo* was disrupted upon FGFR4 blockade.

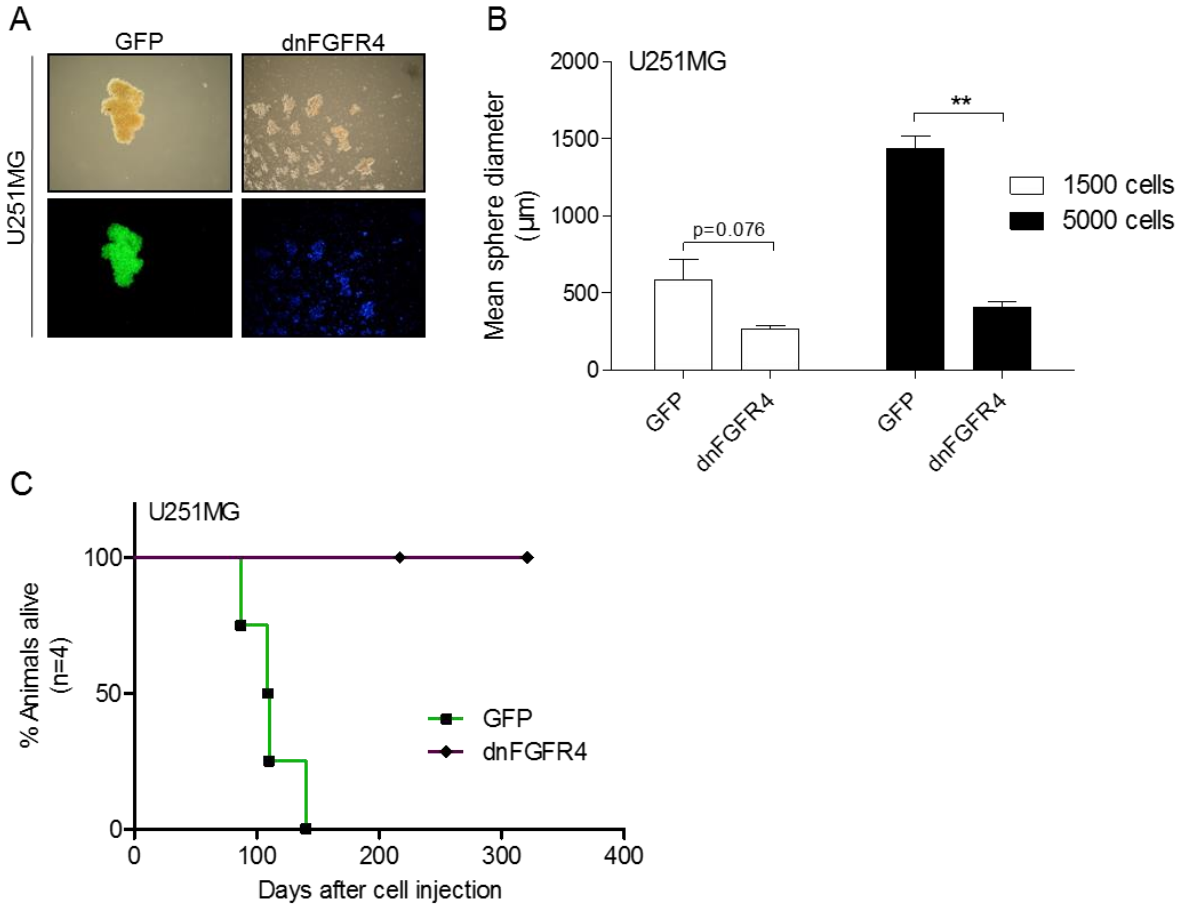

Figure 32. Reduced 3D-growth *in vitro* and low tumorigenicity *in vivo* upon FGFR4 blockade. A) dnFGFR4 transfected cells were used to investigate 3D-growth capacity in vitro by seeding 1500/5000 cells and 7 day incubation time in NB^+ medium to form neurospheres. Photomicrographs were taken at identical time points. B) Mean sphere diameters were quantified. (t-test, **p <0.01, error bars indicate mean ± SD). C) In addition, survival after s.c. xenograft injection of dnFGFR4 transfected cells was investigated and compared to the respective GFP-transfected control (Kaplan-Meier curve of the GFP control group (n=4) and dnFGFR4 transfected U251MG group (n=4)).

4.3. Cloning of wild-type *FGFR4* full-length gene into a GFP plasmid backbone to generate FGFR4_Gly/Arg_GFP fusion-gene constructs

FGFR4_Arg/Gly_GFP fusion-gene vectors were generated to overexpress FGFR4 in FGFR4^{low} expressing cell lines and to allow a localization of FGFR4 intracellularly. To investigate the differences on cell-biological level between the arginine (Arg388) and glycine (Gly388) variants caused by a SNP at codon 388, both FGFR4_Arg_GFP and FGFR4_Gly_GFP constructs were generated. FGFR4 expression vectors, lacking GFP and containing either the Gly388 or Arg388 variant, were used to amplify wild-type full-length FGFR4. These amplified fragments were inserted into a GFP-encoding retroviral plasmid to generate a FGFR4_GFP fusion construct. Both generated constructs were sequenced to analyze the fusion sites of the fragment into the backbone and to verify SNP identity.

4.3.1. Gly388Arg SNP identification

Before amplification of both FGFR4_Arg and FGFR4_Gly genes from the respective vectors, presence of the correct SNP was confirmed. Restriction fragment length polymorphism (RFLP)-technique was performed to identify the Gly388Arg SNP at codon 388 in the respective constructs.

The gel picture of the RFLP in figure 33 shows the undigested FGFR4 (SNP region) PCR fragments on the left and digested fragments on the right side. Both Arg388 and Gly388 were identified using a positive Gly388 control during the PCR and RFLP techniques. The Gly388-positive control indicated visible bands as PCR product and as digested

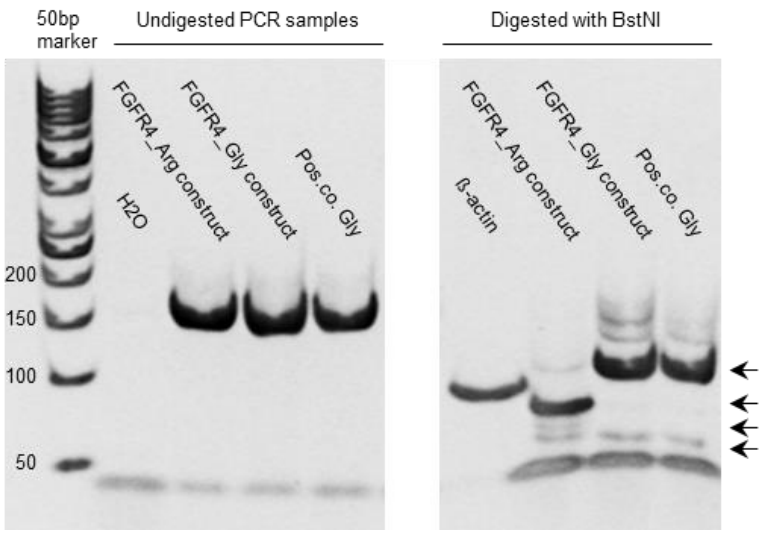

Figure 33. RFLP gel picture identifying the Arg388 and Gly388 variants in FGFR4 expression vectors. *FGFR4*-gene was PCR-amplified using primers flanking SNP location. To analyze SNP variant, PCR products were BstNI-digested and separated by 15% acrylamide gel electrophoresis. Undigested PCR fragments are depicted on the left side of the gel, digested PCR samples on the right.

product. Thus, the FGFR4_Arg and FGFR4_Gly constructs were compared to the Gly388 positive control. Similarities were found between the FGFR4_Gly vector and Gly388 positive control. The SNP causing the G388A mutation generates an additional cutting site for restriction enzyme BstNI, in addition of two already existing sites in the PCR fragment. This additional restriction site resulted in three fragments for the FGFR4_Gly variant at 22, 37 and 109 bp and four fragments for the FGFR4_Arg variant at 22, 29, 37 and 80 bp. The intense band at approximately 110 bp confirmed the absence of a SNP in the FGFR4_Gly vector whereas the FGFR4_Arg vector resulted in a band below 100bp (~80 bp). These findings confirm that the vectors were correct and thus, the fragments were further used for cloning.

4.3.2. In-Fusion® cloning primer design

Generating a fusion-gene (FGFR4_GFP) by In-Fusion® cloning technology includes primer design to amplify the fragment that will be inserted into the recipient vector. Parts of the forward and reverse primers (18 bp) were complementary to both ends of the FGFR4_Gly and FGFR4_Arg full length coding regions, mutating the “STOP” codon to generate a read-through sequence. To make use of the In-Fusion® cloning kit, a 15 bp primer extension, complementary to the target vector (GFP) starting from the cut site, was added at the 5’ ends of the primers. Functioning primers led to ~2 kb PCR products, representing the FGFR4 coding sequence size.

FGFR4 fragment amplification, using the newly designed In-Fusion® primers targeting FGFR4 (without “stop” codon), showed ~ 2 kb PCR products after running a gradient PCR with temperatures reaching from 55-70°C. FGFR4_Arg (figure 34A) as well as FGFR4_Gly (figure 34B) vector amplification with the new primers in combination with 68-70°C melting temperature resulted in most intense bands on the agarose gel. Therefore, this temperature range was chosen as preferred range for the FGFR4 In-Fusion® primers to obtain optimal product amplification. The amplified products were purified and used for the cloning procedure.

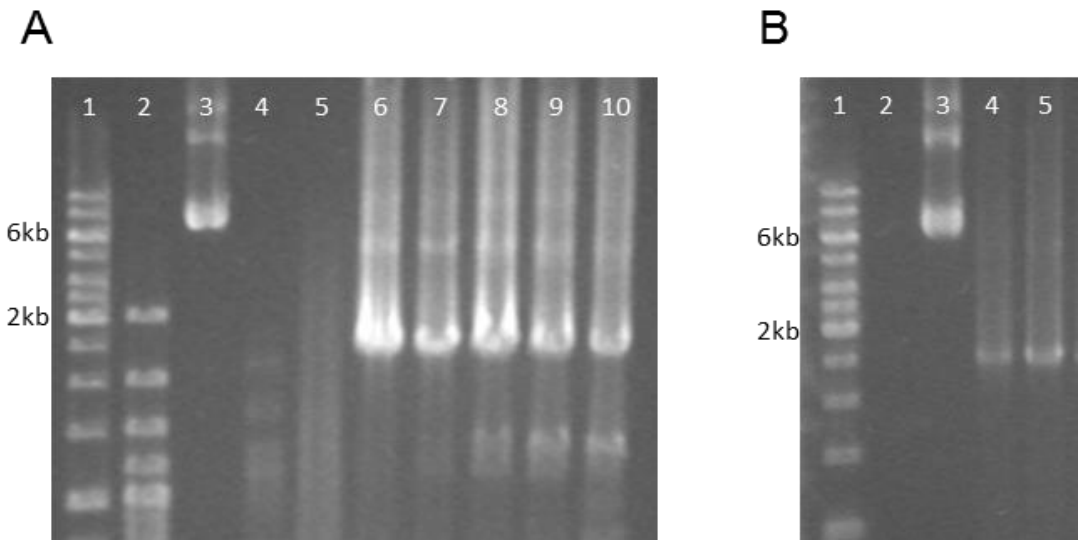

Figure 34. Agarose-gel (0.8%) electrophoresis analysis of FGFR4 PCR products obtained with newly designed In-Fusion® primers. A) FGFR4_Arg construct PCR products obtained after a 55-70°C gradient PCR with the new In-Fusion® primer pair. The 1 kb gene ruler and 100 bp+ marker were loaded in slot 1 and 2, respectively, slot 3 harbors pure construct (no PCR product), slot 4 is a FGFR4_Arg PCR product generated with another polymerase (PFU) which failed, slot 5 contains the negative H2O control and slots 6-10 the FGFR4_Arg PCR products at temperature 70°C, 68°C, 65°C, 60°C & 55°C. B) Amplified FGFR4_Gly construct indicating a 1 kb gene ruler in slot 1, H2O negative control in slot 2, pure construct (no PCR fragment) in slot 3 and PCR product obtained at 70°C and 68°C in slots 4 and 5, respectively.

4.3.3. In-Fusion® cloning

Purified FGFR4_Arg and FGFR4_Gly fragments were cloned into a linearized (using BamHI) GFP backbone. Insertion of these fragments into the GFP backbone generated a fused open reading frame of FGFR4 and c-terminal GFP via the newly introduced read-through at the mutated FGFR4 stop codon. Linearization of the GFP vector with BamHI resulted in higher bands than the non-linearized control, at approximately 7 kb, on a 0.8% agarose gel (data not shown). This indicated successful linearization, as linearized DNA runs slower than circular DNA.

Further, cloned samples were analyzed for ligation and insertion accuracy by running agarose gels of undigested and digested (with NotI) cloning products after performing a mini-prep isolation. NotI exhibits cutting sites at the beginning the FGFR4 insert and downstream of the GFP region on the target vector. Figure 35 indicates successfully cloned constructs resulting in 3184 bp (depicting FGFR4+GFP) and 7175 bp fragments on an agarose gel after restriction with NotI. Plasmids lacking the FGFR4 insert showed the same 7175 bp fragment, confirming the presence of the backbone vector, and, in addition, a 772 bp fragment (GFP sequence without FGFR4).

Gel-electrophoresis analysis of mini-prep samples depicted that only one single sample of the FGFR4_Arg_GFP (figure 35, panel A) and two of the FGFR4_Gly_GFP (figure 35, panel B) generated constructs were lacking the target insert. With focus on the most intense bands, indicative for highest DNA yield, FGFR4_Arg_GFP #7 and FGFR4_Gly_GFP #2 were selected to perform retransformation and DNA isolation via midi-prep.

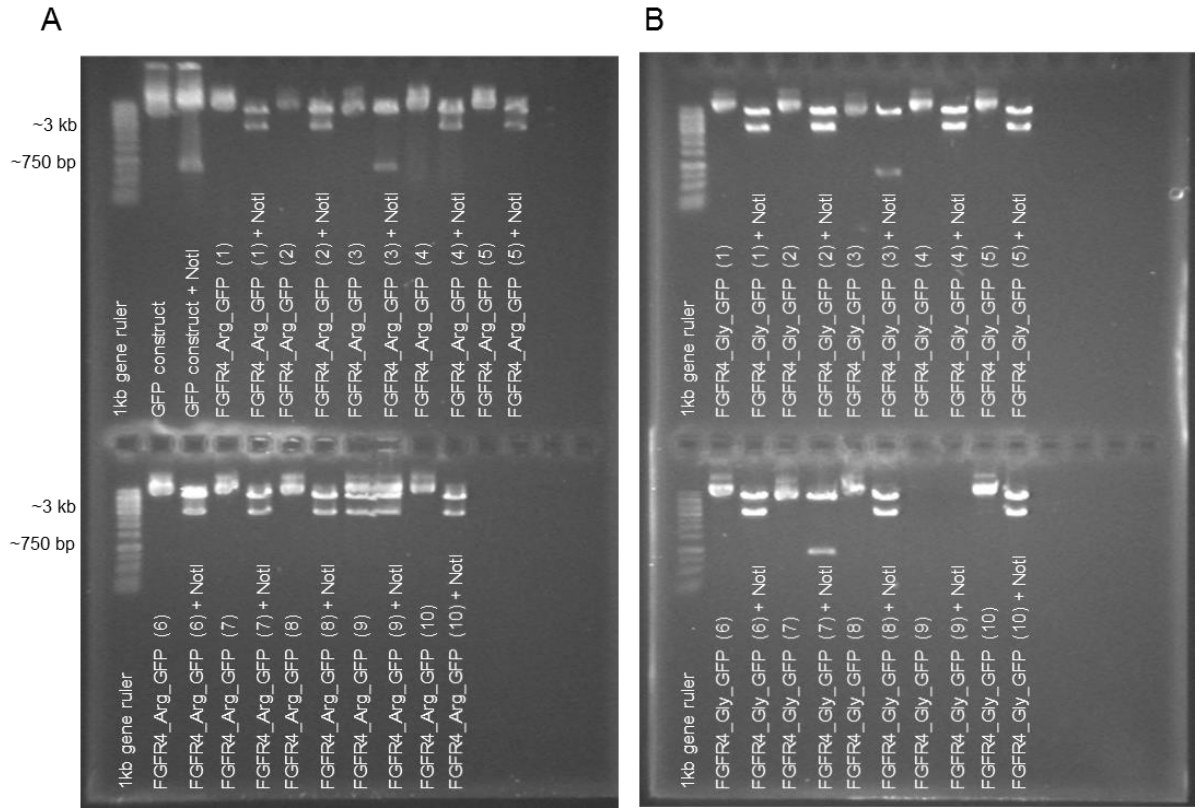

Figure 35. Accurate wild-type full-length FGFR4_Arg and FGFR4_Gly cloning into a GFP vector. GFP vector samples in lane 2 and 3 of panel A serve as negative control, 10 mini-prep samples per generated construct (FGFR4_Arg_GFP and FGFR4_Gly_GFP) were loaded on a 0.8% agarose gel in pure form or after restriction digest with NotI for 1 h, A) indicates the 10 FGFR4_Arg_GFP samples and B) the 10 FGFR4_Gly_GFP samples. Bands showing a size of approximately 3 kb indicate accurate cloning products, whereas the bands around 750 bp in size indicate wrong ligation and absence of the FGFR4 sequence.

Construct integrity after transformation of bacterial cultures was again verified by NotI digestion and loading on a 0.8% agarose gel after midi-prep isolation (data not shown). These constructs were further analyzed on their respective fusion sites in the target vector and the presence or absence of the SNP at codon 388 by Sanger-sequencing.

4.3.4. Sequencing of cloned FGFR4_Arg_GFP and FGFR4_Gly_GFP constructs

To analyze the fusion site of both generated constructs and to identify if the polymorphism variant is still present, constructs were sequenced with single primers. Two reverse primers complementary to GFP, one forward primer complementary to the CMV promoter and the two RFLP primers (previously applied for RFLP) were separately used to sequence the FGFR4 and identify the respective polymorphism.

Sequencing results were imported and all acquired sequences were assembled using an assembly software (clone manager) to discover an overlap. The two sequences generated with the GFP reverse primers and the sequence obtained with the RFLP reverse primer yielded identical results for the FGFR4_Arg_GFP as well as the FGFR4_Gly_GFP sequenced constructs. The assembled sequences were blasted against the entire human genomic and transcript database (NIH) and resulted in a 99% identity with *Homo sapiens* FGFR4 sequence. The assembled FGFR4_Arg_GFP sequence resulted in one mismatch at base position 1357 in the mRNA transcript, whereas the FGFR4_Gly_GFP assembled sequence lacked this mismatch. By further analyzing the sequencing data obtained with the RFLP reverse primer, we confirmed the difference in base (from G→A) at position 58/59 in the obtained sequence (figure 36A). This result indicates that the SNP causing the Gly388Arg variation was preserved during the cloning procedure and is located at position 3445 bp in the construct (figure 36B). In addition, RFLP technique was performed to prove the presence of this SNP in the FGFR4_Arg_GFP construct. The Gly388 and Arg388 patterns were visualized on a 15% polyacrylamide gel, indicating 3 bands in the FGFR4_Arg_GFP lane and 2 bands in the lane where FGFR4_Gly_GFP was loaded (data not shown). These results were in accordance with the sequencing data.

Furthermore, sequences with the CMV forward primer were obtained to visualize the entry site of the n-terminal part of the FGFR4 fragment and the GFP vector. These were blasted against the FGFR4 transcript sequences and found to still harbor the “start” codon at position 2284 bp, which is needed to create a functional expression vector (figure 36C). In addition, the important fusion site at the c-terminus of the FGFR4 gene was analyzed to investigate the absence of the “stop” codon at position 4702 bp. Indeed, no “stop” codon was observed at 4702-4705 bp, and correct in-frame fusion of the FGFR4 sequence with the “start” codon of the GFP sequence ranging from 4705-5424 bp was found (figure 36D). These analyses strongly suggest

the correct formation of FGFR4_GFP fusion constructs harboring either the Arg388 or Gly388 variant and a GFP at the c-terminus of FGFR4 resulting in a FGFR4_Arg/Gly_GFP fused sequence ranging from 2284 bp (start codon) until 5424 bp (stop codon) in the vector map as indicated in red in figure 36E.

To investigate the intracellular localization and tumorigenic effects on 2D- and 3D-growth, both FGFR4_Arg_GFP and FGFR4_Gly_GFP were introduced in FGFR4^{low} expressing cell lines HU-MI and U251MG, as described in the next chapter.

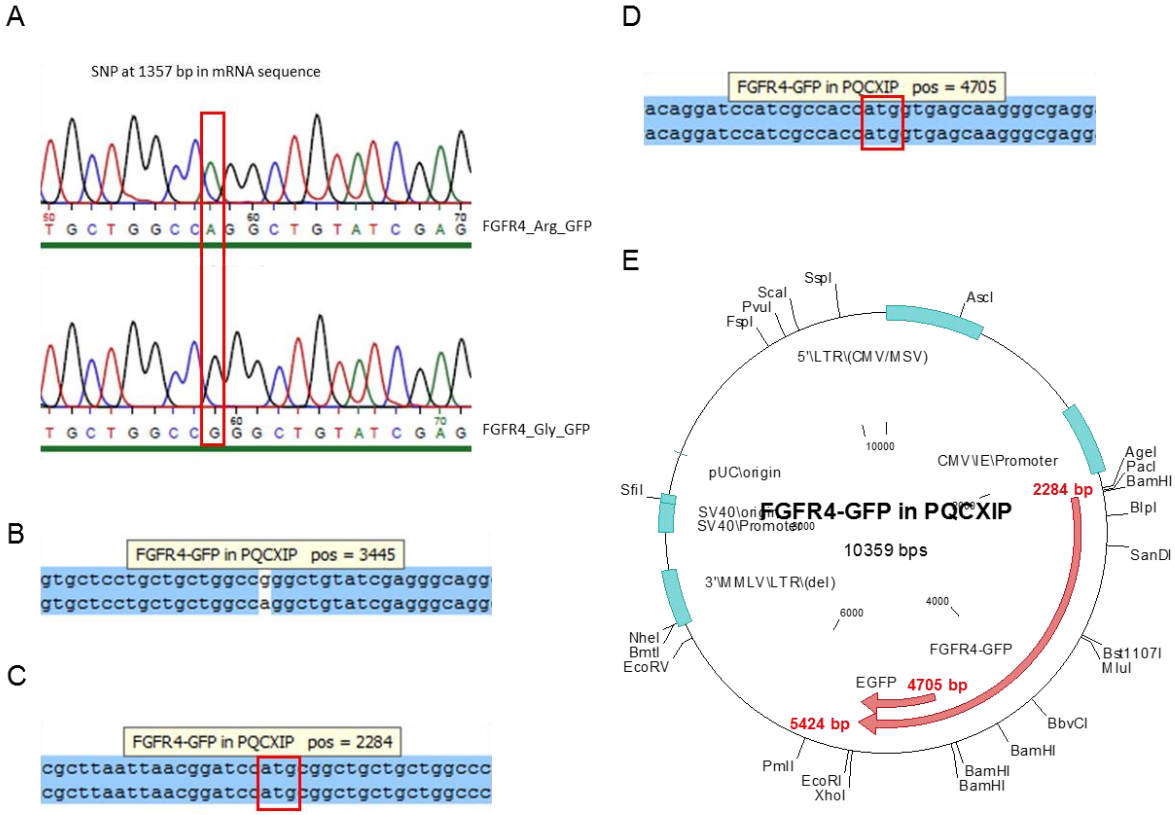

Figure 36. Sequencing results of SNP Gly388Arg variant analysis and fusion sites in the FGFR4_Arg_GFP and FGFR4_Gly_GFP generated constructs. A) Plasmid Sanger sequencing results of both FGFR4_Arg_GFP and FGFR4_Gly_GFP constructs with RFLP reverse primer, indicating the SNP at transcript position 1375 bp. B) Alignment of the assembled sequences obtained after Sanger sequencing with GFP and RFLP reverse primers aligned with the construct sequence harbouring FGFR4, generated in clone manager. The mismatch at position 3445 indicated the position of the SNP in the generated construct. C) N-terminal fusion site of the FGFR4 fragment and the GFP target vector analyzed by alignment of the CMV forward primer obtained sequence and the newly generated construct sequence. The red box indicated the FGFR4 start codon at position 2284. D) Alignment of the GFP reverse primer-obtained sequence and the generated construct sequence to visualize the fusion site at the FGFR4 C-terminus with GFP. The red box indicates the start codon at 4705 bp coding for GFP, and the absence of a stop codon at 4702-4704, which proves the accurate cloning product and generation of a fusion between FGFR4_GFP. E) Expression vector map of the PQCXIP plasmid containing the fused FGFR4_GFP sequence (2284-5424 bp).

4.4. Ectopic expression of FGFR4_GFP Arg388 and Gly388 variants in low expressing GBM cell lines and the effects on 2D- and 3D-growth and proliferation rate

To assess the role of FGFR4 in GBM, low expressing HU-MI primo-culture and commercially available GBM cell line (U251MG) were stably transfected with the FGFR4_Arg_GFP and FGFR4_Gly_GFP fusion-gene constructs. The generated FGFR4_GFP fusion-gene yielded the opportunity to localize the FGFR4_GFP fusion protein intracellularly by fluorescence microscopy. Further, the effects of FGFR4 introduction on proliferation rate, clone forming capacity, 3D-growth and migration were analyzed.

4.4.1. Transfection efficiency and the proliferative effect of FGFR4 expression modification in FGFR4^{low} cell lines

HU-MI and U251MG cell lines were transfected with either FGFR4 Arg388 or Gly388 variant constructs and compared to the respective GFP transfected control. In total, eight cell lines were transfected but only two out of these eight survived the entire transfection procedure with lipofectamine2000®, transgene exposure, trypsinization, transfer into new flasks and constant selection with puromycin (1µg/ml). Therefore, all

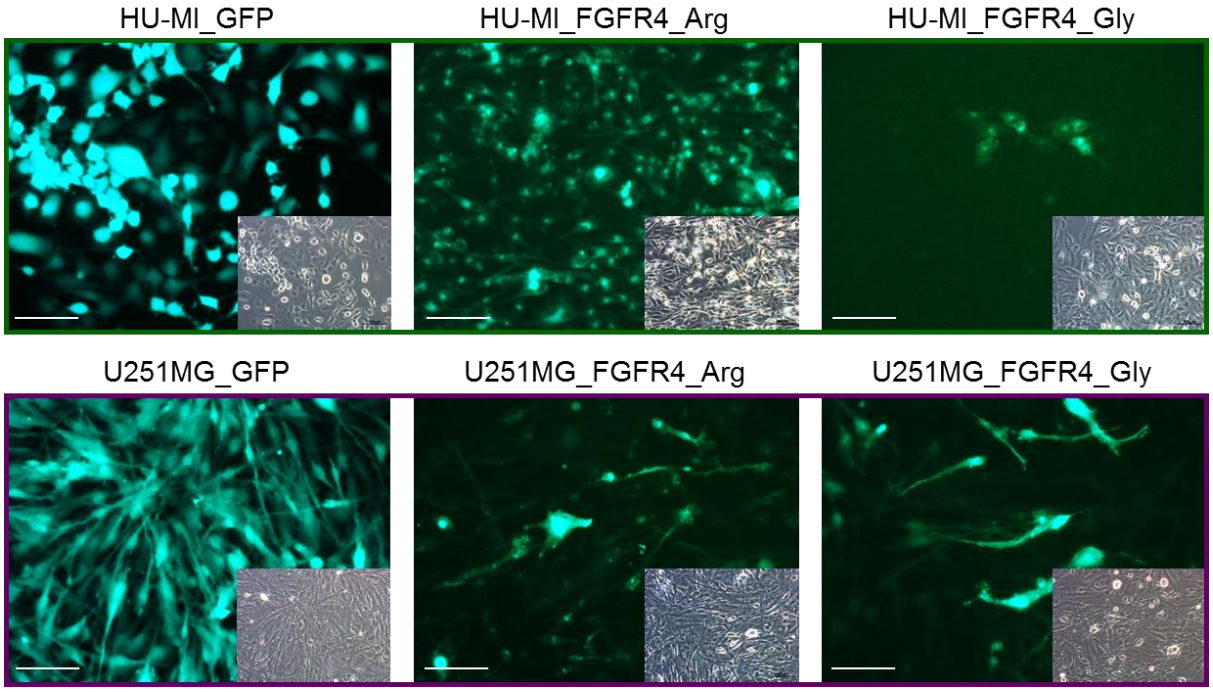

Figure 37. Transfection efficiency 3-days post-transfection of HU-MI and U251MG cells. Cells were exposed to plasmid and Lipofectamine2000® mixture for 8 h. Transfection rate was determined by fluorescence microscopy using the FITC/GFP channel and brightfield. Photomicrographs were taken 3-days post-transfection. Scale bars indicate 50 µm.

experiments with transfected cells were performed with the surviving HU-MI and U251MG (FGFR4_Arg, FGFR4_Gly & GFP) sublines.

Transfection efficiency directly after the procedure appeared extremely high in the GFP transfected cells and in HU-MI_FGFR4_Arg cells but relatively low in the U251MG_FGFR4_Arg and both FGFR4_Gly sublines (figure 37). Continuous selection of the transfected cells was performed by permanent exposure to 1 µg/ml puromycin. Six-to-twelve weeks after transfection, the efficiency was analyzed by flow cytometry, quantifying GFP positive and negative cells. Primary HU-MI sublines indicated high GFP and FGFR4_Arg_GFP transfection efficiency in contrast to very low levels of FGFR4_Gly_GFP (100%, ~80% and ~10%, respectively, figure 38 A). High transfection rates were observed in all three U251MG sublines, exhibiting 98-100% GFP positive cells (figure 38B).

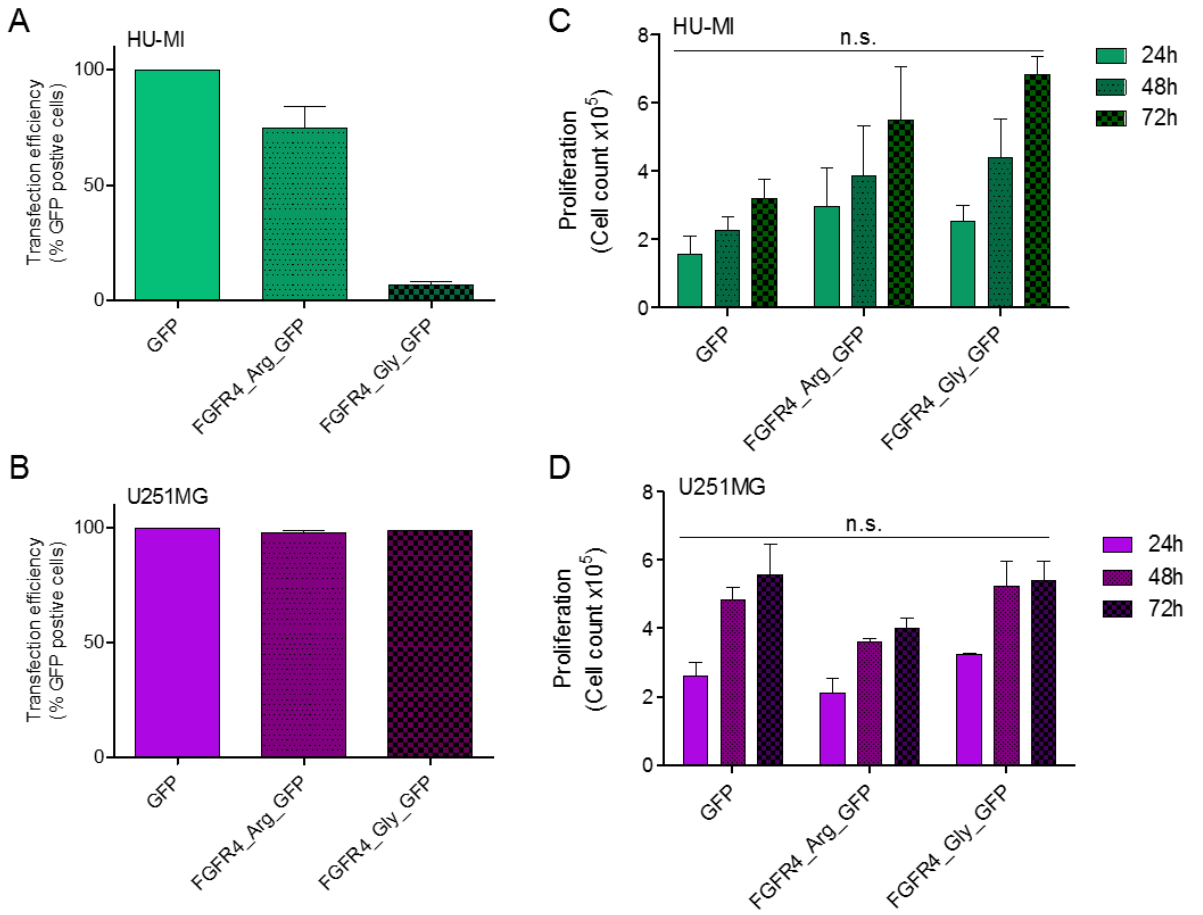

Figure 38. Highly GFP-positive cell populations obtained by transfection in HU-MI_GFP and HU-MI_FGFR4_Arg and all U251MG transfected sublines. Transfection efficiency was quantified by flow cytometry analysis of trypsinzed transfected sublines, measuring GFP positive and negative cells in the FITC channel. A) Transfected HU-MI cells indicating high GFP levels in the GFP and FGFR4_Arg_GFP sublines in contrast to the low GFP levels in the FGFR4_Gly_GFP cell line. B) High transfection efficiency was reached in all U251MG sublines with GFP positive cells ranging between 98-100%. C-D) Proliferation rates were evaluated by determining and counting cells at the indicated time points. Statistics calculated using one-way-ANOVA, error bars indicate mean ± SD

Furthermore, proliferation rates in both HU-MI and U251MG FGFR4_Arg_GFP and FGFR4_Gly_GFP sublines did not significantly differ within the indicated time points as compared to the GFP control cell lines, although after 72h the HU-MI_FGFR4_Gly_GFP subline showed a slight increase in viability (figure 38 C-D). These findings indicate that the introduced constructs do not strongly influence their proliferation capacity in 2D-culture conditions.

4.4.2. Subcellular FGFR4 localization in transfected HU-MI and U251MG sublines

Manipulation of FGFR4 expression in HU-MI and U251MG cells with the fusion-gene constructs enabled us to localize FGFR4 intracellularly. To investigate the intracellular distribution of ectopically expressed FGFR4, we performed confocal laser microscopy. Transfected cells were fixed with 4% PFA, nuclei stained with DAPI and membranes with WGA. While GFP was localized throughout the entire cells, FGFR4_Arg_GFP and FGFR4_Gly_GFP transfected cells indicated distinct peri-nuclear localization (figure 39A). Fractionation of all HU-MI and U251MG sublines and parental cells into nuclear, cytoplasmic and total fractions was performed to identify the subcellular protein localization in more detail. Western blot analysis (figure 39B)

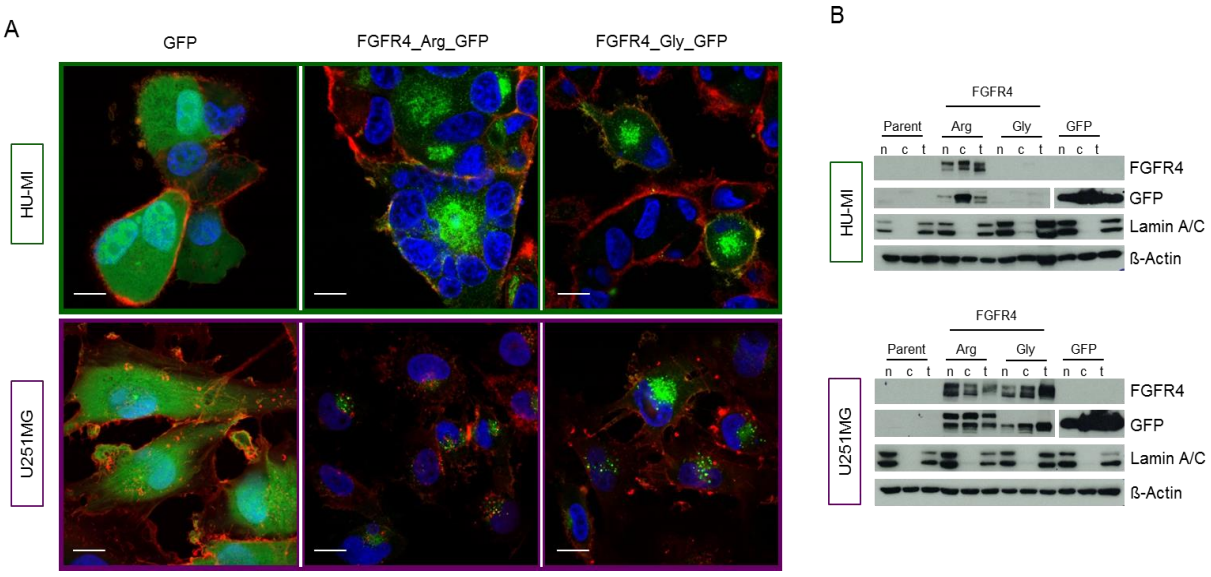

Figure 39. Subcellular FGFR4 localization in proximity to the nucleus in HU-MI and U251MG sublines. A) Confocal LSM photomicrographs of transfected HU-MI and U251MG cells after 4% PFA fixation and staining with DAPI (nuclei) and WGA (membranes), using 63x objective with immersionoil, pinhole = 40. Scale bars, 10 µm. B) Western blot analysis of nuclear (n), cytoplasmic (c) and total (t) protein fractions of parental and transfected HU-MI and U251MG sublines. Lamin A/C serves as control for accurate separation between cytoplasmic and nuclear fractionation, ß-actin serves as loading control.

revealed presence of FGFR4 in cytoplasmic (indicated with c) as well as nuclear (n) and total extracts (t), Lamin A/C served as control for separation of cytoplasmic and nuclear fractions. GFP was present as small protein in the GFP sublines, whereas the HU-MI FGFR4_Arg_GFP and U251MG FGFR4_Arg_GFP as well as FGFR4_Gly_GFP indicated GFP bands at the height of FGFR4. In addition, western blot data strongly confirm the flow cytometry results mentioned above, indicating low transfection efficiency of the HU-MI_FGFR4_Gly_GFP subline.

4.4.3. Ectopic FGFR4 overexpression induced 2D- and 3D-growth aggressiveness and enhanced migratory potential in U251MG GBM cells

As no indications of strongly altered proliferation -in relation to the GFP transfected control- were found in the proliferation experiment mentioned above, the effects of ectopic FGFR4 expression on clone formation capacity, 3D-neurosphere growth and migratory potential in the $FGFR4^{low}$ cell lines HU-MI and U251MG were of high interest. Accordingly, HU-MI and U251MG (FGFR4_Arg_GFP and FGFR4_Gly_GFP sublines) were compared to their respective GFP-transfected control cell lines. The difference between the Arg388 and Gly388 polymorphic variants was our main focus based on reports , indicating a higher risk on cancer in patients harboring the Arg388 germline variant. Further, SNP variant Arg388 serves as negative prognostic marker in several cancer types (e.g. prostate cancer) [149-152].

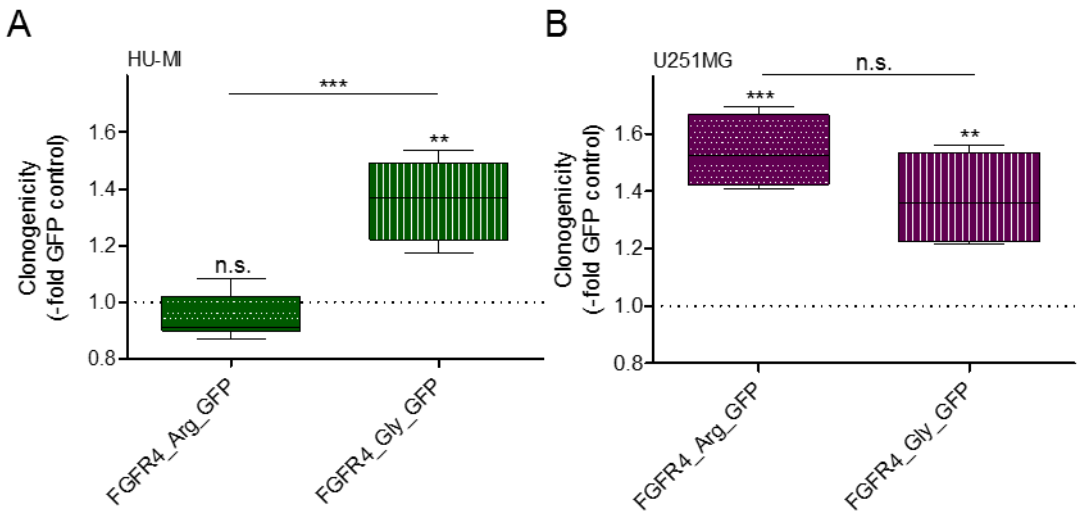

Figure 40. Enhanced clone forming capacity upon modulation of FGFR4 expression in U251MG cells. Cells were seeded (1000 cells per well) and left to form clones for 7 days. Clones were fixed in pure methanol and stained with crystal violet. Graphs indicate the absorbance intensity at 560 nm of crystal violet dissolved in 2% SDS. A) Box blots indicating the clone forming capacity of HU-MI and B) of U251MG FGFR4-transfected cells, both normalized to the GFP control absorbance measurements. Statistical differences between the Arg388 and Gly388 variants were calculated using unpaired student's t-test, ***p <0.001, indicated by the bar above both boxes. Statistical differences between both variants and their respective GFP control were calculated using column statistics with a hypothetical value of 1.0, **p <0.01, ***p <0.001, indicated directly above the boxes. Error bars show SD.

Colony forming capacity of HU-MI cells upon transfection indicated no significant differences between the FGFR4_Arg_GFP subline and the respective GFP control (figure 40A). HU-MI_FGFR4_Gly_GFP cells were characterized by significantly enhanced clonogenicity as compared to the GFP control. On the contrary, modification of FGFR4 with both Arg388 and Gly388 variants significantly (***p <0.001 and **p <0.01, respectively) improved clone formation capacity in U251MG cells in relation to the GFP-transfected control subline (figure 40B). However, no significant difference was found between the Arg388 and Gly388 U251MG subclones in this cell line.

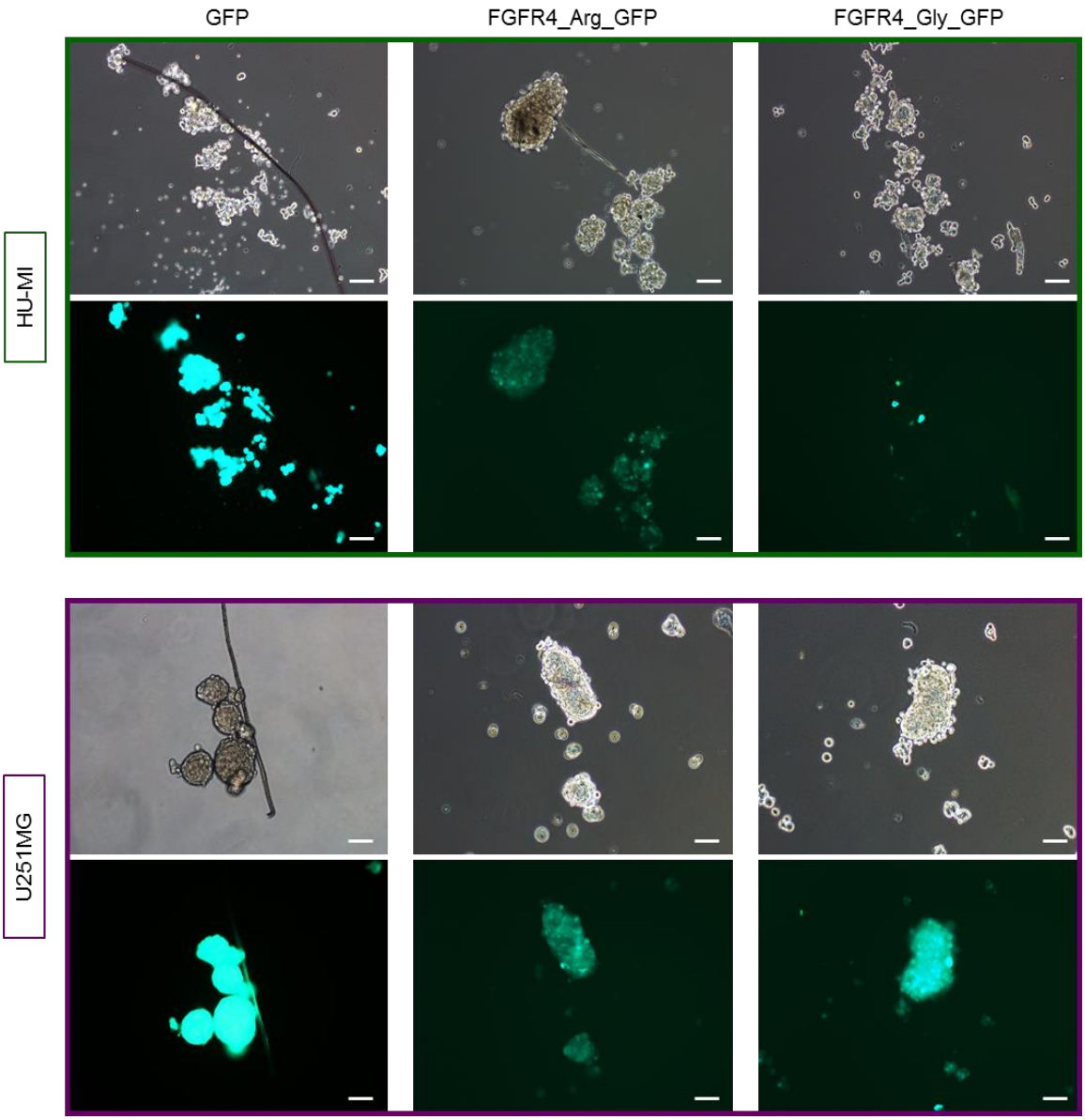

Figure 41. 3D-neurosphere formation of HU-MI and U251MG transfected cells. Cells were grown in low-attachment plates with NB+ medium supplemented with growth factors (bFGF and EGF). Photomicrographs were taken with a Nikon Eclipse Ti (10x objective), fluorescence microscope, 96 h after seeding. Scale bars indicate 100 µm.

Moreover, FGFR4 modification clearly influenced 3D-neurosphere formation in HU-MI as well as U251MG cells. Introduction of the Arg388 variant enhanced the tendency to form a single giant neurosphere instead of the numerous smaller spheres, seen in the GFP control (figure 41). This giant sphere formation was also observed in the U251MG_FGFR4_Gly_GFP cell line. Poorly transfected HU-MI_FGFR4_Gly_GFP cells revealed 3D-growth capacities similar to the GFP control cell line (compare figure 40) and the parental HU-MI cell line (data not shown).

Focusing on cell motility, induced FGFR4 expression significantly enhanced migratory and invasive potentials of all GBM cells analyzed. At first, transfected HU-MI and U251MG cells were seeded in inserts harboring 8 µm pores in 24-well plates. After 48 h migration time, cells at the bottom of these inserts were fixed, stained and absorbance was measured to quantify the migratory potential of the cells.

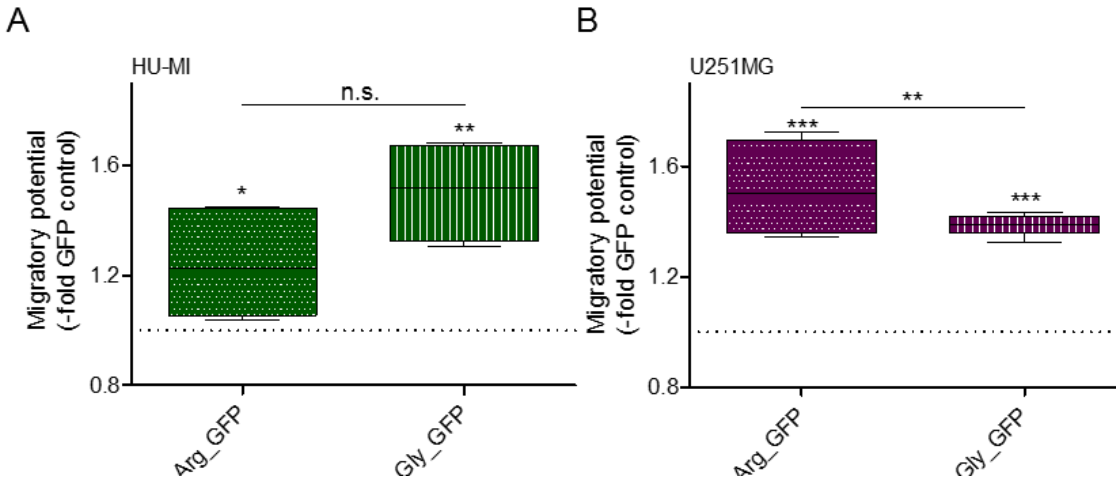

Figure 42. Enhanced migratory potential of HU-MI and U251MG FGFR4 transfected cells. Cells were seeded in inserts harbouring 8 µm pores and left for 48 h to migrate through these pores. Migrated cells were fixed with methanol, stained with crystal violet and absorbance was measured of crystal violet stained cell, dissolved in 2% SDS at 560 nm. A) Shows the migratory potential of HU-MI_FGFR4_Arg_GFP and HU-MI_FGFR4_Gly_GFP cells relative to the GFP control cell line. B) Indicates the migratory potential of both Arg388 and Gly388 transfected U251MG cell lines in relation to the respective GFP control. Statistical differences between the Arg388 and Gly388 variants were calculated using unpaired student's t-test, **p <0.01 and n.s., non-significant, indicated by the bar above both boxes. Statistical differences between both variants and their respective GFP control were calculated using column statistics with a hypothetical value of 1.0, *p <0.05, **p <0.01, ***p <0.001, indicated directly above the boxes.

Significantly enhanced migratory potential was observed in all of the FGFR4 transfected sublines (HU-MI and U251MG, figure 42). U251MG revealed the greatest migratory induction as compared to the GFP control (***p <0.001, figure 42.B). Additionally, HU-MI Arg388 and Gly388 did not strongly differ regarding migration capacity whereas the U251MG_FGFR4_Arg_GFP subline exhibited a significant increase (**p <0.01) in migratory potential relative to the Gly388 variant.

To complement these findings, cells were densely seeded onto an 8-well chamber slide, left to adhere, followed by formation of scratches into the confluent cell layer. Every 30 minutes for 32 h, the scratched areas were recorded using live-cell imaging. This technique mimics the process of wound healing and enabled us to analyze the migratory potential of cells additionally to the trans-well assay.

Cell migration was observed after approximately 10 h in HU-MI and 5 h in U251MG sublines. No distinct differences were measured between the HU-MI sublines in the first 20 h (figure 43A), in contrast to significantly higher motility in U251MG_FGFR4_Arg_GFP compared to the other U251MG cell lines at the same time point (figure 43B). Cell motility was recorded at low magnification using a 10x objective, revealing wound closure by U251MG Arg388 variant after 27 h. Remaining

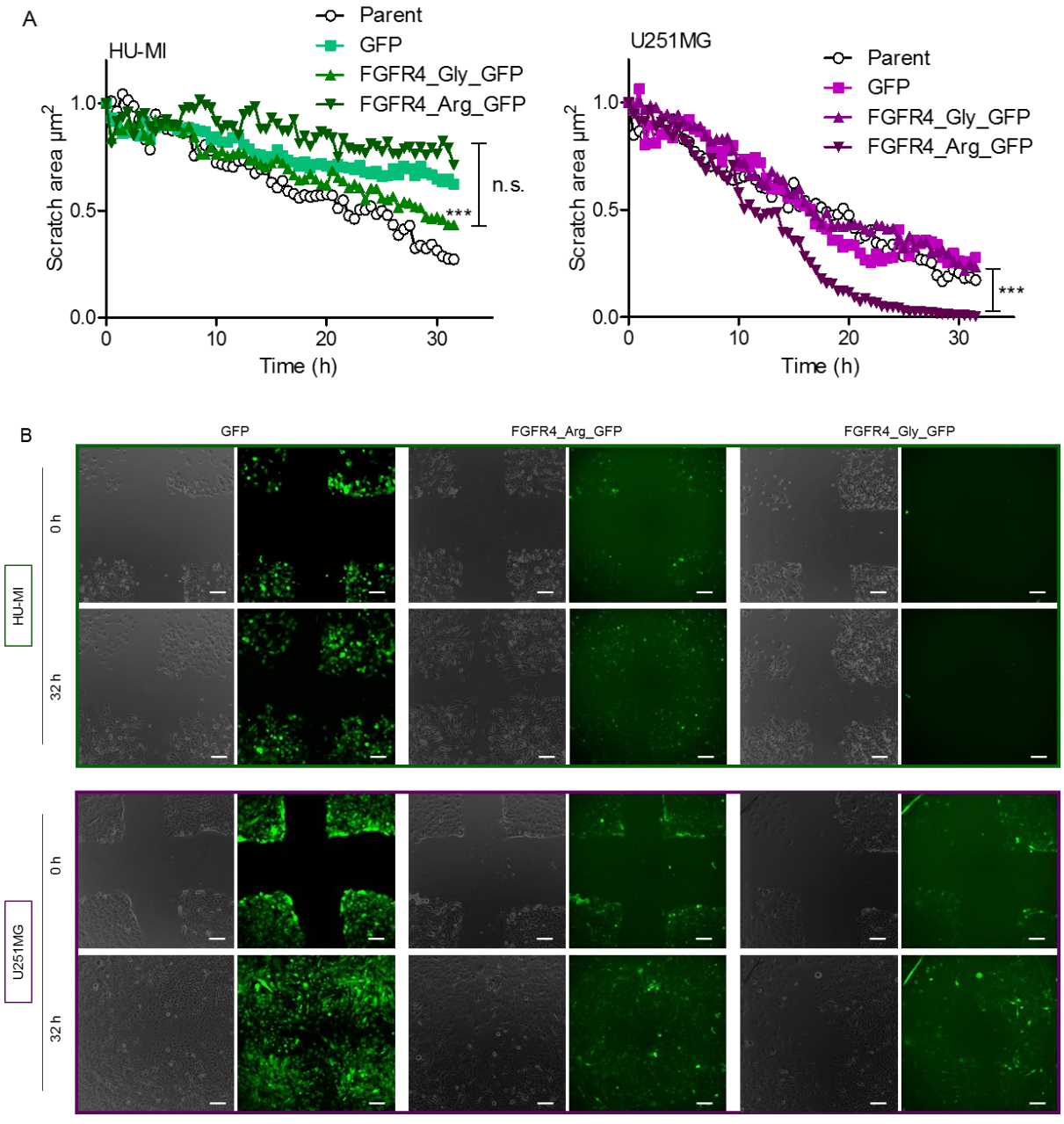

Figure 43. Enhanced wound closure upon FGFR4_Arg_GFP transfection in U251MG cells. Cells were seeded in an 8-well chamber slide, left o/n to grow a confluent monolayer, and scratches were made with a p10 tip. Motility was recorded every 30 min, using a live-cell imaging system. A) Represents quantification of the scratch area (μm^2), analysed with Tscratch software. Significant differences were analysed using two-way-ANOVA, comparing the FGFR4 transfected samples to each other and to the GFP control, ***p <0.001. B) Photomicrographs were taken in brightfield and GFP settings using a 10x objective. Indicated are time points 0 h and 32 h representing the start and end of the experiment. Scale bars indicate 100 µm.

U251MG cell lines and the entire HU-MI panel were not able to fully heal the wound, but closed the scratch partially (figure 43 A&B).

Taken together, U251MG exhibited higher migratory potential (relative to GFP) upon FGFR4 manipulation as compared to HU-MI sublines. Hence, U251MG transfected sublines were grown up and injected ($1x10^6$ cells/mouse, subcutaneously) into 8-week old female SCID mice. Preliminary data indicate enhanced tumorigenicity in the U251MG FGFR4 transfected sublines as compared to the GFP control cell model (50% compared to 25% measurable tumors, respectively). However, this *in vivo* experiment was started at a late time point and expected to finish after the completion of this thesis.

4.5. Inhibitory effects of the pan-FGFR inhibitor ponatinib on FGFR4 Arg388 and Gly388 overexpressing HU-MI and U251MG cells

4.5.1. Alteration of subcellular FGFR4 localization in transfected HU-MI and U251MG cells upon FGFR inhibition

FGFRs are known to be internalized upon FGF ligand binding, resulting in intracellular FGFR localization [153]. As mentioned in 3.5.2., cells transfected with the FGFR4_Arg_GFP and FGFR4_Gly_GFP constructs exhibited predominantly perinuclear FGFR4 localization. The pan-FGFR inhibitor ponatinib was applied to investigate whether blockade of FGFR signaling leads to a shift from perinuclear to membranous localization due to enhanced receptor stabilization at the cell membrane. While untreated HU-MI_FGFR4_Gly_GFP cells exhibited GFP signal at both the cell membrane (co-localization with WGA staining) and at perinuclear sites, the Arg388 variant localized predominantly to the perinuclear region (figure 44A). Only a trend towards enhanced membrane localization was observed after 1 h high dose (10 µM) ponatinib exposure, especially in HU-MI_FGFR4_Gly_GFP cells (figure 44B).

Moreover, FGFR inhibition in both U251MG FGFR4 sublines did not indicate a shift in GFP signal from peri-nuclear towards the plasma membrane (figure 45B), when compared to the untreated control (figure 45A). Interestingly, ponatinib treatment of the U251MG FGFR4 transfected sublines resulted in a shift from an endoplasmic reticulum(ER)-like perinuclear GFP localization towards a vesicular Golgi-like signal in the cytoplasm.

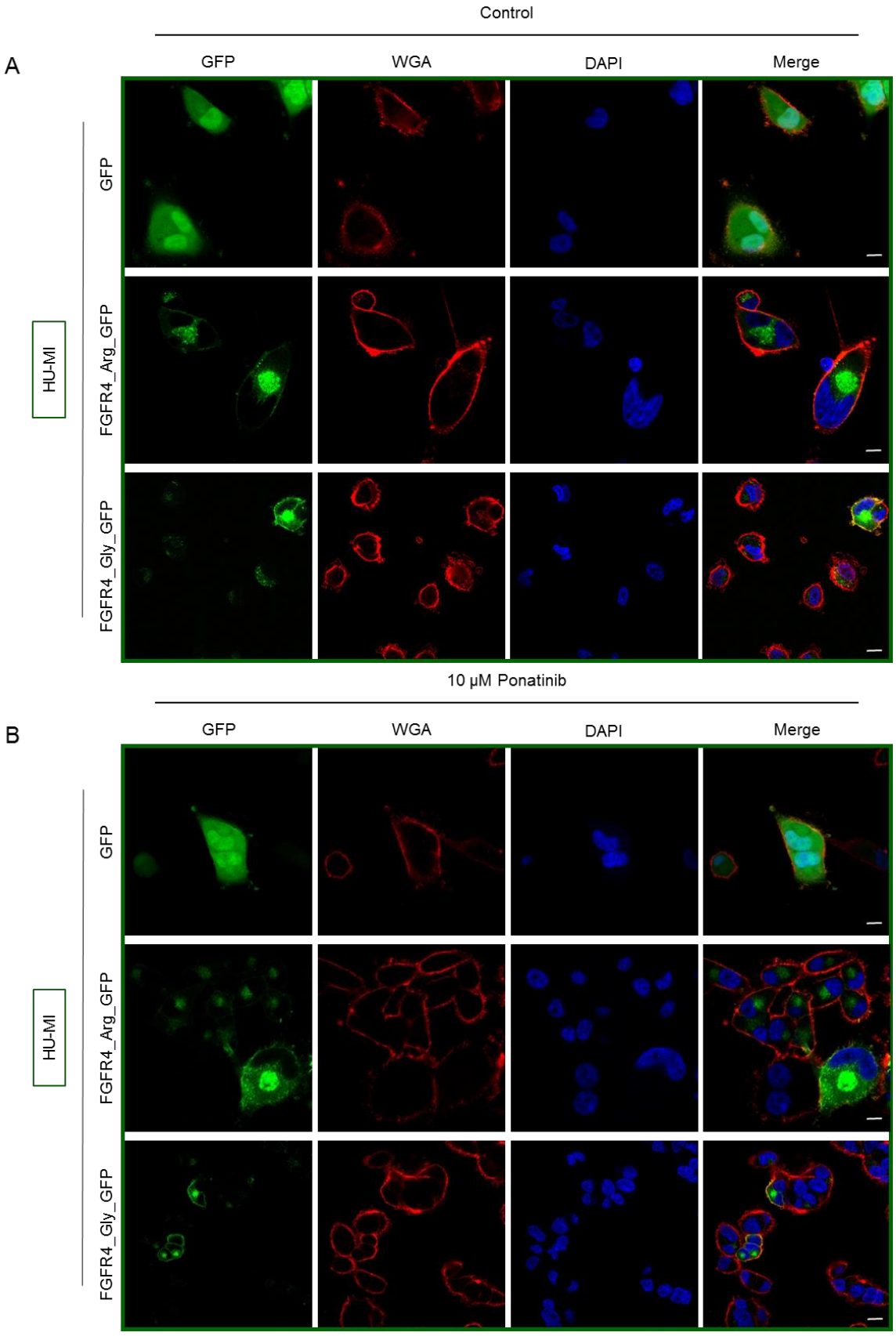

Figure 44. Subcellular localization of FGFR4 Arg388 and Gly388 in HU-MI transfected cells upon ponatinib treatment. Confocal LSM photomicrographs using 63x objective with immersion oil, pinhole = 40 of transfected HU-MI cells control (A) and treated with 10 µM ponatinib for 1 h (B). Upon exposure, cells were fixed with 4% PFA and stained with DAPI (nuclei) and WGA (membranes). Scale bars, 10 µm.

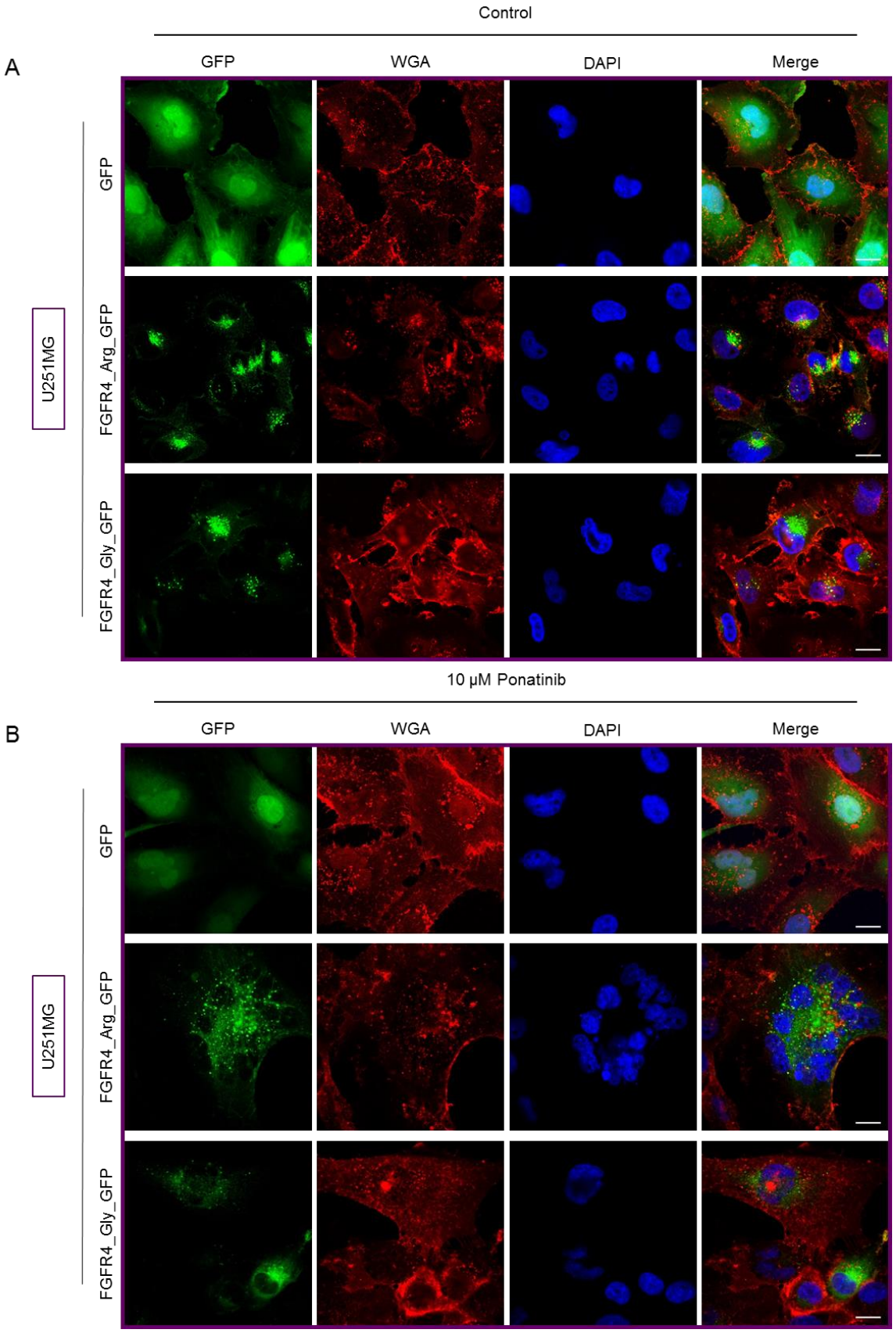

Figure 45. Subcellular localization of FGFR4 Arg388 and Gly388 in U251MG transfected cells upon ponatinib treatment. Confocal LSM photomicrographs using 63x objective with immersion oil, pinhole = 40 of transfected U251MG control cells (A) and treated with 10 µM ponatinib for 1 h (B). Upon exposure, cells were fixed with 4% PFA and stained with DAPI (nuclei) and WGA (membranes). Scale bars, 10 µm.

4.5.2. Impaired 2D- and 3D-growth capacities upon FGFR4-transduction in HU-MI and U251MG cells when exposed to ponatinib

FGFR inhibition by ponatinib resulted in a significantly stronger reduction (***p <0.001) in clone forming capacity of HU-MI Arg388 as compared to the GFP control already at 1 µM, whereas in the Gly388 cell model enhanced inhibitory effects were only observed after treatment with 2.5µM (figure 46A). The Arg388 subline showed more effective FGFR inhibition at 1 µM in relation to the Gly388 variant (**p<0.01). In contrast, clonogenicity impairment by FGFR inhibition in U251MG transfected cells was significantly stronger in case of the Gly388 subline after treatment with 1 µM ponatinib when compared to both Arg388 and GFP cells (**p <0.01 and ***p <0.001, respectively). Interestingly, upon 2.5 µM ponatinib exposure the observed sensitivity differences were less pronounced as compared to the lower dose but still both Gly388 and Arg388 sublines exhibited higher sensitivity towards FGFR inhibition compared to the GFP control (***p<0.001) and Gly388 cells remained the most sensitive.

Additionally, comparable inhibitory effects were observed in 3D-neurosphere cultures (figure 46B). Untreated HU-MI_FGFR4_Arg_GFP and HU-MI_FGFR4_Gly_GFP cells formed bigger spheroids than the GFP transfected control cell line. Further, the sensitivity towards FGFR inhibition by ponatinib was lower in the Arg388 variant (figure 46B, upper panel). HU-MI_FGFR4_Gly_GFP cells exhibited hypersensitivity towards FGFR inhibition with ponatinib. Despite persistence of a visible spheroid in case of HU-MI_FGFR4_Arg_GFP cells, the brownish color indicates massive apoptotic cell death in the inner cell mass (figure 46B, upper panel). Both FGFR4 overexpressing U251MG sublines again tended to form single big spheroids, while multiple smaller ones were observed in the GFP subclone (compare figure 30). Exposure to ponatinib revealed highest sensitivity of the U251MG_FGFR4_Arg_GFP cell line (figure 46B, lower panel), which is in line with clone forming capacity of this cell line upon FGFR inhibition (compare figure 46A).

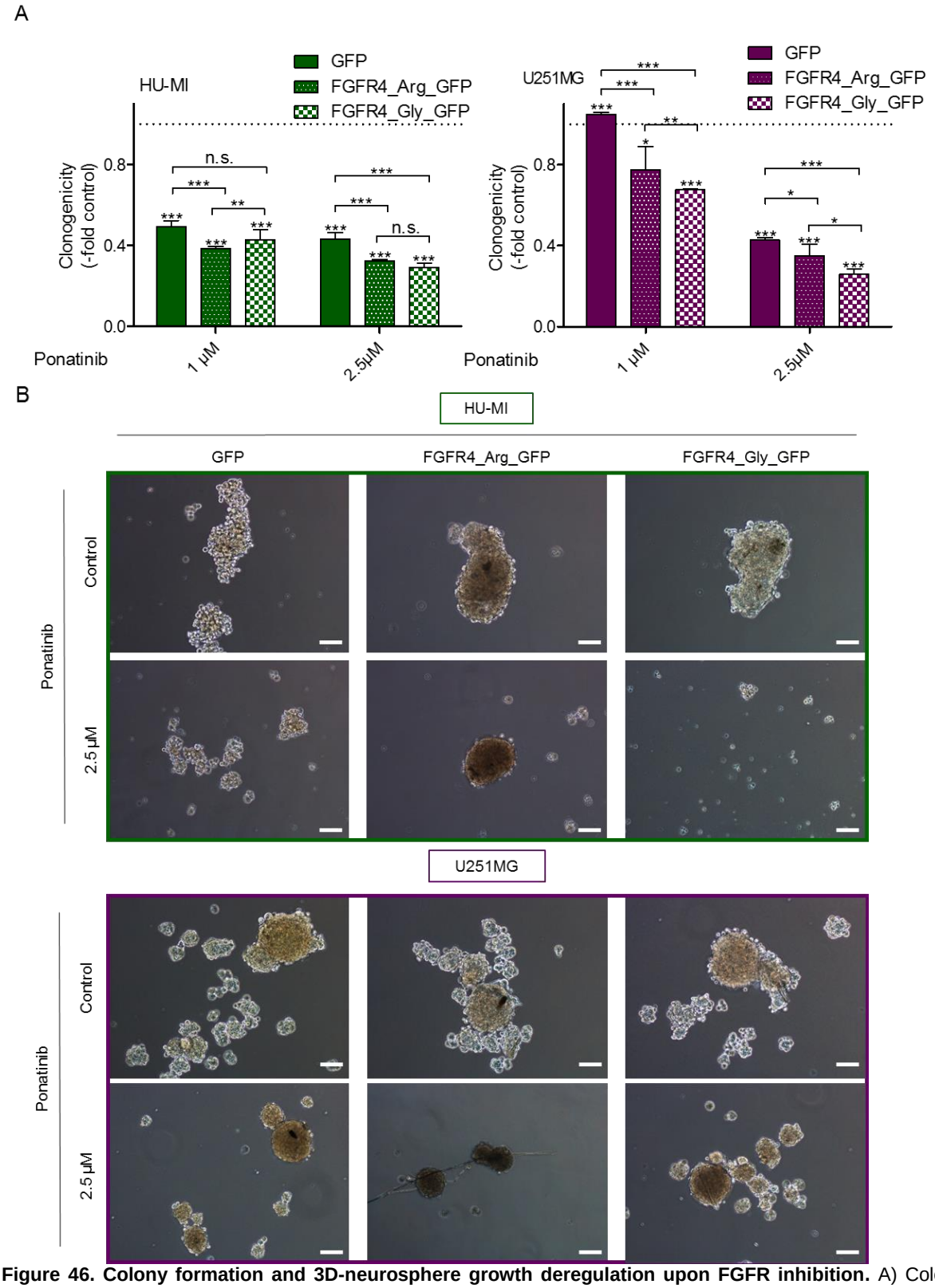

Figure 46. Colony formation and 3D-neurosphere growth deregulation upon FGFR inhibition. A) Colony formation of FGFR4-overexpressing cells was tested by seeding 1000 cells per well, followed by exposure to indicated concentrations of ponatinib for 7 days. Clonogenic potential was analysed by measuring crystal violet absorbance photometrically at 560nm after cell fixation and staining procedure. Statistical significance was calculated using 2way-ANOVA, *p <0.05, **p <0.01, ***p <0.001. Error bars indicate mean ± SD, stars on top of bars indicate the difference between the cell line and respective untreated control whereas stars above lines indicate the difference between the Arg388, Gly388 and GFP variants. B) Impact of ponatinib on spheroid-forming capacity of FGFR4- as compared to GFP- overexpressing cells was analysed by plating the indicated GBM cell subclones in low-attachment plates with NB+ medium. 96 h after seeding, formed neurospheres were exposed to indicated concentrations of ponatinib for 7 days. Photomicrographs were taken with a Nikon Eclipse Ti (10x objective). Scale bars indicate 100 µm.

5. Discussion

Cancer is one of the most serious health problems worldwide, and known to be the second leading cause of death after cardiovascular diseases [2, 11]. The understanding of the development of cancer and, thus, cellular and genetic changes causing this disease are increasing since the beginning of cancer research around 1770 [12]. Transformed neural stem- and progenitor-cell populations are believed to give rise to gliomas, a subgroup of CNS tumors [82, 83].

GBM represents the most common and aggressive adult brain tumor, classified by the WHO as grade IV astrocytoma [106]. GBM are fast growing tumors consisting of a heterogenous cell population and lead to a mean overall patient survival of 14 months under standard therapy. Primary GBM (90% of all GBM cases), are characterized predominantly by an *IDH1* non-mutated genotype in contrast to secondary GBM (10% of all GBM cases) harboring a somatic *IDH1* point mutation leading to an enzymatic gain-of-function [81, 88]. Additionally, primary and secondary GBM are classified by genetic markers such as *TP53, TERT* promoter and *PTEN* mutations, *EGFR* alterations and *MGMT* promoter hyper-methylation [154].

Despite rapid discovery of novel therapeutic targets and development of new anticancer compounds, GBM remains difficult to treat [155]. The anti-VEGF antibody bevacizumab showed positive initial responses, unfortunately followed by a more aggressive GBM relapse in the majority of patients [156]. Main obstacles hindering treatment of GBM are adequate delivery into the brain by passing the blood-brain-barrier and the heterogenous cell population forming these tumors and building the TME [157]. Consequently, novel therapeutic strategies are of high interest and urgently needed in clinical practice.

Previous *in vitro* studies performed in our group at the Institute of Cancer Research in Vienna revealed that endogenous as well as ectopic overexpression of *FGF5* in GBM promotes proliferation and *in vivo* tumor growth [158]. Additional preliminar studies performed by Lötsch *et. al.* (unpublished) pointed out that FGFR4 could play an important role in GBM cell aggressiveness. Hence, introduction of a dnFGFR4 construct into U251MG cells led to reduced proliferation, clone forming capacity as well as impaired 3D-neurosphere formation and *in vivo* xenograft growth. Based on these data, in this thesis work we set out to dissect the role of FGFR4 in

GBM. In more detail, we aimed to investigate the effect on 2D- and 3D-growth after ectopic expression of FGFR4 in HU-MI and U251MG cells *in vitro* as well as *in vivo*.

5.1. Endogenous overexpression of FGFR4 in a subset of primary GBM samples

Several altered signaling pathways in malignant glioma tissue samples were identified by TCGA research network analysis to play major roles during tumor development [159]. One of these pathways was the RTK/RAS/PI3K signalling pathway, responsible for proliferation and survival. EGFR, MET and PDGFRA are well-investigated RTKs, frequently altered in gliomas [109, 159, 160]. Also, for some FGFR variants and FGFR1 in particular, as well as their ligands FGF2 and FGF5, important impacts on GBM cell survival, proliferation and chemoresistance have been suggested [158, 161-163]. In addition, Yamaguchi *et al.* suggested a possible correlation between changes in FGFR2 expression and a shift from FGFR1 splice variant “alpha” to “beta” as important features during malignant astrocytic development [164]. Furthermore, 3-6% of adult GBM are known to harbor a fusion of FGFR genes and transforming acidic coiled-coil domains (FGFR-TACC), discovered in 2012 by [165]. The most common genetic event in that respect is an in-frame fusion of FGFR3 and TACC3 (FGFR3-TACC3), but also FGFR1-TACC1 occurs in a small subset of GBM patients, both generating strong oncogenes [166, 167]. Preliminary clinical phase I studies revealed promising anticancer effects in GBM patients harbouring a FGFR-TACC fusion upon treatment with pan-FGFR inhibitors, pointing out the importance of gaining knowledge about FGFRs and their role in GBM [166].

On the contrary, the role of FGFR4 on the aggressive phenotype of GBM in particular is still poorly understood. However, *Yamada et al.* suggested a correlation of astrocytoma malignant progression and FGFR4 expression, hence predicting dismal prognosis [168]. Previous investigations (Lötsch *et al*, unpublished) on endogenous FGFR4 levels revealed variable FGFR4 mRNA expression in patient-derived GBM primo-cultures. Interestingly, several samples exhibited high FGFR4 expression even similar to the overexpressing hepatocellular carcinoma cell line Hep3B [169]. *In silico* analysis of mRNA expression array data (TCGA GBM project) indicated a distinct cluster of $FGFR4^{high}$ expressing GBM samples belonging to mesenchymal and neural subtypes as described by [109, 148]. Interestingly, mutations of FGFR4 were reported in a small GBM subset of the TCGA GBM project [170]. Further investigation on GBM primo-cell cultures established in our consortium by CGH demonstrated that this

overexpression is not based on *FGFR4* gene amplification. Hence, the molecular factors underlying FGFR4 expression in a defined GBM subgroup are obviously of transcriptional nature but need to be dissected in further experiments. In this thesis project, we focused on the functional role of FGFR4 overexpression as contributor to tumorigenesis in GBM.

Out of an additional subset of GBM primo-cultures and immortalized GBM cell models, BTL1376 and SI-WA were found to endogenously express high FGFR4 mRNA and protein levels in contrast to the other cells included in the panel expressing detectable but low mRNA levels. The FGFR4 expression of the primo-cell line BTL1376 was even comparable to the well-known FGFR4 overexpressing cell line Hep3B [171]. Hence, our data confirmed that FGFR4 was overexpressed in a subgroup of GBM cases. Thus, we were interested whether FGFR4 represents a feasible therapeutic target in this GBM variant.

5.2. Impaired proliferation and 3D-growth capacity upon FGFR4 blockade

Previously, inhibition of FGFRs by small molecule pan-FGFR inhibitors like ponatinib and nintedanib showed promising effects (nM and low µM range, respectively) in several tumor-derived cell lines and solid tumors harbouring gene alterations in *FGFRs* such as lung adenocarcinoma, hepatocellular carcinoma, colon carcinoma, prostate cancer and rhabdomyosarcoma [172-177]. Ponatinib is clinically used in acute myeloid leukaemia (AML) and chronic myeloid leukaemia (CML) patients (BCR-ABL positive), whereas nintedanib is applied in FGFR-overexpressing lung adenocarcinoma patients [178-182]. The intrinsically FGFR4-overexpressing GBM cell lines used in this study showed higher sensitivity towards the small molecule inhibitors ponatinib and nintedanib as compared to their low expressing counterparts. These observations concerned several important hallmarks of tumor aggressiveness including clonogenicity and 3D-neurosphere formation [183, 184]. This suggests enhanced stemness features of GBM cells overexpressing FGFR4. These findings are in line with previous studies on lung cancer samples exhibiting FGFR overexpression on mRNA and protein level and enhanced sensitivity towards pan-FGFR inhibition [176, 185, 186].

Pharmacological FGFR inhibition by ponatinib and nintedanib is not specific to FGFR4 alone, as they are multi-kinase inhibitors. Therefore, further analysis on FGFR4-specific inhibition by genetic approaches was of interest. Targeted suppression by siRNA knock-down or introduction of kinase-dead FGFR4 expression constructs allowed selective FGFR4 downregulation resulting in lower viability and reduced invasive characteristics in HCC cells [187]. Our group members (Lötsch et.al. & Allerstorfer, unpublished) decided to downregulate FGFR4 expression by introduction of a dnFGFR4 adenoviral construct. Upon viral transformation, cells displayed reduced proliferation, clone-forming capacity and impaired 3-D growth. Targeted FGFR4 blockade was performed in U251MG cells, harbouring moderate endogenous FGFR4 mRNA and protein expression levels. Thus, transformation with the dnFGFR4 construct in one of the high expressing primo-cultures is expected to result in even higher impact on proliferation, 2D- and 3D-cultures upon FGFR4 blockade. These experiments are currently ongoing. Further, xenograft experiments revealed that dnFGFR4 expression resulted in impaired tumorigenicity in comparison to the GFP-transformed control. This is an interesting finding, pointing towards a role of even low FGFR4 expression levels as essential contributor to the malignancy of human GBM.

5.3. Modification of FGFR4 expression in FGFR4^{low} GBM cell models

Accordingly, we decided to perform the opposite experiment and test whether ectopic FGFR4 overexpression in FGFR4^{low} cell lines can influence proliferation and survival. FGFR4 alteration by introduction of wild-type FGFR4 into prostate cancer cells with a retroviral expression construct resulting in altered motility and invasiveness has been described previously [125, 188]. In this thesis work, we cloned plasmids coding for full length wild-type FGFR4 variants (Gly388 and Arg388) into a retroviral construct. By application of designed primers, we generated a construct encoding a FGFR4_GFP fusion protein with GFP at the c-terminus of the FGFR4 open reading frame. A variety of studies revealed an association of the Gly388Arg polymorphism within the transmembrane region of the FGFR4 molecule with altered cellular migratory potential and tumor aggressiveness [125, 189, 190]. The Gly388Arg polymorphism, caused by a germline SNP resulting in a change from glycine to arginine at codon 388, is frequently associated with poor prognosis in several cancer types [151, 190, 191].

However, it needs to be mentioned that in case of GBM an impact of this SNP on patient prognosis could not be confirmed so far [190].To address this question, we decided to generate an Arg388 as well as a Gly388 FGFR4 expression construct to investigate the impact on viability, clone formation and 3D-neurosphere growth in GBM cells.

Transfection of HU-MI primo-cells and U251MG immortalized cells with FGFR4_GFP Arg388 and Gly388 expression constructs resulted in efficiently transfected U251MG_FGFR4_Arg_GFP, U251MG_FGFR4_Gly_GFP and HU-MI_FGFR4_Arg_GFP subclones, but unsatisfying numbers of positively transfected HU-MI_FGFR4_Gly_GFP cells. It is conceivable that primo-cultures are more sensitive towards lipofection-based transfection, resulting in a comparably low transfection efficiency of HU-MI cells and lethal outcome in 6 other primo-cell lines emerged during this study. In addition, it is likely that high downstream signalling activation by ectopic overexpression of oncogenic FGFR4 cannot be tolerated by several cell models, leading to transgene-mediated cell death induction or oncogene-mediated senescence [192, 193]

Proliferation rates of the FGFR4-transfected sublines were not altered when compared to the GFP control cell lines. FGFR4 Arg388 as well as Gly388 subcellular localization was found to be predominantly perinuclear in both HU-MI and U251MG transfected sublines. In addition, Western blot analysis confirmed these findings, indicating more protein load in the cytoplasmic fractions as compared to the nuclear fractions. This indicates activation of ectopic FGFR4 probably by endogenous FGF ligands leading to receptor internalization and recycling or degradation [145, 194]. This corresponds well to the previous reports on intrinsic expression of e.g. FGF2 and FGF5 in human GBM [158, 195].

Further, colony forming capacity and 3D-neurosphere growth were significantly enhanced upon FGFR4 transfection in U251MG cells. On the contrary, HU-MI Arg388 transfected cells exhibited clone formation comparable to the GFP control, but were characterized by formation of giant neurospheres. These findings are well in line with the already described impact of FGFR4 overexpression on GBM cell stemness features [161, 196]. Although HU-MI Gly388 clones were characterized by enhanced clone formation, 3D-growth capacity was widely unaltered, probably based on the poor

transfection efficacy. Together, these data correspond well to the ones reported by Gauglhofer *et al.* demonstrating that FGFR4 overexpression induces the capacity for 3D-growth in non-tumorigenic hepatocarcinoma cells [197]. Moreover, FGFR4 stabilisation in prostate cancer cells resulted in enhanced proliferation and anchorage independent growth [198].

5.4. Enhanced migratory potential upon efficient transfection of GBM cells with FGFR4 Arg388 or Gly388 constructs

Characteristics such as enhanced migratory potential and growth aggressiveness in cells harbouring the Arg388 variant have been frequently observed in other types of cancer [189, 190, 199, 200]. Presence of germline Arg388 variant was associated with enhanced prostate cancer cell motility, whereas the Gly388 variant supresses gene expression associated with metastases in breast cancer patients [125, 201]. However, in GBM the role of FGFR4 and the Gly388Arg variant is not well characterized [190] and thus, needs to be urgently investigated.

Migration assays revealed that both HU-MI and U251MG Arg388- and Gly388-transfected cell lines harbored significantly enhanced migratory potential. This indicates that FGFR4 generally has to be considered as GBM cell migration-promoting molecule. Enhanced migration by FGFR4 overexpression has also been described in human HCC [169, 197] and high expression of FGFR4 enhanced tumor growth and metastasis in nasopharyngeal carcinoma [202]. Very recently a paracrine signal loop of cancer-associated fibroblast-derived FGF1 activating ovarian cancer cell migration and invasion has been reported [203].

Despite promotion of GBM cell migration by all FGFR4 isoforms investigated also some significant differences have been observed. In particular, HU-MI Gly388 cells exhibited a slight increase in migration rate compared to the Arg388 cell model, whereas in U251MG Arg388 cells the migratory potential was significantly stronger enhanced as compared to the Gly388 counterpart. This increase in migration was corroborated by scratch assay revealing the most rapid wound closure for the Arg388 cell line in case of the U251MG model and for the Gly388 subline in the HU-MI cells. This strongly suggests that the pro-migratory effects of the investigated FGFR4 variants are depending on the cellular context. In that respect, it has to be considered

that U251MG represents an immortalized GBM cell line while HU-MI is a low-passage primo cell culture, probably still more vulnerable to factors like oncogene-induced senescence or hyperproliferation-induced cell death [204, 205]. Additionally, strong differences between HU-MI sublines in the wound-healing assay may be explained by the difference in transfection, with Gly388 indicating poor transfection efficiency. In addition, when trying to understand the differences between both Arg388 subclones and their respective parental cell lines, the Arg388 transfected cells were characterized by distinct changes in morphology from a glial to more mesenchymal phenotype (data not shown), indicating a glial-to-mesenchymal transition (GMT). This is interesting in the light of the fact that a number of TCGA-derived FGFR4^{high} expressors were gliosarcomas, which exhibit next to the heterogenous GBM cell population also sarcomatoid compartments [206]. Accordingly, induction of EMT has been described in HCC cells by FGF19/FGFR4 signalling [207] and also in colorectal cancer stroma-induced EMT was mediated by FGFR4 activation in the malignant cells [208]. It will be interesting to investigate whether FGFR4 mediated signals are general drivers for inducing a sarcomatoid phenotype in astrocytic brain tumors.

5.5. Sensitivity of FGFR4-transfected GBM cell lines towards FGFR inhibition

A possible increase in sensitivity of HU-MI and U251MG transfected cell lines towards FGFR inhibition compared to the parental cell lines was analysed. Both HU-MI and U251MG FGFR4-transfected sublines did not show induced sensitivity towards ponatinib in short term cell viability assays (data not shown). This is not surprising considering the fact that also the proliferation rate of the FGFR4-transfected cell clones was not enhanced. This indicates that FGFR4 transfection did not lead to dependency of the derived cell clones regarding cell proliferation. However this does not preclude that the ectopic introduction of an additional oncogenic transgene does not lead to alterations in other cell biological characteristics. Consequently, FGFR4 overexpression would not per se influence the sensitivity towards inhibitors of this specific transgene in short term cell proliferation assays. Another probable factor keeping the cells less sensitive towards FGFR inhibition upon long term selection might be the activation of Met, helping the cells to bypass FGFR dependency [209, 210]. As mentioned by Kim *et.al. 2015*, the RTK Met and FGFRs crosstalk in their signaling pathways, resulting in drug resistance [210]. Inhibition of Met and suppression of

FGFRs have been described to result in a synthetic lethal phenotype in gastric adenocarcinoma [210]. It is of high interest to test this in future experiments.

In sharp contrast, clonogenicity and anchorage-independent growth were massively influenced by FGFR4 overexpression. Accordingly, hypersensitivity of the FGFR4-transfected clones towards the investigated small molecule FGFR inhibitor ponatinib was observed. This again proves the direct involvement of the FGFR4 transgene in mediating enhanced GBM cell aggressiveness based on cancer stem cell features. Interestingly, like normal stem cells, also cancer stem cells are known to be highly chemoresistant based on the overexpression of multiple protection mechanism [211, 212]. Accordingly, FGFR4 has been frequently linked to cancer chemoresistance phenotypes like for example in case of breast cancer towards doxorubicin [213] and for hepatocellular carcinoma against ER-stress induction based on an FGFR4-GSK3ß-Nrf2 signalling axis [214]. Even resistance of colon cancer cells towards radiation [215] and against the multi-targeted anticancer compound sorafenib of hepatoma cells [216] have been demonstrated to be based on FGFR4. Hence, the question arises whether FGFR4 might also be a molecular factor underlying the strong treatment resistance of human GBMs, especially with respect to radiation and the alkylating substance TMZ used as the standard therapy of this highly malignant brain tumor entity.

6. Conclusion & outlook

In summary, the aim of this study was to dissect the role of FGFR4 in GBM aggressiveness. Transfection of GBM cells with FGFR4 Arg388 and Gly388 constructs promoted several oncogenic features including clone formation, anchorage independent growth and cancer cell migration. Significant differences have been observed with respect to the investigated SNP variants, however, were cell background-dependent. To dig deeper into these topics, currently the migratory and 3D-growth characteristics of the established FGFR4 GBM models are further addressed by using soft-agar and methylcellulose 3D-growth tests *in vitro* and xenograft experiments *in vivo*. Furthermore, to asses the morphologic changes indicating GMT, migratory markers will be analyzed in Western blot analysis and on mRNA expression level. After termination of the *in vivo* experiment, tumors will be processed for immunohistochemical analysis and the differences between the U251MG Arg388 and Gly388 tumors with focus on proliferation (Ki-76), stem cell markers (i.e. nestin) and eventually enhanced migratory potential (vimentin/cadherin) will be investigated. To uncover if FGFR4 may depict a novel therapeutic target in combination with already applied therapeutics, the crosstalk between FGFRs and other RTKs such as Met, has to be investigated in more detail. Moreover, the impact of ectopic FGFR4 expression on chemo- and radiation- sensitivity will be established. In summary, FGFR4 supports an aggressive GBM cell phenotype and might represent a feasible target especially for combination therapy settings in the frame of precision neuro oncology.

7. Abstract

Glioblastoma multiforme (GBM) is a high-grade astrocytoma and accounts for 45-55% of all malignant gliomas in adults. GBM represents the most aggressive primary brain tumor and survival rates are very low with a median overall survival of 14 months under treatment and a 5-year survival of only 5.5%. A heterogenous cell population, high vascularization and pseudopalisading necrosis are the main histopathological characteristics typifying GBM tumor tissue. Molecular features such as *isocitrate dehydrogenase 1/2 (IDH 1/2)* mutations, *telomerase reverse transcriptase (TERT)* promoter mutations, *O^6-methylguanine DNA methyltransferase (MGMT)* promoter methylation and *epidermal growth factor receptor (EGFR)* amplification are parameters used in for the diagnosis of GBM. Despite intensive research, GBM-specific biomarkers -to develop targeted therapies- are still not identified and therefore GBM remains complicated to treat. Previous studies performed in our group revealed the influence of fibroblast growth factors (FGFs) on GBM proliferation and tumor growth *in vivo*. In the present study, we aimed to dissect the role of both FGF receptor tyrosine kinase 4 (FGFR4) Arg388 and Gly388 single nucleotide polymorphism (SNP) variants on GBM growth aggressiveness, 3D-neurosphere formation and migration.

To do so, we transfected two FGFR4 low expressing GBM cell lines, the primary GBM cell line U251MG and the GBM primo-culture HU-MI, to ectopically over-express both FGFR4 Arg388 and Gly388 SNP variants. All cell models were analyzed on their colony forming capacity, 3D-neurosphere growth and migratory potential in relation to GFP transfected controls. Upon transfection with both FGFR4 Arg388 and Gly388 constructs, distinct pro-migratory effects were visible in U251MG cells in contrast to HU-MI transfected cells. Additionally, colony formation and 3D-growth were significantly enhanced in U251MG FGFR4 Arg388 and Gly388 cell models and HU-MI FGFR4 Arg388. Introduction of FGFR4 Gly388 into the HU-MI cell model was not efficient enough to obtain results strongly differing from the parental cell line.

Summarizing, ectopic expression of FGFR4 Arg388 or Gly388 in U251MG resulted in enhanced migration, 3D-growth and clone formation. To analyze the role of FGFR4 in these processes into more detail, further biological and molecular analyses with focus on migratory markers are of high interest. Additionally, altered tumorigenicity of the U251MG FGFR4 transfected sublines requires examination in *in vivo* xenograft

models. In conclusion, these data suggest a prominent role of FGFR4 in GBM migratory and proliferative characteristics as well as 3D-neurosphere formation and clonogenicity.

8. Zusammenfassung

Mit 45-55% aller malignen Gliomen ist das Glioblastom (GBM) der häufigste Tumor des zentralen Nervensystems (ZNS) in Erwachsenen. Das GBM ist der aggressivste primäre Gehirntumor und gehört zur Gruppe der hochgradigen Astrozytome, welche sich durch eine besonders niedrige Überlebenszeit von 14 Monaten auszeichnet. Besonders charakteristisch für das GBM sind seine heterogene Zellpopulation, starke Vaskularisierung und strichförmige Nekrosen, welche die wichtigsten histo- pathologischen Merkmale des Tumors darstellen. In Bezug auf die molekular-diagnostischen Eigenschaften dieser Entität sind besonders Mutationen in den Genen der *Isozitrat-Dehydrogenase 1/2 (IDH1/2)*, des *Telomerase reverse Transkriptase (TERT)* Promoters, des *O^6-Methylguanin Methyltransferase (MGMT)* Promoters und Amplifikationen des *epidermalen Wachstumsfakor-Rezeptor (EGFR)* Gens nennenswert. Trotz intensiver Forschung im Bereich der zielgerichteten Krebstherapie, wurden bisher keine GBM-spezifischen Biomarker identifiziert und auch die zuvor genannten molekularen Marker konnten nicht dafür genutzt werden.

Frühere Beobachtungen in unsere Arbeitsgruppe ergaben gesteigerte Zellproliferation und Tumorwachstum *in vivo* welche stark von fibroblastischen Wachstumsfaktoren (FGFs) beeinflusst wurden. Basierend auf diesen vorherigen Ergebnissen konzentriert sich diese Studie auf FGF Rezeptor 4 (FGFR4), die Unterschiede zwischen seinen Varianten (Arg388 und Gly388), und dessen Rolle in GBM -Wachstum, -Aggressivität, -migration und 3D-Wachstum *in vitro*.

Um FGFR4 in FGFR4 niedrig exprimierende GBM Zelllinien über zu exprimieren, wurden U251MG und HU-MI mit FGFR4 Arg388 oder Gly388 Expressionsvektoren transfiziert. Klonformation, 3D-Wachstum, und Migrationspotential wurden in den transfizierten Zellmodellen untersucht. FGFR4 Arg388 und Gly388 Überexprimierung hat induzierte Migration in U251MG zur Folge. Dieser Effekt konnte jedoch nicht in transfizierten HU-MI Zellen nachgewiesen werden. Bemerkenswerterweise zeigen alle transfizierten Zellmodelle außer HU-MI FGFR4 Gly388 gesteigertes Klon- und 3D-wachstum.

Zusammenfassend ist wichtig zu erwähnen, dass induzierte FGFR4 (Arg388 und Gly388) Expression in U251MG zu verstärkter Migration, Klon- und 3D-Wachstum führt. Weiterführend wird die Funktion von FGFR4 noch *in vivo* untersucht werden.

9. References

1. Ornitz, D.M. and N. Itoh, *The Fibroblast Growth Factor signaling pathway.* Wiley Interdiscip Rev Dev Biol, 2015. **4**(3): p. 215-66.
2. World Health Organization, W., *Top 10 causes of death worldwide.* Updated January 2017.
3. Wells, J.C.K., et al., *Evolutionary public health: introducing the concept.* Lancet, 2017. **390**(10093): p. 500-509.
4. Ferlay, J., et al., *Cancer incidence and mortality patterns in Europe: estimates for 40 countries in 2012.* Eur J Cancer, 2013. **49**(6): p. 1374-403.
5. *Conquering cancer.* Lancet, 2013. **382**(9910): p. 2039.
6. Anand, P., et al., *Cancer is a preventable disease that requires major lifestyle changes.* Pharm Res, 2008. **25**(9): p. 2097-116.
7. Organization, W.H., *Noncommunicable diseases country profiles 2014.* WHO Document Production Services, Geneva, Switzerland, 2014.
8. Gostin, L.O., et al., *Legal priorities for prevention of non-communicable diseases: innovations from WHO's Eastern Mediterranean region.* Public Health, 2017. **144**: p. 4-12.
9. Kennedy, P.T.F., et al., *Immune Tolerant Chronic Hepatitis B: The Unrecognized Risks.* Viruses, 2017. **9**(5).
10. Stoner, P., T. Ghaffaripour, and D. Cohen, *Aggressive large-cell neuroendocrine carcinoma of the sigmoid colon in a patient with ulcerative colitis.* BMJ Case Rep, 2017. **2017**.
11. National Cancer Institute, N., *What is cancer, cancer types.* Understanding about cancer, Updated January, 2015.
12. National Cancer Institute, N., *Milestones in Cancer Research & Discovery.*
13. Weinberg, R.A., *Coming full circle-from endless complexity to simplicity and back again.* Cell, 2014. **157**(1): p. 267-71.
14. Lin, L.F., et al., *P-glycoprotein attenuates DNA repair activity in multidrug-resistant cells by acting through the Cbp-Csk-Src cascade.* Oncotarget, 2017. **8**(28): p. 45072-45087.
15. Shih, C., et al., *Passage of phenotypes of chemically transformed cells via transfection of DNA and chromatin.* Proc Natl Acad Sci U S A, 1979. **76**(11): p. 5714-8.
16. R.A., W., *The biology of cancer* Garland science, 2013. **Eight edition**.
17. Tessmer, M.S. and K.C. Anderson, *AACR Cancer Progress Report 2016: Improving Lives Through Research.* Clin Cancer Res, 2016. **22**(19): p. 4759.
18. Fakhri, B. and K.H. Lim, *Molecular landscape and sub-classification of gastrointestinal cancers: a review of literature.* J Gastrointest Oncol, 2017. **8**(3): p. 379-386.
19. Yates, L.R. and P.J. Campbell, *Evolution of the cancer genome.* Nat Rev Genet, 2012. **13**(11): p. 795-806.
20. Lu, H., W. Ouyang, and C. Huang, *Inflammation, a key event in cancer development.* Mol Cancer Res, 2006. **4**(4): p. 221-33.
21. Cooper, G.M., *The cell, a molecular approach.* Boston University:Sunderland, 2000. **2nd**.
22. Vincent, T.L. and R.A. Gatenby, *An evolutionary model for initiation, promotion, and progression in carcinogenesis.* Int J Oncol, 2008. **32**(4): p. 729-37.

23. Lorne J. Hofseth, P.e.A.W., PhD equation Curtis C. Harris, MD, *Chemical Carcinogenesis.* Fastest Oncology & Hematology Insight Engine, 2017.
24. Institute, N.C., *Defining Cancer.* Retrieved 10 June 2014.
25. Chaffer, C.L. and R.A. Weinberg, *How does multistep tumorigenesis really proceed?* Cancer Discov, 2015. **5**(1): p. 22-4.
26. Alexandrov, L.B., et al., *Signatures of mutational processes in human cancer.* Nature, 2013. **500**(7463): p. 415-21.
27. Hanahan, D. and R.A. Weinberg, *Hallmarks of cancer: the next generation.* Cell, 2011. **144**(5): p. 646-74.
28. Tan, S., et al., *Crystal clear: visualizing the intervention mechanism of the PD-1/PD-L1 interaction by two cancer therapeutic monoclonal antibodies.* Protein Cell, 2016. **7**(12): p. 866-877.
29. Hanahan, D. and R.A. Weinberg, *The hallmarks of cancer.* Cell, 2000. **100**(1): p. 57-70.
30. Fouad, Y.A. and C. Aanei, *Revisiting the hallmarks of cancer.* Am J Cancer Res, 2017. **7**(5): p. 1016-1036.
31. Boss, M.K., R. Bristow, and M.W. Dewhirst, *Linking the history of radiation biology to the hallmarks of cancer.* Radiat Res, 2014. **181**(6): p. 561-77.
32. Folkman, J., *Tumor angiogenesis: therapeutic implications.* N Engl J Med, 1971. **285**(21): p. 1182-6.
33. Sabapathy, K. and D.P. Lane, *Therapeutic targeting of p53: all mutants are equal, but some mutants are more equal than others.* Nat Rev Clin Oncol, 2017.
34. Merkel, O., et al., *When the guardian sleeps: Reactivation of the p53 pathway in cancer.* Mutat Res, 2017. **773**: p. 1-13.
35. Sherr, C.J. and F. McCormick, *The RB and p53 pathways in cancer.* Cancer Cell, 2002. **2**(2): p. 103-12.
36. Ferrara, N., *Vascular endothelial growth factor.* Arterioscler Thromb Vasc Biol, 2009. **29**(6): p. 789-91.
37. Bandyopadhyay, D., *Farmer to pharmacist: curcumin as an anti-invasive and antimetastatic agent for the treatment of cancer.* Front Chem, 2014. **2**: p. 113.
38. Melzer, C., J. von der Ohe, and R. Hass, *Breast Carcinoma: From Initial Tumor Cell Detachment to Settlement at Secondary Sites.* Biomed Res Int, 2017. **2017**: p. 8534371.
39. Klymkowsky, M.W. and P. Savagner, *Epithelial-mesenchymal transition: a cancer researcher's conceptual friend and foe.* Am J Pathol, 2009. **174**(5): p. 1588-93.
40. Gatenby, R.A. and R.J. Gillies, *Why do cancers have high aerobic glycolysis?* Nat Rev Cancer, 2004. **4**(11): p. 891-9.
41. Weinberg, R.A., *The biology of cancer*. Second edition. ed. 2014, New York: Garland Science, Taylor & Francis Group. xx, 876, A 6, G 30, I 28 pages.
42. Balkwill, F.R., M. Capasso, and T. Hagemann, *The tumor microenvironment at a glance.* J Cell Sci, 2012. **125**(Pt 23): p. 5591-6.
43. Hanahan, D. and L.M. Coussens, *Accessories to the crime: functions of cells recruited to the tumor microenvironment.* Cancer Cell, 2012. **21**(3): p. 309-22.
44. Dang, C.V., et al., *Drugging the 'undruggable' cancer targets.* Nat Rev Cancer, 2017. **17**(8): p. 502-508.
45. Holland JF, F.E., Bast RC, Kufe DW, Pollok RE, Weichselbaum RR, *Cancer Medicine 7*. 2006: Hamilton: BC Decker.

46. Mezhir, J.J., et al., *Ionizing radiation: a genetic switch for cancer therapy.* Cancer Gene Ther, 2006. **13**(1): p. 1-6.
47. Goodman Gilman A, H.J., Limbird LE, *The pharmacological basis of therapeutics*. 10th ed. 2001, New York: McGraw-Hill.
48. Li, Y., et al., *A Mini-Review for Cancer Immunotherapy: Molecular Understanding of PD-1/PD-L1 Pathway & Translational Blockade of Immune Checkpoints.* Int J Mol Sci, 2016. **17**(7).
49. Artal Cortes, A., L. Calera Urquizu, and J. Hernando Cubero, *Adjuvant chemotherapy in non-small cell lung cancer: state-of-the-art.* Transl Lung Cancer Res, 2015. **4**(2): p. 191-7.
50. Airley, R., *Cancer chemotherapy*. 2009, Chichester, UK ; Hoboken, NJ: Wiley-Blackwell. x, 341 p., 8 p. of plates.
51. Miller, K.D., et al., *Cancer treatment and survivorship statistics, 2016.* CA Cancer J Clin, 2016. **66**(4): p. 271-89.
52. Moser, E.C. and F. Meunier, *Cancer survivorship: A positive side-effect of more successful cancer treatment.* EJC Suppl, 2014. **12**(1): p. 1-4.
53. Kimberly Miller, M., M. Rebecca Siegel, and D. Ahmedin Jemal, PhD, *Cancer Treatment & Survivorship Facts & Figures 2016-2017.* Atlanta American Cancer Society, 2016: p. 41.
54. Verweij, J. and H.M. Pinedo, *Mitomycin C: mechanism of action, usefulness and limitations.* Anticancer Drugs, 1990. **1**(1): p. 5-13.
55. Kelland, L., *The resurgence of platinum-based cancer chemotherapy.* Nat Rev Cancer, 2007. **7**(8): p. 573-84.
56. Westerink, N.L., et al., *Cancer treatment induced metabolic syndrome: Improving outcome with lifestyle.* Crit Rev Oncol Hematol, 2016. **108**: p. 128-136.
57. Chueh, H.W. and J.H. Yoo, *Metabolic syndrome induced by anticancer treatment in childhood cancer survivors.* Ann Pediatr Endocrinol Metab, 2017. **22**(2): p. 82-89.
58. Thind, K., et al., *Immunotherapy in pancreatic cancer treatment: a new frontier.* Therap Adv Gastroenterol, 2017. **10**(1): p. 168-194.
59. Pardoll, D.M., *The blockade of immune checkpoints in cancer immunotherapy.* Nat Rev Cancer, 2012. **12**(4): p. 252-64.
60. Wang, X., et al., *The application and mechanism of PD pathway blockade for cancer therapy.* Postgrad Med J, 2017.
61. Rasche, L., et al., *Immunologic approaches for the treatment of multiple myeloma.* Cancer Treat Rev, 2017. **55**: p. 190-199.
62. Xu, J.X., et al., *FDA Approval Summary: Nivolumab in Advanced Renal Cell Carcinoma After Anti-Angiogenic Therapy and Exploratory Predictive Biomarker Analysis.* Oncologist, 2017. **22**(3): p. 311-317.
63. Goodman, A., S.P. Patel, and R. Kurzrock, *PD-1-PD-L1 immune-checkpoint blockade in B-cell lymphomas.* Nat Rev Clin Oncol, 2017. **14**(4): p. 203-220.
64. Gotwals, P., et al., *Prospects for combining targeted and conventional cancer therapy with immunotherapy.* Nat Rev Cancer, 2017. **17**(5): p. 286-301.
65. Avendaño, C. and J.C. Menéndez, *Medicinal chemistry of anticancer drugs*. 1st ed. 2008, Amsterdam ; Boston: Elsevier. xv, 442 p.
66. Moyer, J.D., et al., *Induction of apoptosis and cell cycle arrest by CP-358,774, an inhibitor of epidermal growth factor receptor tyrosine kinase.* Cancer Res, 1997. **57**(21): p. 4838-48.

67. Lippert, T.H., H.J. Ruoff, and M. Volm, *Current status of methods to assess cancer drug resistance.* Int J Med Sci, 2011. **8**(3): p. 245-53.
68. Lavi, O., M.M. Gottesman, and D. Levy, *The dynamics of drug resistance: a mathematical perspective.* Drug Resist Updat, 2012. **15**(1-2): p. 90-7.
69. Heffeter, P., et al., *Impact of terminal dimethylation on the resistance profile of alpha-N-heterocyclic thiosemicarbazones.* Biochem Pharmacol, 2012. **83**(12): p. 1623-33.
70. Cheng, L., et al., *FUT family mediates the multidrug resistance of human hepatocellular carcinoma via the PI3K/Akt signaling pathway.* Cell Death Dis, 2013. **4**: p. e923.
71. Sousa, A.M.M., et al., *Evolution of the Human Nervous System Function, Structure, and Development.* Cell, 2017. **170**(2): p. 226-247.
72. Faa, G., et al., *Fetal programming of neuropsychiatric disorders.* Birth Defects Res C Embryo Today, 2016. **108**(3): p. 207-223.
73. Forni, P.E. and S. Wray, *Neural crest and olfactory system: new prospective.* Mol Neurobiol, 2012. **46**(2): p. 349-60.
74. Gilbert, S., *Developmental Biology.* 6th edition ed. 2000, Sunderland MA.: Sinauer Associates.
75. Sadler, T.W.T.W., *Langman's medical embryology.* Philadelphia : Wolters Kluwer Lippincott Williams & Wilkins, c2010.

: United States.
76. resource, O.e., *Anatomy and Physiology*. Vol. 2.
77. Pansky, B., *Review of medical embryology*. 1982, United States: New York : Macmillan, c1982.
78. Peitgen, N. and P. Papanagiotou, *[Intra-axial brain tumors in adults : On the basis of the 2016 WHO classification].* Radiologe, 2017.
79. Carlsson, S.K., S.P. Brothers, and C. Wahlestedt, *Emerging treatment strategies for glioblastoma multiforme.* EMBO Mol Med, 2014. **6**(11): p. 1359-70.
80. Antonios, J.P., et al., *Detection of immune responses after immunotherapy in glioblastoma using PET and MRI.* Proc Natl Acad Sci U S A, 2017.
81. Louis, D.N., et al., *The 2016 World Health Organization Classification of Tumors of the Central Nervous System: a summary.* Acta Neuropathol, 2016. **131**(6): p. 803-20.
82. Miranda, A., et al., *Breaching barriers in glioblastoma. Part I: Molecular pathways and novel treatment approaches.* Int J Pharm, 2017.
83. Auffinger, B., et al., *The role of glioma stem cells in chemotherapy resistance and glioblastoma multiforme recurrence.* Expert Rev Neurother, 2015. **15**(7): p. 741-52.
84. Seymour, T., A. Nowak, and F. Kakulas, *Targeting Aggressive Cancer Stem Cells in Glioblastoma.* Front Oncol, 2015. **5**: p. 159.
85. Kim, S.S., et al., *Effective treatment of glioblastoma requires crossing the blood-brain barrier and targeting tumors including cancer stem cells: The promise of nanomedicine.* Biochem Biophys Res Commun, 2015. **468**(3): p. 485-9.
86. Hu, B., et al., *Epigenetic Activation of WNT5A Drives Glioblastoma Stem Cell Differentiation and Invasive Growth.* Cell, 2016. **167**(5): p. 1281-1295 e18.
87. Crespo, I., et al., *Molecular and Genomic Alterations in Glioblastoma Multiforme.* Am J Pathol, 2015. **185**(7): p. 1820-33.

88. Preusser, M., et al., *Prospects of immune checkpoint modulators in the treatment of glioblastoma.* Nat Rev Neurol, 2015. **11**(9): p. 504-14.
89. Cohen, A.L., S.L. Holmen, and H. Colman, *IDH1 and IDH2 mutations in gliomas.* Curr Neurol Neurosci Rep, 2013. **13**(5): p. 345.
90. Akyerli, C.B., et al., *Use of telomerase promoter mutations to mark specific molecular subsets with reciprocal clinical behavior in IDH mutant and IDH wild-type diffuse gliomas.* J Neurosurg, 2017: p. 1-13.
91. Spiegl-Kreinecker, S., et al., *Prognostic quality of activating TERT promoter mutations in glioblastoma: interaction with the rs2853669 polymorphism and patient age at diagnosis.* Neuro Oncol, 2015. **17**(9): p. 1231-40.
92. Stetson, L.C., J.E. Dazard, and J.S. Barnholtz-Sloan, *Protein Markers Predict Survival in Glioma Patients.* Mol Cell Proteomics, 2016. **15**(7): p. 2356-65.
93. Aldape, K., et al., *Glioblastoma: pathology, molecular mechanisms and markers.* Acta Neuropathol, 2015. **129**(6): p. 829-48.
94. Paulitschke, V., et al., *Vemurafenib resistance signature by proteome analysis offers new strategies and rational therapeutic concepts.* Mol Cancer Ther, 2015. **14**(3): p. 757-68.
95. Jacinto, F.V. and M. Esteller, *MGMT hypermethylation: a prognostic foe, a predictive friend.* DNA Repair (Amst), 2007. **6**(8): p. 1155-60.
96. Sturm, D., et al., *Hotspot mutations in H3F3A and IDH1 define distinct epigenetic and biological subgroups of glioblastoma.* Cancer Cell, 2012. **22**(4): p. 425-37.
97. Dang, L., et al., *Cancer-associated IDH1 mutations produce 2-hydroxyglutarate.* Nature, 2009. **462**(7274): p. 739-44.
98. Ahmed, A.U., B. Auffinger, and M.S. Lesniak, *Understanding glioma stem cells: rationale, clinical relevance and therapeutic strategies.* Expert Rev Neurother, 2013. **13**(5): p. 545-55.
99. Taylor, J.W. and D. Schiff, *Treatment considerations for MGMT-unmethylated glioblastoma.* Curr Neurol Neurosci Rep, 2015. **15**(1): p. 507.
100. Aparicio, S. and C. Caldas, *The implications of clonal genome evolution for cancer medicine.* N Engl J Med, 2013. **368**(9): p. 842-51.
101. Nicholas, M.K., et al., *Molecular heterogeneity in glioblastoma: therapeutic opportunities and challenges.* Semin Oncol, 2011. **38**(2): p. 243-53.
102. Alberts, B., J.H. Wilson, and T. Hunt, *Molecular biology of the cell*. 5th ed. 2008, New York: Garland Science. xxxiii, 1601, 90 p.
103. Katoh, M., *Therapeutics Targeting FGF Signaling Network in Human Diseases.* Trends Pharmacol Sci, 2016. **37**(12): p. 1081-1096.
104. Spangle, J.M. and T.M. Roberts, *Epigenetic regulation of RTK signaling.* J Mol Med (Berl), 2017. **95**(8): p. 791-798.
105. Katoh, M. and H. Nakagama, *FGF receptors: cancer biology and therapeutics.* Med Res Rev, 2014. **34**(2): p. 280-300.
106. Cancer Genome Atlas Research, N., *Comprehensive genomic characterization defines human glioblastoma genes and core pathways.* Nature, 2008. **455**(7216): p. 1061-8.
107. Zheng, H., et al., *p53 and Pten control neural and glioma stem/progenitor cell renewal and differentiation.* Nature, 2008. **455**(7216): p. 1129-33.
108. Stommel, J.M., et al., *Coactivation of receptor tyrosine kinases affects the response of tumor cells to targeted therapies.* Science, 2007. **318**(5848): p. 287-90.

109. Ceccarelli, M., et al., *Molecular Profiling Reveals Biologically Discrete Subsets and Pathways of Progression in Diffuse Glioma.* Cell, 2016. **164**(3): p. 550-63.
110. Chae, Y.K., et al., *Inhibition of the fibroblast growth factor receptor (FGFR) pathway: the current landscape and barriers to clinical application.* Oncotarget, 2017. **8**(9): p. 16052-16074.
111. Heinzle, C., et al., *Is fibroblast growth factor receptor 4 a suitable target of cancer therapy?* Curr Pharm Des, 2014. **20**(17): p. 2881-98.
112. Beenken, A. and M. Mohammadi, *The FGF family: biology, pathophysiology and therapy.* Nat Rev Drug Discov, 2009. **8**(3): p. 235-53.
113. Mohammadi, M., S.K. Olsen, and O.A. Ibrahimi, *Structural basis for fibroblast growth factor receptor activation.* Cytokine Growth Factor Rev, 2005. **16**(2): p. 107-37.
114. Consortium, A., *Autosomal dominant hypophosphataemic rickets is associated with mutations in FGF23.* Nat Genet, 2000. **26**(3): p. 345-8.
115. Eswarakumar, V.P., I. Lax, and J. Schlessinger, *Cellular signaling by fibroblast growth factor receptors.* Cytokine Growth Factor Rev, 2005. **16**(2): p. 139-49.
116. Johnson, D.E. and L.T. Williams, *Structural and functional diversity in the FGF receptor multigene family.* Adv Cancer Res, 1993. **60**: p. 1-41.
117. Johnson, D.E., et al., *The human fibroblast growth factor receptor genes: a common structural arrangement underlies the mechanisms for generating receptor forms that differ in their third immunoglobulin domain.* Mol Cell Biol, 1991. **11**(9): p. 4627-34.
118. Wang, F., et al., *Alternately spliced NH2-terminal immunoglobulin-like Loop I in the ectodomain of the fibroblast growth factor (FGF) receptor 1 lowers affinity for both heparin and FGF-1.* J Biol Chem, 1995. **270**(17): p. 10231-5.
119. Hacker, U., K. Nybakken, and N. Perrimon, *Heparan sulphate proteoglycans: the sweet side of development.* Nat Rev Mol Cell Biol, 2005. **6**(7): p. 530-41.
120. Ibrahimi, O.A., et al., *Structural basis for fibroblast growth factor receptor 2 activation in Apert syndrome.* Proc Natl Acad Sci U S A, 2001. **98**(13): p. 7182-7.
121. Turner, N. and R. Grose, *Fibroblast growth factor signalling: from development to cancer.* Nat Rev Cancer, 2010. **10**(2): p. 116-29.
122. Antoniou, A.C., et al., *Common breast cancer-predisposition alleles are associated with breast cancer risk in BRCA1 and BRCA2 mutation carriers.* Am J Hum Genet, 2008. **82**(4): p. 937-48.
123. Dutt, A., et al., *Drug-sensitive FGFR2 mutations in endometrial carcinoma.* Proc Natl Acad Sci U S A, 2008. **105**(25): p. 8713-7.
124. Pollock, P.M., et al., *Frequent activating FGFR2 mutations in endometrial carcinomas parallel germline mutations associated with craniosynostosis and skeletal dysplasia syndromes.* Oncogene, 2007. **26**(50): p. 7158-62.
125. Wang, J., D.W. Stockton, and M. Ittmann, *The fibroblast growth factor receptor-4 Arg388 allele is associated with prostate cancer initiation and progression.* Clin Cancer Res, 2004. **10**(18 Pt 1): p. 6169-78.
126. Coleman, S.J., et al., *The ins and outs of fibroblast growth factor receptor signalling.* Clin Sci (Lond), 2014. **127**(4): p. 217-31.
127. Basilico, C. and D. Moscatelli, *The FGF family of growth factors and oncogenes.* Adv Cancer Res, 1992. **59**: p. 115-65.
128. Boilly, B., et al., *FGF signals for cell proliferation and migration through different pathways.* Cytokine Growth Factor Rev, 2000. **11**(4): p. 295-302.

129. Citores, L., et al., *Fibroblast growth factor receptor-induced phosphorylation of STAT1 at the Golgi apparatus without translocation to the nucleus.* J Cell Physiol, 2007. **212**(1): p. 148-56.
130. Chen, Y., et al., *Fibroblast growth factor (FGF) signaling through PI 3-kinase and Akt/PKB is required for embryoid body differentiation.* Oncogene, 2000. **19**(33): p. 3750-6.
131. Doherty, P. and F.S. Walsh, *CAM-FGF Receptor Interactions: A Model for Axonal Growth.* Mol Cell Neurosci, 1996. **8**(2/3): p. 99-111.
132. Hall, H., et al., *Inhibition of FGF-stimulated phosphatidylinositol hydrolysis and neurite outgrowth by a cell-membrane permeable phosphopeptide.* Curr Biol, 1996. **6**(5): p. 580-7.
133. Hart, K.C., et al., *Transformation and Stat activation by derivatives of FGFR1, FGFR3, and FGFR4.* Oncogene, 2000. **19**(29): p. 3309-20.
134. Touat, M., et al., *Targeting FGFR Signaling in Cancer.* Clin Cancer Res, 2015. **21**(12): p. 2684-94.
135. Jaakkola, J., et al., *Radiographic grading of extrinsic allergic alveolitis. A comparison between a modified ILO classification and a descriptive method.* Acta Radiol, 1991. **32**(6): p. 461-6.
136. Triantis, V., et al., *Glycosylation of fibroblast growth factor receptor 4 is a key regulator of fibroblast growth factor 19-mediated down-regulation of cytochrome P450 7A1.* Hepatology, 2010. **52**(2): p. 656-66.
137. Rokita, H., M. Mackiewicz, and A. Koj, *Acute phase response to recombinant interleukin-6 and macrophage- and fibroblast-derived crude cytokine preparations in primary cultures of mouse hepatocytes.* Cell Biochem Funct, 1989. **7**(4): p. 257-62.
138. Desnoyers, L.R., et al., *Targeting FGF19 inhibits tumor growth in colon cancer xenograft and FGF19 transgenic hepatocellular carcinoma models.* Oncogene, 2008. **27**(1): p. 85-97.
139. Dethlefsen, C., et al., *Exercise-Induced Catecholamines Activate the Hippo Tumor Suppressor Pathway to Reduce Risks of Breast Cancer Development.* Cancer Res, 2017.
140. Riss, T.L., et al., *Cell Viability Assays*, in *Assay Guidance Manual*, G.S. Sittampalam, et al., Editors. 2004: Bethesda (MD).
141. Rafehi, H., et al., *Clonogenic assay: adherent cells.* J Vis Exp, 2011(49).
142. Su, G., et al., *The effect of forced growth of cells into 3D spheres using low attachment surfaces on the acquisition of stemness properties.* Biomaterials, 2013. **34**(13): p. 3215-22.
143. Falvella, F.S., et al., *FGFR4 Gly388Arg polymorphism may affect the clinical stage of patients with lung cancer by modulating the transcriptional profile of normal lung.* Int J Cancer, 2009. **124**(12): p. 2880-5.
144. Sahadevan, K., et al., *Selective over-expression of fibroblast growth factor receptors 1 and 4 in clinical prostate cancer.* J Pathol, 2007. **213**(1): p. 82-90.
145. Haugsten, E.M., et al., *Proximity Labeling Reveals Molecular Determinants of FGFR4 Endosomal Transport.* J Proteome Res, 2016. **15**(10): p. 3841-3855.
146. Heinzle, C., et al., *Differential effects of polymorphic alleles of FGF receptor 4 on colon cancer growth and metastasis.* Cancer Res, 2012. **72**(22): p. 5767-77.
147. Ulaganathan, V.K., et al., *Germline variant FGFR4 p.G388R exposes a membrane-proximal STAT3 binding site.* Nature, 2015. **528**(7583): p. 570-4.

148. Brennan, C.W., et al., *The somatic genomic landscape of glioblastoma.* Cell, 2013. **155**(2): p. 462-77.
149. Ipenburg, N.A., et al., *Fibroblast Growth Factor Receptor Family Members as Prognostic Biomarkers in Head and Neck Squamous Cell Carcinoma: A Systematic Review.* Target Oncol, 2016. **11**(1): p. 17-27.
150. Shen, Y.Y., et al., *Fibroblast growth factor receptor 4 Gly388Arg polymorphism in Chinese gastric cancer patients.* World J Gastroenterol, 2013. **19**(28): p. 4568-75.
151. Ezzat, S., et al., *FGFR4 polymorphic alleles modulate mitochondrial respiration: A novel target for somatostatin analog action in pituitary tumors.* Oncotarget, 2017. **8**(2): p. 3481-3494.
152. Koole, K., et al., *FGFR4 Is a Potential Predictive Biomarker in Oral and Oropharyngeal Squamous Cell Carcinoma.* Pathobiology, 2015. **82**(6): p. 280-9.
153. Auciello, G., et al., *Regulation of fibroblast growth factor receptor signalling and trafficking by Src and Eps8.* J Cell Sci, 2013. **126**(Pt 2): p. 613-24.
154. Kim, J., et al., *Spatiotemporal Evolution of the Primary Glioblastoma Genome.* Cancer Cell, 2015. **28**(3): p. 318-28.
155. Lozada-Delgado, E.L., N. Grafals-Ruiz, and P.E. Vivas-Mejia, *RNA interference for glioblastoma therapy: Innovation ladder from the bench to clinical trials.* Life Sci, 2017. **188**: p. 26-36.
156. Wick, W., et al., *Lomustine and Bevacizumab in Progressive Glioblastoma.* N Engl J Med, 2017. **377**(20): p. 1954-1963.
157. Miranda, A., et al., *Breaching barriers in glioblastoma. Part I: Molecular pathways and novel treatment approaches.* Int J Pharm, 2017. **531**(1): p. 372-388.
158. Allerstorfer, S., et al., *FGF5 as an oncogenic factor in human glioblastoma multiforme: autocrine and paracrine activities.* Oncogene, 2008. **27**(30): p. 4180-90.
159. Wang, H., et al., *The challenges and the promise of molecular targeted therapy in malignant gliomas.* Neoplasia, 2015. **17**(3): p. 239-55.
160. Granberg, K.J., et al., *Strong FGFR3 staining is a marker for FGFR3 fusions in diffuse gliomas.* Neuro Oncol, 2017. **19**(9): p. 1206-1216.
161. Loilome, W., et al., *Glioblastoma cell growth is suppressed by disruption of Fibroblast Growth Factor pathway signaling.* J Neurooncol, 2009. **94**(3): p. 359-66.
162. Wang, F., et al., *Tumor suppressors microRNA-302d and microRNA-16 inhibit human glioblastoma multiforme by targeting NF-kappaB and FGF2.* Mol Biosyst, 2017. **13**(7): p. 1345-1354.
163. Wang, F., et al., *Nuclear translocation of fibroblast growth factor-2 (FGF2) is regulated by Karyopherin-beta2 and Ran GTPase in human glioblastoma cells.* Oncotarget, 2015. **6**(25): p. 21468-78.
164. Yamaguchi, F., et al., *Differential expression of two fibroblast growth factor-receptor genes is associated with malignant progression in human astrocytomas.* Proc Natl Acad Sci U S A, 1994. **91**(2): p. 484-8.
165. Singh, D., et al., *Transforming fusions of FGFR and TACC genes in human glioblastoma.* Science, 2012. **337**(6099): p. 1231-5.
166. Lasorella, A., M. Sanson, and A. Iavarone, *FGFR-TACC gene fusions in human glioma.* Neuro Oncol, 2017. **19**(4): p. 475-483.

167. Brennan, C., *FGFR-TACC approaches the first turn in the race for targetable GBM mutations.* Neuro Oncol, 2017. **19**(4): p. 461-462.
168. Yamada, S.M., et al., *Fibroblast growth factor receptor (FGFR) 4 correlated with the malignancy of human astrocytomas.* Neurol Res, 2002. **24**(3): p. 244-8.
169. Gauglhofer, C., et al., *Up-regulation of the fibroblast growth factor 8 subfamily in human hepatocellular carcinoma for cell survival and neoangiogenesis.* Hepatology, 2011. **53**(3): p. 854-64.
170. Masica, D.L. and R. Karchin, *Correlation of somatic mutation and expression identifies genes important in human glioblastoma progression and survival.* Cancer Res, 2011. **71**(13): p. 4550-61.
171. Poh, W., et al., *Klotho-beta overexpression as a novel target for suppressing proliferation and fibroblast growth factor receptor-4 signaling in hepatocellular carcinoma.* Mol Cancer, 2012. **11**: p. 14.
172. Katoh, M., *FGFR inhibitors: Effects on cancer cells, tumor microenvironment and whole-body homeostasis (Review).* Int J Mol Med, 2016. **38**(1): p. 3-15.
173. Khalique, S. and S. Banerjee, *Nintedanib in ovarian cancer.* Expert Opin Investig Drugs, 2017. **26**(9): p. 1073-1081.
174. Riesco-Martinez, M.C., A. Sanchez-Torre, and R. Garcia-Carbonero, *Safety and efficacy of nintedanib for the treatment of metastatic colorectal cancer.* Expert Opin Investig Drugs, 2017. **26**(11): p. 1295-1305.
175. Roth, G.J., et al., *Nintedanib: from discovery to the clinic.* J Med Chem, 2015. **58**(3): p. 1053-63.
176. Wynes, M.W., et al., *FGFR1 mRNA and protein expression, not gene copy number, predict FGFR TKI sensitivity across all lung cancer histologies.* Clin Cancer Res, 2014. **20**(12): p. 3299-309.
177. El Demellawy, D., et al., *Update on molecular findings in rhabdomyosarcoma.* Pathology, 2017. **49**(3): p. 238-246.
178. Mitchell, R., et al., *Targeting BCR-ABL-Independent TKI Resistance in Chronic Myeloid Leukemia by mTOR and Autophagy Inhibition.* J Natl Cancer Inst, 2017.
179. Bucelli, C., et al., *Ponatinib as a Valid Alternative Strategy in Patients with Blast Crisis-Chronic Myeloid Leukemia Not Eligible for Allogeneic Stem Cells Transplantation and/or Conventional Chemotherapy: Report of a Case.* Case Rep Hematol, 2017. **2017**: p. 6167345.
180. Gentile, C., et al., *Kinase Inhibitors in Multitargeted Cancer Therapy.* Curr Med Chem, 2017. **24**(16): p. 1671-1686.
181. Zhang, J., et al., *Effects of 31 FDA approved small-molecule kinase inhibitors on isolated rat liver mitochondria.* Arch Toxicol, 2017. **91**(8): p. 2921-2938.
182. Duarte, A.C., M.J. Santos, and A. Cordeiro, *Anti-fibrotic nintedanib-a new opportunity for systemic sclerosis patients?* Clin Rheumatol, 2017.
183. Mao, X.G., et al., *LIN28A facilitates the transformation of human neural stem cells and promotes glioblastoma tumorigenesis through a pro-invasive genetic program.* Oncotarget, 2013. **4**(7): p. 1050-64.
184. Figueroa, J., et al., *Exosomes from Glioma-Associated Mesenchymal Stem Cells Increase the Tumorigenicity of Glioma Stem-like Cells via Transfer of miR-1587.* Cancer Res, 2017. **77**(21): p. 5808-5819.
185. Rashdan, S. and N. Hanna, *Nintedanib for the treatment of non-small-cell lung cancer.* Expert Opin Pharmacother, 2014. **15**(5): p. 729-39.

186. Huang, H.P., et al., *The prognostic significance of fibroblast growth factor receptor 4 in non-small-cell lung cancer.* Onco Targets Ther, 2015. **8**: p. 1157-64.
187. Repana, D. and P. Ross, *Targeting FGF19/FGFR4 Pathway: A Novel Therapeutic Strategy for Hepatocellular Carcinoma.* Diseases, 2015. **3**(4): p. 294-305.
188. Li, S.Q., et al., *Targeting wild-type and mutationally activated FGFR4 in rhabdomyosarcoma with the inhibitor ponatinib (AP24534).* PLoS One, 2013. **8**(10): p. e76551.
189. Whittle, S.B., et al., *A Polymorphism in the FGFR4 Gene Is Associated With Risk of Neuroblastoma and Altered Receptor Degradation.* J Pediatr Hematol Oncol, 2016. **38**(2): p. 131-8.
190. Mawrin, C., et al., *Analysis of a single nucleotide polymorphism in codon 388 of the FGFR4 gene in malignant gliomas.* Cancer Lett, 2006. **239**(2): p. 239-45.
191. Thussbas, C., et al., *FGFR4 Arg388 allele is associated with resistance to adjuvant therapy in primary breast cancer.* J Clin Oncol, 2006. **24**(23): p. 3747-55.
192. Luo, Y., et al., *Metabolic regulator betaKlotho interacts with fibroblast growth factor receptor 4 (FGFR4) to induce apoptosis and inhibit tumor cell proliferation.* J Biol Chem, 2010. **285**(39): p. 30069-78.
193. Tateno, T., et al., *The FGFR4-G388R polymorphism promotes mitochondrial STAT3 serine phosphorylation to facilitate pituitary growth hormone cell tumorigenesis.* PLoS Genet, 2011. **7**(12): p. e1002400.
194. Haugsten, E.M., et al., *Different intracellular trafficking of FGF1 endocytosed by the four homologous FGF receptors.* J Cell Sci, 2005. **118**(Pt 17): p. 3869-81.
195. Sailer, M.H., et al., *Non-invasive neural stem cells become invasive in vitro by combined FGF2 and BMP4 signaling.* J Cell Sci, 2013. **126**(Pt 16): p. 3533-40.
196. Chang, K.W., et al., *Fibroblast growth factor-2 up-regulates the expression of nestin through the Ras-Raf-ERK-Sp1 signaling axis in C6 glioma cells.* Biochem Biophys Res Commun, 2013. **434**(4): p. 854-60.
197. Gauglhofer, C., et al., *Fibroblast growth factor receptor 4: a putative key driver for the aggressive phenotype of hepatocellular carcinoma.* Carcinogenesis, 2014. **35**(10): p. 2331-8.
198. Wang, J., et al., *Altered fibroblast growth factor receptor 4 stability promotes prostate cancer progression.* Neoplasia, 2008. **10**(8): p. 847-56.
199. Cho, S.H., et al., *FGFR4 Arg388 Is Correlated with Poor Survival in Resected Colon Cancer Promoting Epithelial to Mesenchymal Transition.* Cancer Res Treat, 2017. **49**(3): p. 766-777.
200. Ulaganathan, V.K. and A. Ullrich, *Membrane-proximal binding of STAT3 revealed by cancer-associated receptor variants.* Mol Cell Oncol, 2016. **3**(3): p. e1145176.
201. Stadler, C.R., et al., *FGFR4 GLY388 isotype suppresses motility of MDA-MB-231 breast cancer cells by EDG-2 gene repression.* Cell Signal, 2006. **18**(6): p. 783-94.
202. Shi, S., et al., *High Expression of FGFR4 Enhances Tumor Growth and Metastasis in Nasopharyngeal Carcinoma.* J Cancer, 2015. **6**(12): p. 1245-54.

203. Sun, Y., et al., *Cancer-associated fibroblasts secrete FGF-1 to promote ovarian proliferation, migration, and invasion through the activation of FGF-1/FGFR4 signaling.* Tumour Biol, 2017. **39**(7): p. 1010428317712592.
204. Schosserer, M., J. Grillari, and M. Breitenbach, *The Dual Role of Cellular Senescence in Developing Tumors and Their Response to Cancer Therapy.* Front Oncol, 2017. **7**: p. 278.
205. Moulana, F.I., et al., *BRAF-Oncogene-Induced Senescence and the Role of Thyroid-Stimulating Hormone Signaling in the Progression of Papillary Thyroid Carcinoma.* Horm Cancer, 2017.
206. Smith, D.R., et al., *Clinical and molecular characteristics of gliosarcoma and modern prognostic significance relative to conventional glioblastoma.* J Neurooncol, 2017.
207. Zhao, H., et al., *FGF19 promotes epithelial-mesenchymal transition in hepatocellular carcinoma cells by modulating the GSK3beta/beta- catenin signaling cascade via FGFR4 activation.* Oncotarget, 2016. **7**(12): p. 13575-86.
208. Liu, R., et al., *FGFR4 promotes stroma-induced epithelial-to-mesenchymal transition in colorectal cancer.* Cancer Res, 2013. **73**(19): p. 5926-35.
209. Kim, S.M., et al., *Activation of the Met kinase confers acquired drug resistance in FGFR-targeted lung cancer therapy.* Oncogenesis, 2016. **5**(7): p. e241.
210. Kim, B., et al., *Synthetic lethal screening reveals FGFR as one of the combinatorial targets to overcome resistance to Met-targeted therapy.* Oncogene, 2015. **34**(9): p. 1083-93.
211. Adamski, V., et al., *Dormant glioblastoma cells acquire stem cell characteristics and are differentially affected by Temozolomide and AT101 treatment.* Oncotarget, 2017. **8**(64): p. 108064-108078.
212. Wang, T., et al., *JAK/STAT3-Regulated Fatty Acid beta-Oxidation Is Critical for Breast Cancer Stem Cell Self-Renewal and Chemoresistance.* Cell Metab, 2017.
213. Tiong, K.H., et al., *Fibroblast growth factor receptor 4 (FGFR4) and fibroblast growth factor 19 (FGF19) autocrine enhance breast cancer cells survival.* Oncotarget, 2016. **7**(36): p. 57633-57650.
214. Teng, Y., et al., *FGF19 Protects Hepatocellular Carcinoma Cells against Endoplasmic Reticulum Stress via Activation of FGFR4-GSK3beta-Nrf2 Signaling.* Cancer Res, 2017. **77**(22): p. 6215-6225.
215. Ahmed, M.A., et al., *Fibroblast growth factor receptor 4 induced resistance to radiation therapy in colorectal cancer.* Oncotarget, 2016. **7**(43): p. 69976-69990.
216. Gao, L., et al., *FGF19/FGFR4 signaling contributes to the resistance of hepatocellular carcinoma to sorafenib.* J Exp Clin Cancer Res, 2017. **36**(1): p. 8.

10. Appendix

10.1. Appendix 1. WHO classification (2007) of CNS tumors, based on histopathology

WHO classification of tumours of the central nervous system

Diffuse astrocytic and oligodendroglial tumours	
Diffuse astrocytoma, IDH-mutant	9400/3
Gemistocytic astrocytoma, IDH-mutant	9411/3
Diffuse astrocytoma, IDH-wildtype	*9400/3*
Diffuse astrocytoma, NOS	9400/3
Anaplastic astrocytoma, IDH-mutant	9401/3
Anaplastic astrocytoma, IDH-wildtype	*9401/3*
Anaplastic astrocytoma, NOS	9401/3
Glioblastoma, IDH-wildtype	9440/3
Giant cell glioblastoma	9441/3
Gliosarcoma	9442/3
Epithelioid glioblastoma	*9440/3*
Glioblastoma, IDH-mutant	9445/3*
Glioblastoma, NOS	9440/3
Diffuse midline glioma, H3 K27M–mutant	9385/3*
Oligodendroglioma, IDH-mutant and 1p/19q-codeleted	9450/3
Oligodendroglioma, NOS	9450/3
Anaplastic oligodendroglioma, IDH-mutant and 1p/19q-codeleted	9451/3
Anaplastic oligodendroglioma, NOS	*9451/3*
Oligoastrocytoma, NOS	*9382/3*
Anaplastic oligoastrocytoma, NOS	*9382/3*
Other astrocytic tumours	
Pilocytic astrocytoma	9421/1
Pilomyxoid astrocytoma	9425/3
Subependymal giant cell astrocytoma	9384/1
Pleomorphic xanthoastrocytoma	9424/3
Anaplastic pleomorphic xanthoastrocytoma	9424/3
Ependymal tumours	
Subependymoma	9383/1
Myxopapillary ependymoma	9394/1
Ependymoma	9391/3
Papillary ependymoma	9393/3
Clear cell ependymoma	9391/3
Tanycytic ependymoma	9391/3
Ependymoma, *RELA* fusion–positive	9396/3*
Anaplastic ependymoma	9392/3
Other gliomas	
Chordoid glioma of the third ventricle	9444/1
Angiocentric glioma	9431/1
Astroblastoma	9430/3
Choroid plexus tumours	
Choroid plexus papilloma	9390/0
Atypical choroid plexus papilloma	9390/1
Choroid plexus carcinoma	9390/3
Neuronal and mixed neuronal-glial tumours	
Dysembryoplastic neuroepithelial tumour	9413/0
Gangliocytoma	9492/0
Ganglioglioma	9505/1
Anaplastic ganglioglioma	9505/3
Dysplastic cerebellar gangliocytoma (Lhermitte–Duclos disease)	9493/0
Desmoplastic infantile astrocytoma and ganglioglioma	9412/1
Papillary glioneuronal tumour	9509/1
Rosette-forming glioneuronal tumour	9509/1
Diffuse leptomeningeal glioneuronal tumour	
Central neurocytoma	9506/1
Extraventricular neurocytoma	9506/1
Cerebellar liponeurocytoma	9506/1
Paraganglioma	8693/1
Tumours of the pineal region	
Pineocytoma	9361/1
Pineal parenchymal tumour of intermediate differentiation	9362/3
Pineoblastoma	9362/3
Papillary tumour of the pineal region	9395/3
Embryonal tumours	
Medulloblastomas, genetically defined	
Medulloblastoma, WNT-activated	9475/3*
Medulloblastoma, SHH-activated and *TP53*-mutant	9476/3*
Medulloblastoma, SHH-activated and *TP53*-wildtype	9471/3
Medulloblastoma, non-WNT/non-SHH	9477/3*
Medulloblastoma, group 3	
Medulloblastoma, group 4	
Medulloblastomas, histologically defined	
Medulloblastoma, classic	9470/3
Medulloblastoma, desmoplastic/nodular	9471/3
Medulloblastoma with extensive nodularity	9471/3
Medulloblastoma, large cell / anaplastic	9474/3
Medulloblastoma, NOS	9470/3
Embryonal tumour with multilayered rosettes, C19MC-altered	9478/3*
Embryonal tumour with multilayered rosettes, NOS	*9478/3*
Medulloepithelioma	9501/3
CNS neuroblastoma	9500/3
CNS ganglioneuroblastoma	9490/3
CNS embryonal tumour, NOS	9473/3
Atypical teratoid/rhabdoid tumour	9508/3
CNS embryonal tumour with rhabdoid features	*9508/3*
Tumours of the cranial and paraspinal nerves	
Schwannoma	9560/0
Cellular schwannoma	9560/0
Plexiform schwannoma	9560/0

Melanotic schwannoma	9560/1
Neurofibroma	9540/0
Atypical neurofibroma	9540/0
Plexiform neurofibroma	9550/0
Perineurioma	9571/0
Hybrid nerve sheath tumours	
Malignant peripheral nerve sheath tumour	9540/3
Epithelioid MPNST	9540/3
MPNST with perineurial differentiation	9540/3
Meningiomas	
Meningioma	9530/0
Meningothelial meningioma	9531/0
Fibrous meningioma	9532/0
Transitional meningioma	9537/0
Psammomatous meningioma	9533/0
Angiomatous meningioma	9534/0
Microcystic meningioma	9530/0
Secretory meningioma	9530/0
Lymphoplasmacyte-rich meningioma	9530/0
Metaplastic meningioma	9530/0
Chordoid meningioma	9538/1
Clear cell meningioma	9538/1
Atypical meningioma	9539/1
Papillary meningioma	9538/3
Rhabdoid meningioma	9538/3
Anaplastic (malignant) meningioma	9530/3
Mesenchymal, non-meningothelial tumours	
Solitary fibrous tumour / haemangiopericytoma**	
Grade 1	8815/0
Grade 2	8815/1
Grade 3	8815/3
Haemangioblastoma	9161/1
Haemangioma	9120/0
Epithelioid haemangioendothelioma	9133/3
Angiosarcoma	9120/3
Kaposi sarcoma	9140/3
Ewing sarcoma / PNET	9364/3
Lipoma	8850/0
Angiolipoma	8861/0
Hibernoma	8880/0
Liposarcoma	8850/3
Desmoid-type fibromatosis	8821/1
Myofibroblastoma	8825/0
Inflammatory myofibroblastic tumour	8825/1
Benign fibrous histiocytoma	8830/0
Fibrosarcoma	8810/3
Undifferentiated pleomorphic sarcoma / malignant fibrous histiocytoma	8802/3
Leiomyoma	8890/0
Leiomyosarcoma	8890/3
Rhabdomyoma	8900/0
Rhabdomyosarcoma	8900/3
Chondroma	9220/0
Chondrosarcoma	9220/3
Osteoma	9180/0
Osteochondroma	9210/0
Osteosarcoma	9180/3
Melanocytic tumours	
Meningeal melanocytosis	8728/0
Meningeal melanocytoma	8728/1
Meningeal melanoma	8720/3
Meningeal melanomatosis	8728/3
Lymphomas	
Diffuse large B-cell lymphoma of the CNS	9680/3
Immunodeficiency-associated CNS lymphomas	
AIDS-related diffuse large B-cell lymphoma	
EBV-positive diffuse large B-cell lymphoma, NOS	
Lymphomatoid granulomatosis	9766/1
Intravascular large B-cell lymphoma	9712/3
Low-grade B-cell lymphomas of the CNS	
T-cell and NK/T-cell lymphomas of the CNS	
Anaplastic large cell lymphoma, ALK-positive	9714/3
Anaplastic large cell lymphoma, ALK-negative	9702/3
MALT lymphoma of the dura	9699/3
Histiocytic tumours	
Langerhans cell histiocytosis	9751/3
Erdheim–Chester disease	9750/1
Rosai–Dorfman disease	
Juvenile xanthogranuloma	
Histiocytic sarcoma	9755/3
Germ cell tumours	
Germinoma	9064/3
Embryonal carcinoma	9070/3
Yolk sac tumour	9071/3
Choriocarcinoma	9100/3
Teratoma	9080/1
Mature teratoma	9080/0
Immature teratoma	9080/3
Teratoma with malignant transformation	9084/3
Mixed germ cell tumour	9085/3
Tumours of the sellar region	
Craniopharyngioma	9350/1
Adamantinomatous craniopharyngioma	9351/1
Papillary craniopharyngioma	9352/1
Granular cell tumour of the sellar region	9582/0
Pituicytoma	9432/1
Spindle cell oncocytoma	8290/0
Metastatic tumours	

The morphology codes are from the International Classification of Diseases for Oncology (ICD-O) {742A}. Behaviour is coded /0 for benign tumours; /1 for unspecified, borderline, or uncertain behaviour; /2 for carcinoma in situ and grade III intraepithelial neoplasia; and /3 for malignant tumours. The classification is modified from the previous WHO classification, taking into account changes in our understanding of these lesions.
*These new codes were approved by the IARC/WHO Committee for ICD-O.
Italics: Provisional tumour entities. **Grading according to the 2013 *WHO Classification of Tumours of Soft Tissue and Bone*.

10.2. Appendix 2: Grading of CNS tumors conform WHO, updated in 2016

WHO grades of select CNS tumours	
Diffuse astrocytic and oligodendroglial tumours	
Diffuse astrocytoma, IDH-mutant	II
Anaplastic astrocytoma, IDH-mutant	III
Glioblastoma, IDH-wildtype	IV
Glioblastoma, IDH-mutant	IV
Diffuse midline glioma, H3 K27M–mutant	IV
Oligodendroglioma, IDH-mutant and 1p/19q-codeleted	II
Anaplastic oligodendroglioma, IDH-mutant and 1p/19q-codeleted	III
Other astrocytic tumours	
Pilocytic astrocytoma	I
Subependymal giant cell astrocytoma	I
Pleomorphic xanthoastrocytoma	II
Anaplastic pleomorphic xanthoastrocytoma	III
Ependymal tumours	
Subependymoma	I
Myxopapillary ependymoma	I
Ependymoma	II
Ependymoma, *RELA* fusion–positive	II or III
Anaplastic ependymoma	III
Other gliomas	
Angiocentric glioma	I
Chordoid glioma of third ventricle	II
Choroid plexus tumours	
Choroid plexus papilloma	I
Atypical choroid plexus papilloma	II
Choroid plexus carcinoma	III
Neuronal and mixed neuronal-glial tumours	
Dysembryoplastic neuroepithelial tumour	I
Gangliocytoma	I
Ganglioglioma	I
Anaplastic ganglioglioma	III
Dysplastic gangliocytoma of cerebellum (Lhermitte–Duclos)	I
Desmoplastic infantile astrocytoma and ganglioglioma	I
Papillary glioneuronal tumour	I
Rosette-forming glioneuronal tumour	I
Central neurocytoma	II
Extraventricular neurocytoma	II
Cerebellar liponeurocytoma	II
Tumours of the pineal region	
Pineocytoma	I
Pineal parenchymal tumour of intermediate differentiation	II or III
Pineoblastoma	IV
Papillary tumour of the pineal region	II or III
Embryonal tumours	
Medulloblastoma (all subtypes)	IV
Embryonal tumour with multilayered rosettes, C19MC-altered	IV
Medulloepithelioma	IV
CNS embryonal tumour, NOS	IV
Atypical teratoid/rhabdoid tumour	IV
CNS embryonal tumour with rhabdoid features	IV
Tumours of the cranial and paraspinal nerves	
Schwannoma	I
Neurofibroma	I
Perineurioma	I
Malignant peripheral nerve sheath tumour (MPNST)	II, III or IV
Meningiomas	
Meningioma	I
Atypical meningioma	II
Anaplastic (malignant) meningioma	III
Mesenchymal, non-meningothelial tumours	
Solitary fibrous tumour / haemangiopericytoma	I, II or III
Haemangioblastoma	I
Tumours of the sellar region	
Craniopharyngioma	I
Granular cell tumour	I
Pituicytoma	I
Spindle cell oncocytoma	I

10.3. Abbreviations

ABC-family	ATP-binding cassette transporter family
ADT	Androgen-deprivation therapy
ALK	Anaplastic lymphoma kinase
AML	Acute myeloid leukaemia
Arg	Arginine
ATP	Adenosine triphosphate
ATRX	Alpha thalassemia retardation syndrome X-linked
BBB	Blood-brain barrier
CAF	Cancer associated fibroblasts
CC	Cancer cells
CD	Communicable diseases
CGH	Comparative genome hybridization
CLSM	Confocal laser scanning microscopy
CML	Chronic myeloid leukaemia
CMV	Cytomegalovirus
CNS	Central nervous system
CRISPR	Clustered Regularly Interspaced Short Palindromic Repeats
CSC	Cancer stem cells
CT	Computed tomography
CTLA-4	Cytotoxic T-lymphocyte-associated protein 4
DAPI	6-diamidino-2-phenylindole
DMSO	Dimethyl sulfoxide
DNA	Deoxyribonucleic acid
ECM	Extracellular matrix
EGF	Epidermal growth factor
EGFR	EGF receptor tyrosine kinase
EMT	Epithelial to mesenchymal transition

FACS	Fluorescence-activated cell sorting
FCS	Fetal calf serum
FD	Fast-digest
FDA	US food and drug administration
FELASA	Federation for laboratory animal science associations
FGF	Fibroblast growth factor
FGFR	FGF receptor tyrosine kinase
GBM	Glioblastoma multiforme
GFP	Green fluorescent protein
Gly	Glycine
GLUT1	Glucose transporter
GMT	Glial-to-mesenchymal transition
GoF	Gain-of-function
GS	Gliosarcoma
GSCs	Glioma stem cells
HBV	Hepatitis B virus
HCC	Hepatocellular carcinoma
HSPG	Heparine-sulfate proteoglycans
IBD	Inflammatory bowel diseases
ICs	Immune inflammatory cells
IDH1/2	Isocitrate dehydrogenase 1/2
kDa	Kilo Dalton
MAPK	Mitogen activated protein kinase
MCS	Multiple cloning site

MET	Mesenchymal to epithelial-like transition
MGMT	O^6-methylguanine-DNA-methyltransferase
MHC	Major histocompatibility complex
MDR1	Multidrug-resistance protein 1
MRI	Magnetic resonance imaging
MRP	MDR –related proteins
NAA	N-acetyl-aspartate
NCs	Neural crest cells
NCD	Noncommunicable diseases
O/N	over night
Ori	Origin of replication
PCR	Polymerase chain reaction
PFA	Paraformaldehyde
PC	Pericytes
PD-1	Programmed cell death receptor-1
PDL-1	PD-1 ligand
PDGF	Platelet derived growth factor
PDFGR	PDGF receptor tyrosine kinase
PET	Positron-emission tomography
P-gp	P-glycoprotein
PI3K	Phosphotidylinositol-3-kinase
PTEN	Phosphatase and tensin homologue deleted on chromosome 10
RB	Retinoblastoma-associated protein
RFLP	Restriction fragment length polymorphism
ROS	Reactive oxygen species
RT-qPCR	Quantitative real-time PCR
RTK	Receptor tyrosine kinase
SCID	Severe combined immunideficiency

SDS-PAGE	Sodium dodecyl sulfate polyacrylamide gel electrophoresis
SNP	Single nucleotide polymorphism
src	Sarcoma
STAT	Signal transducer and activator of transcription
TCGA	The cancer genome atlas
TCR	T-cell receptor
TKI	Tyrosine kinase inhibitor
TME	Tumor microenvironment
TMZ	Temozolomide
TNF-α	Tumor necrosis factor-α
TSP-1	Thrombospondin-1
UV	Ultraviolet
VEGF-A	Vascular endothelial growth factor-A
VEGFR 1-3	VEGF receptor tyrosine kinases 1-3
WGA	Wheat germ agglutinin
WHO	World Health Organization